Retrospective study of suspended sediment patterns on Lake Winnipeg using NOAA AVHRR satellite imagery

Final Report
29 March 2001

Greg McCullough,
Klaus Hochheim
and Paul Cooley

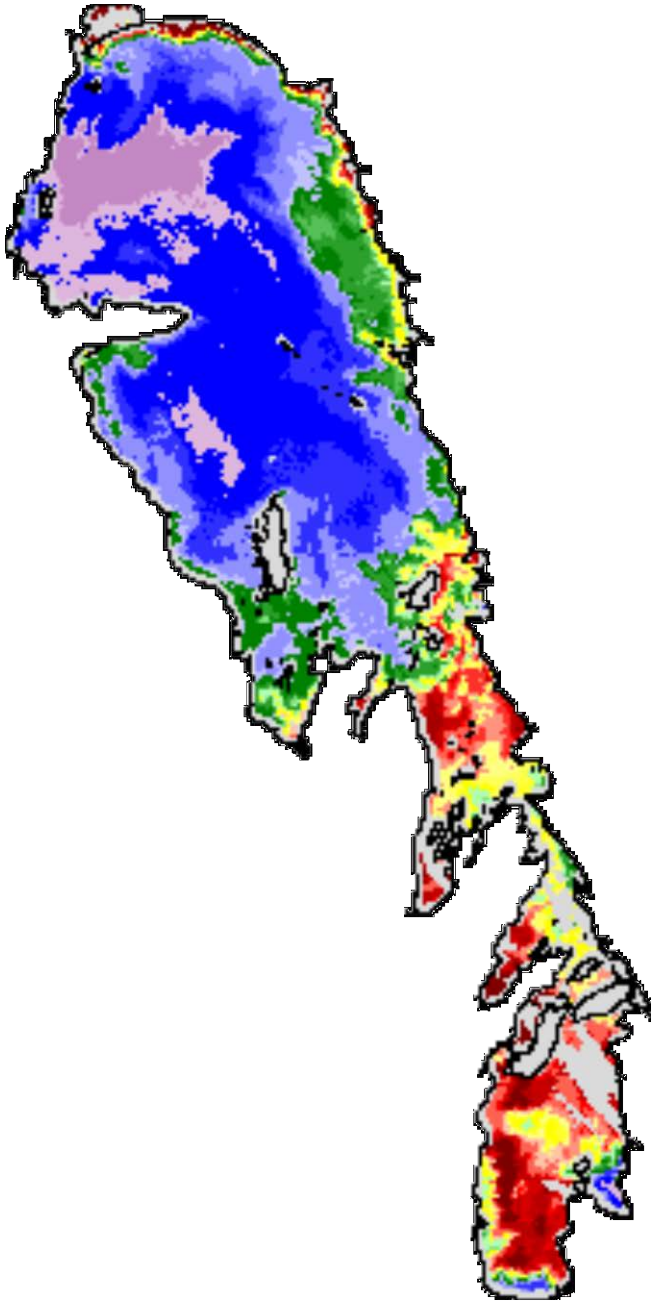

Prepared for the
Canada Department of
Fisheries and Oceans,
Winnipeg, Canada

Table of Contents

List of Tables

List of Figures

1 INTRODUCTION

Over the last two decade there has been growing public and scientific concern about the health of Lake Winnipeg. In 1980, Brunskill et al. warned of a trend towards increasing nutrient supply from it watersheds, particularly in the Prairies where increasingly intensive agriculture was leading to higher nutrient loads in influent rivers. Since 1975, the lake has been controlled as a storage reservoir for hydroelectric production in the downstream Nelson River, increasing winter discharge at the expense of summer outflow. This changed regime would effectively increase nutrient storage by reducing outflow at the summer period of peak plankton productivity, and therefore peak suspended nutrient concentration. Over this same period, and particularly in the last decade, Lake Winnipeg fishermen have reported increasing frequency and magnitude of algal blooms.

Suspended sediments are a critical component of freshwater aquatic systems, simultaneously supplying nutrients and reducing light necessary for biological production. In the last few decades, we have also come to understand their significance as agents of contaminant transport into and removal from aquatic systems. However, their discontinuous distribution and dynamic movement through lacustrine environments has made sediments difficult to monitor adequately by traditional limnological point sampling techniques. Although airborne photography has been used in the past to study patterns of turbidity, the most promising quantitative techniques for capturing this spatial dimension have employed calibrated multispectral scanners, especially those carried by satellites now continuously in orbit above the earth.

This study begins an attempt to document suspended sediment and productivity patterns on Lake Winnipeg using satellite remote sensing. We have used a set of National Oceanic and Atmospheric Administration's (NOAA) Advanced Very High Resolution Radiometer (AVHRR) images of Lake Winnipeg to create maps of suspended solids concentration (TSS) on Lake Winnipeg through the period 1985 to 2000. A primary data set of 15 TSS maps documents mid-summer TSS in each year, and a second set shows monthly TSS, June through September, in four selected years.

1.1 Objectives and scope

This work has been done under contract to the Canada Department of Fisheries and Oceans, Winnipeg office. The requirements, tasks and products of the contract are copied in Appendix 1.

There are two requirements:

1. To identify possible trends in surface suspended solids quantity and patterns in L. Winnipeg over the period 1985-2000.

2. To study intra- and inter-annual seasonal variability in surface suspended solids quantity and patterns in Lake Winnipeg for flood and drought years and between warm and cool summers.

Also, we were asked to produce a series of normalized difference vegetation index maps (NDVI) investigate the utility of AVHRR-derived NDVI for mapping chlorophyll.

2 TECHNICAL AND SCIENTIFIC BACKGROUND

2.1.1 The AVHRR Historical Record

The United States National Oceanic and Atmospheric Administration (NOAA) in 1972 launched the first in a series of Polar-orbiting Operational Environmental Satellites which carried, among several earth atmosphere and surface monitoring instruments, a radiometer [the Very High Resolution Radiometer (VHRR)] capable of recording visible and near-infrared, daytime upwelling radiance data for the whole earth on a daily basis. With the launch of NOAA-7, in June, 1979, NOAA inaugurated the Advanced Very High Resolution Radiometer (AVHRR) with slightly altered spectral and spatial resolution from the VHRR. From NOAA-7 to the currently operating NOAA-14, successive AVHRRs carried into orbit have had similar operating characteristics, spatial resolution and spectral sensitivity and have been calibrated before launch to produce comparable radiometric data.

NOAA-7 through NOAA-14 satellites have been launched in sun-synchronous, polar orbits with an orbital period of about 102 min (Kidwell, 1997).. Although their orbital path relative to the earth's surface repeats only every nine days, the instrument scan width, imaging a 2400 km wide path, is such it records images covering every part of the earth twice daily. Odd-numbered satellites have afternoon daylight orbital passes with ascending equatorial crossings at about 14:30 local time. Even numbered satellites record morning and evening scenes, with equatorial crossings at about 07:30 local time (descending) and 19:30 local time (ascending). NOAA-14 is an exception to this general rule as it is an "afternoon" satellite; it was put into this orbit to replace NOAA-13 which failed after only about two weeks of operation (Kidwell, 1997).

Data from the NOAA-9 to -14 satellites has been archived with near-daily frequency throughout their operational life spans, and is available from the NOAA Satellite Services Branch (online through the Satellite Active Archive) and the United States Geological Survey Earth Resources Observation System Data Centre.

The AVHRR instrument that has been orbiting on the NOAA-7 to -14 satellites is a cross-track scanner with a spatial resolution of about 1.1 km at nadir and about 3.8 km at the maximum scan angle of 55^{o}. AVHRRs record electromagnetic energy with 10-bit precision in 5 bands of the electromagnetic spectrum, including mid- (Channel 3, 355-393 nm) and far-infrared (Channels 4 and 5, 1030-1130 nm and 1150-1240 nm) thermal

radiation (Kidwell, 1997). Of interest in this study of suspended sediments are the short wave radiation channels, Channel 1, which senses orange-red visible light (580-680 nm) and Channel 2, which senses near-infrared radiation (725-1100 nm). The former has achieved widespread use for mapping of surface-water suspended sediments, and the two in combination are used to produce normalized-difference vegetation index (NDVI) maps. Although the latter are traditionally used for mapping terrestrial vegetation, it has been used for mapping chlorophyll in Case-1 waters (i.e. sediment-free open ocean waster) and it is shown in this study that they may be correlated with in-lake measurements of chlorophyll in Lake Winnipeg.

2.1.2 ***Absorption and scattering by mineral and organic particles***

The following is condensed from McCullough (1998) in which the relationship between AVHRR-measured albedo and suspended sediment concentrations were investigated in a Lake Erie case study.

Although particle scattering is the predominant source of upwelling light in all but very clear waters, the spectral distribution of upwelling light is a complex product of combined absorption and scattering properties of the water column and its suspended load. Light scattered upwards from any given layer in the water column is due to downwelling light not previously attenuated multiplied by the backscattering coefficient. That backscattered light is again attenuated by the same processes in its path through the water column back up to the surface. Attenuation of both downwelling and upwelling light streams is itself the result of both absorption and scattering, in which scattering contributes by lengthening the path available for aborption. Morel and Prieur (1977) followed this logic to predict at-surface albedo as a function of the ratio backscatter:absorption, with an empirically-derived, linear coefficient dependent on the radiance distribution and the volume scattering function of the water column and its suspended load. They used this relationship successfully to predict spectral albedo functions for very clear marine waters, for which molecular backscattering was a significant component of total backscatter. Whitlock et al. (1981a) show a curvilinear relationship of albedo with backscatter:absorption. They attribute the uncertainty in the relationship mainly to unresolved effects of solar zenith angle and relative sun-sky illumination. Regardless, it is useful to bear in mind the spectral distribution of backscatter:absorption when considering the spectral distribution of albedo.

Although spectral albedo curves vary in their details, several general features are common to spectral albedo curves for natural suspensions. For illustration, we have reproduced Han's (1997) figures showing spectral distribution of albedo over suspensions both purely of mineral sediments (Figure 1a), and mixed with algae (Figure 1b). He measured spectral albedo under mid-day sun in a large, black-lined, open tank for two experiments: one in which he progressively added 25 $mg \cdot L^{-1}$ increments of sieved, red loam soil to clear well-water, and a second in which he made identical additions to algae-laden water.

Spectral albedo distribution over suspensions of sediments is highest between 550-700 nm, with a secondary peak at 800-810 nm. The secondary peak is barely significant at the lowest concentrations due to the relatively high attenuation of the infrared light. The gradual shift in the major peak to the right with increasing sediment load is a highly typical progression observed in most published studies. In Hans' experiment the peak shifts from about 570 nm at 25 $mg \cdot L^{-1}$ to 630 nm at 500 $mg \cdot L^{-1}$; Ritchie et al. (1976) found a shift from 550 nm at 30 $mg \cdot L^{-1}$ to 600 at 300 $mg \cdot L^{-1}$; Whitlock et al. (1981b) in laboratory studies using lake bottom sediments, show migration of peak reflectance from 550-600 nm at 5-100 $mg \cdot L^{-1}$ to over 700 nm at 600-800 $mg \cdot L^{-1}$.

Spectral distribution of absorption coefficients are sufficient to explain this shift. Molecular backscattering coefficients are small enough at visible and near-infrared wavelengths that they do not contribute to the shift except in almost optically pure water. Particle backscattering coefficients show such weak wavelength dependency as to have no significant effect compared to the active absorption coefficients. This is best understood with reference to Figure 2 which illustrates the relationship between absorption and backscatter of suspensions by combining data from Kirk (1980, Figure 1) and Morel (1974, Figure 4).

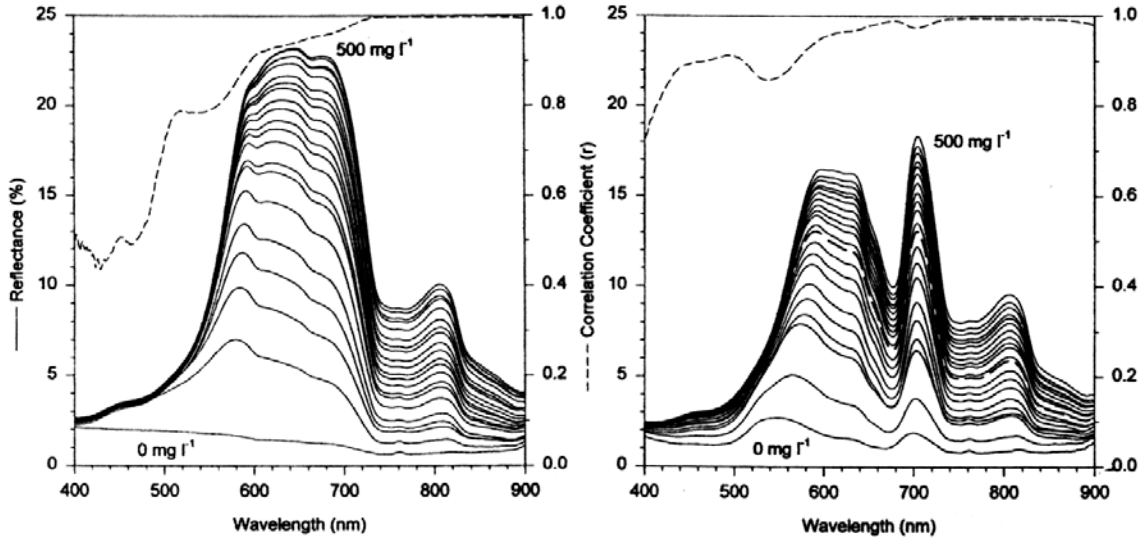

Figure 1. Spectral at-surface albedo of suspensions of red loam soil (35% sand, 43% silt, 22% clay) ranging from 0-500 mg L^{-1} in (a) clear water and (b) algae-laden (chlorophyll = 302 $ug \cdot L^{-1}$) water. The dashed line above the spectrograms indicated the coefficient of linear correlation between reflectance and sediment concentration. (After Han, 1997; Figure 3 and 4.)

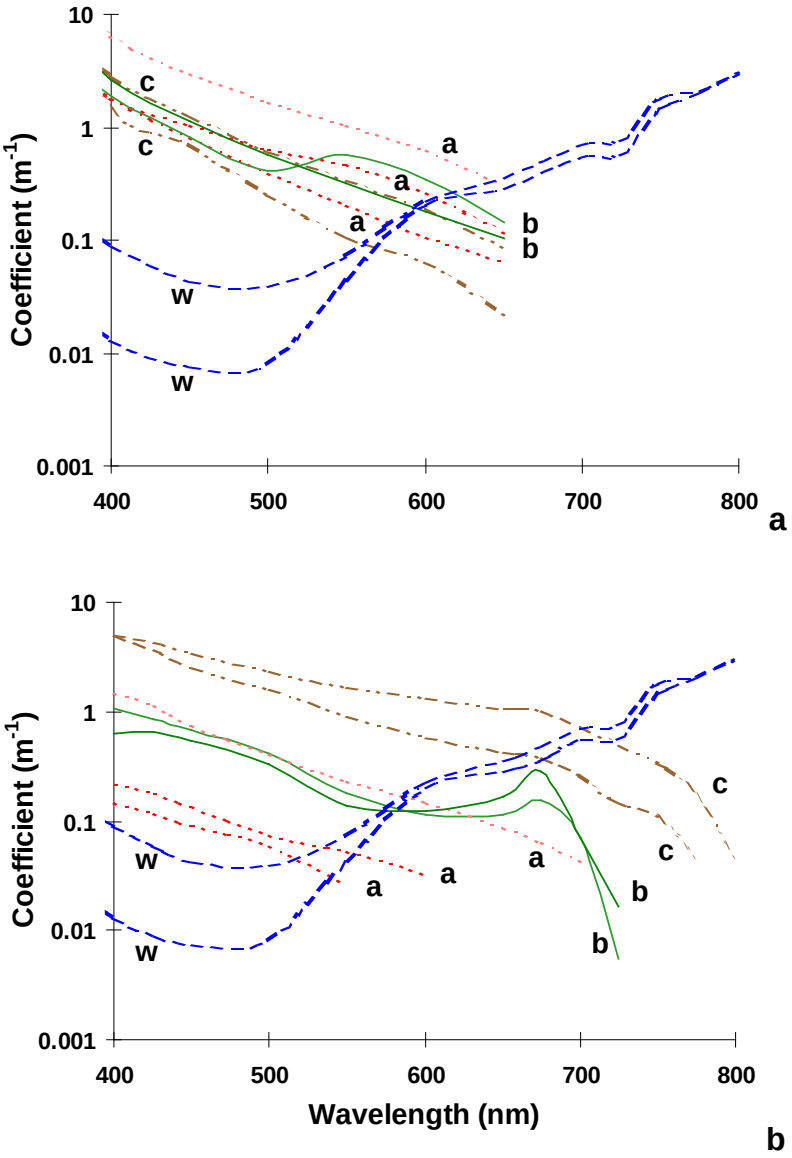

Figure 2. Spectral distribution, in the visible and near-infrared range, of absorption coefficients for a) dissolved and b) particulate matter from Australian lakes (after Kirk, 1980, Figure 1). Sample chlorophyll-a concentrations ranged from 1.5-16 ug·L^{-1}; turbidity ranged from 0.51-49 N.T.U. a = mod. to high colour, low chl-a (< 2 ug·L^{-1}), low to mod. turbidity; b = high chl-a (>9 ug·L^{-1}), mod. turbidity dominated by phytoplankton; c = high turbidity, mod. chl-a, dominated by silt. w = range of reported values for vertical attenuation coefficients for optically pure water (after Morel, 1974, Figure 4).

Absorption due to water increases steeply through the visible and near-infrared range from a minimum at about 500 nm. Absorption due to both dissolved substances and suspended materials, on the other hand, is inversely correlated with wavelength through the same range, and at 500 nm, even at moderate turbidities is higher than absorption due to water. The two oppositely-sloping spectra intersect in the visible to near-infrared

range. Increasing turbidity (Figure 2, lines "a" – low to moderate turbidity; lines "c" – high turbidity) shifts the intersection point both upwards (higher absorption) and to the right (higher wavelengths). The intersection of the spectrum of absorption by water with the spectrum of absorption by dissolved and suspended materials marks the wavelength of maximum potential depth penetration of incident light, and hence the wavelength of maximum numbers of light scatterings by suspended particles, producing the peak spectral albedo. Peak albedo, then, shifts to higher wavelengths with increasing concentration.

In comparison to mineral suspended material, some dissolved and suspended substances, including organic acids, and chlorophyll in plankton, are more effective absorbers than reflectors (Han, 1997; Kirk, 1980). As a result, the spectral distribution of albedo for suspended particulate matter may be dramatically altered by the presence of living algae (Figure 1b, and absorption spectra "b" in Figure 2b). Although the chorophyll concentration Han employed would be unusual and indicative of severely eutrophic conditions in nature, his illustration is nonetheless indicative of its spectral influence on albedo. At 600 nm, the peak albedo due to inorganic sediments, albedo was decreased about one-third in Han's data by strong chlorophyll absorbance. Depression of albedo by chlorophyll caused the correlation between reflectance and suspended mineral concentration to be weak throughout the visible range, even though chlorophyll absorption actually peaks in the 400-450 nm range (Per Halldal, 1974). Most dramatic is the reduction in albedo centred at 670-680 nm. This is matched (and caused) by the secondary peak in absorbance apparent in Kirk's (1980) two high-chlorophyll-a absorbance spectra (b in Figure 2b). A third narrow absorbance peak due to phycoerythrin and/or phycocyanin at about 620 nm (Per Halldal, 1974) is not apparent in these data. Kirk's results also show a sharp drop-off in chlorophyll absorbance beyond 700 nm consistent with Han's albedo data. Between 700-900 nm in Han's data, the depression of albedo by algae was only a few percent, and the correlation between albedo and suspended sediment concentration was consistently very high.

The chlorophyll concentration (302 $ug \cdot L^{-1}$) which Han used in his experiment is indicative of severely eutrophic conditions in nature. Because high suspended sediment concentrations tend to limit algal productivity by limiting light, such a high chlorophyll concentration in combination with suspended sediment concentrations greater than 50 $mg \cdot L^{-1}$ is uncommon in natural lakes. Certainly, this describes the prevailing suspended sediment concentration in Lake Winnipeg. Bukata et al. (1995) showed that water with high concentrations of inorganic sediment have volume reflectances in the visible wavelengths almost an order of magnitude higher than water with similar concentrations of chlorophyll. On the other hand, chlorophyll is not purely absorptive. At 650 nm wavelength, they showed that chlorophyll at concentrations typical of the Great Lakes, 0.05-20 ug L^{-1}, had a significant and positive effect on reflectance of suspended mineral concentrations less than 100 mg L^{-1}. At higher suspended sediment concentrations reflectance was slightly reduced by increasing chlorophyll concentration.

3 METHODS

3.1 Location

Lake Winnipeg lies on the edge between Central Plains and Precambrian Shield in central Manitoba. It is a (Figure 3) 24,000 km^2 lake, stretching 400 km from NNW to SSE from about 50^{o}N to almost 54^{o}N at its outlet into the Nelson River at Warrens Landing. It comprises a smaller South Basin, 40 km wide at its widest point, and a much larger North basin over 200 km long and 90 km wide at its widest point, separated by a Narrows region broken into small basins and bays separated by islands and broad peninsulas. It is fed from the Central Plains by two major rivers from the west -- the Saskatchewan River -- and south -- the Red-Assiniboine River system -- and the Dauphin-Fairford River which drains two other major Plains lakes, Lake Manitoba and Lake Winnipegosis. From the Precambrian Shield, it is fed by one major river, the Winnipeg River, and numerous smaller rivers. Altogether, it is tributary to about 780 000 km^2 of Plains drainage and 174 000 km^2 of Shield drainage.

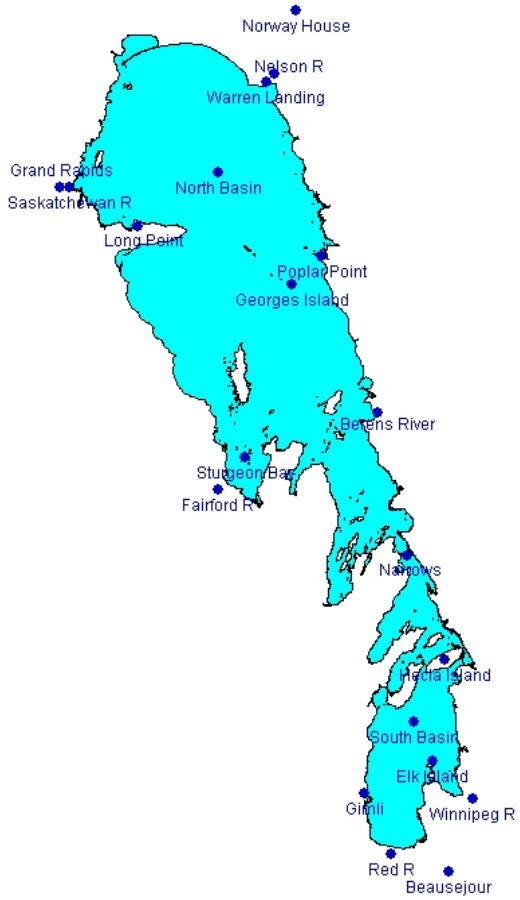

Figure 3. Lake Winnipeg place names used in this report.

3.2 Water quality, water quantity and climate data

3.2.1 Water quality

Total suspended solids (TSS) and chlorophyll concentrations referred to in this study were supplied by the Mike Stainton of the Canada Department of Fisheries and Oceans chemistry laboratory at the Freshwater Institute in Winnipeg. Analyses are as described by Stainton et al. (1977).

For both TSS and chlorophyll, near-surface dip samples of lake water collected in the field were returned as quickly as possible (usually a few days to a week) to Winnipeg, where they were filtered through ashed, preweighed glass fibre filters with a nominal pore size of 1.2 um (Whatman® GF/C filters). After filtration, filters were dried at 105^{o}C to a constant weight before reweighing. Results were reported to the nearest 1 mg$\cdot$L^{-1}.

In August 1999 and again in August 2000, optical turbidity and fluorometer data were collected using a continuous flow system along transects in Lake Winnipeg (Figure 37). Both turbidity and chlorophyll fluorescence were measured with Turner fluorometers fitted with 2 cm i.d. flow through cells. The cells were connected in series to a tube carrying lake water pumped continuously while enroute. Turbidity was determined by measuring light reflected at 90^{o} from the incident path through the cell. In the fluorescence mode, emission at 650-675 nm was measured using excitation at 430-450 nm. On both cruise, calibration samples were taken both in-line and off the ship's side for later analysis for both TSS and chlorophyll-a.

At intervals during the cruises, flow in the system was sampled and/or ship-side samples were taken for TSS and chlorophyll analysis. These TSS and chlorophyll data were used to calibrate the instruments as continuous-flow TSS and chlorophyll meters. For the 22-25 August 2000 cruise, TSS was estimated for the flow-through turbidity meter data set using with the following equation

$$TSS = 194.92\, S_{90}^{\ 1.7395}$$

where

TSS = total suspended solids measured by filtration (GFC, nominally 1.1. *u*m, mg$\cdot$L^{-1})

S_{90} = light scattering at 90^{o} to incident beam, as measured on a flow-through turbidity meter (volts)

The equation is based on regression of S_{90} with TSS from flow-through and ship-side samples. For correlation between the logarithms of TSS and S90, r2=0.90 (n=27, 5<TSS<34 mg/L, significance F=0.000). The four greatest outliers (Figure 4) were removed to calculate the coefficients for calibration equation, above. Dropping the outliers improved the apparent fit of the regression line with the remaining data at higher TSS.

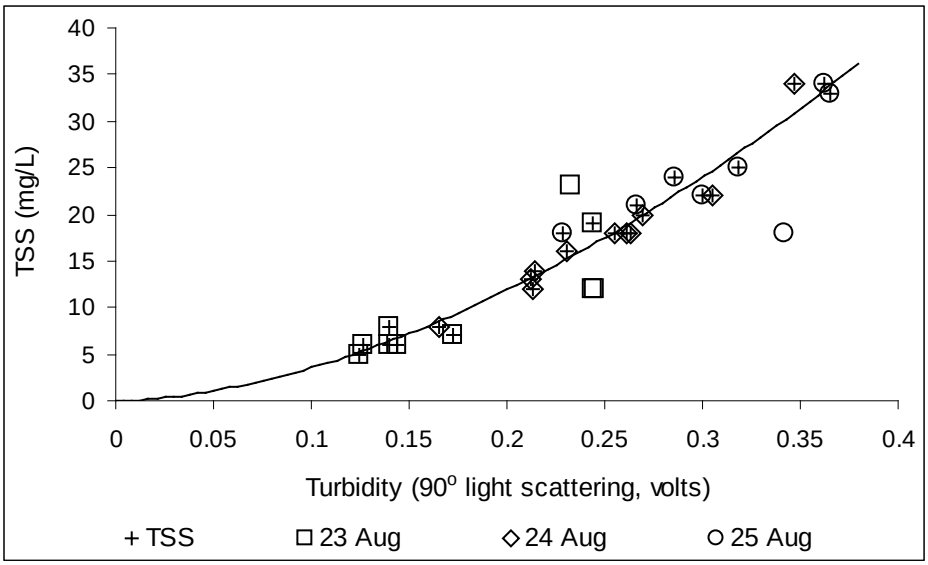

Figure 4. Plot of *TSS* versus S_{90}. Samples used to calculate the best fit (power) regression line used for *TSS* calibration are indicated by crosses (i.e. *TSS* in the legend). Three samples on 23 August and one on 25 August were excluded from the final regression calculation.

At sample stations on the cruise, spectral albedo distribution was measured using an Analytical Spectral Devices Inc. (ASD) FieldSpec® field radiation spectrometer. The ASD spectrometer measures integrated light intensity for 512 equal spectral intervals between 330-1065 nm. It was used to measure upwelling reflectance off the lake surface as a ratio of radiance over the target to radiance over a non-specular flat white $BaSO_4$ reflector, in this case always measured within 1-2 min. prior to reflectance measurement. Spectral albedo samples were taken with a 1^o foreoptic pointed vertically down from the side of a 7 m open boat, at a height of about 1 m. above the lake surface. A minimum of 100 spectral samples were taken at each station, with reference to the white reflector between each set of 10. Each sample was recorded over an integration time of 34-544 ms, depending on the ambient light level.

Transect and sample locations for the 1999 cruise were established by interpolation assuming a constant velocity between stations located by a Geographic Positioning System (GPS) on-board ship. In August 2000, a continuous time-location file was recorded by GPS. Geographical data were not differentially corrected. During the August 2000 cruise locations were recorded at 2 s intervals, and subsequently averaged over 1 m intervals. Based on a test of the GPS while docked for 2 h, precision of 1 m averages was +/-25 m (maximum apparent movement=25 m, mean apparent movement/minute=8 m, s.d.=5 m, n=120).

3.2.2 Flow, lake level, wind

Years for which complete data have been acquired for inflow, lake level, air temperature and wind are listed in Table 1.

Table 1. Years for which data available for environmental variables.

Year	**85**	**86**	**87**	**88**	**89**	**90**	**91**	**92**	**93**	**94**	**95**	**96**	**97**	**98**	**99**	**00**
Flow																
Saskatchewan R	X	X	X	X	X	X	X	X	X	X	X	X	X	X	X	X
Fairford R	X	X	X	X	X	X	X	X	X	X	X	X	X	X	X	
Red R	X	X	X	X	X	X	X	X	X	X	X	X	X	X	X	X
Winnipeg R - Pine Falls			X	X	X	X	X	X	X	X	X	X	X	X		
Winnipeg R - Slave Falls	X	X	X	X	X	X	X	X	X	X	X	X	X	X		
Lake Winnipeg level																
Georges Island	X	X	X	X	X	X	X	X	X	X	X	X	X	X	X	
Berens River	X	X	X	X	X	X	X	X	X	X	X	X	X	X	X	X
Gimli	X	X	X	X	X	X	X	X	X	X	X	X	X	X	X	X
3.2.2.1.1.1.1.1 Temperature																
Grand Rapids	X	X	X	X	X	X	X	X	X	X	X	X	X			
Berens River	X	X	X	X		X	X	X	X	X	X	X	X			
Beausejour	X	X	X	X	X	X	X	X	X	X	X	X	X			
Wind																
Norway House	X	X	X	X	X	X	X	X	X	X	X	X	X	X	X	X
Grand Rapids										X	X	X	X	X	X	X
Georges Island			X	X	X	X	X	X	X	X	X	X	X	X	X	
Berens River	X	X	X	X	X	X	X	X	X	X	X	X	X	X	X	X
Gimli	X	X	X	X	X	X	X	X	X	X	X	X	X	X	X	X

River discharge and lake level data for this study were abstracted from the HYDAT CD for years up to 1995. Data for subsequent years was purchased from the Water Survey of Canada. 1999 and 2000 flow data for the Saskatchewan River at Grand Rapids were contributed by Manitoba Hydro.

Only the Saskatchewan River record of discharges at Grand Rapids was complete to 2000. Red River discharge at Lockport was available only to the end of 1999. The record for the Winnipeg River at Pine Falls was complete only to the end of 1998. For 1985 and 1986, flow at Pine Falls was estimated by regression of monthly discharge with the upstream station at Slave Falls.

Lake Winnipeg level records at Berens River and Gimli were used to investigate correlation between TSS and instantaneous level, and between TSS and differences between North and South Basin level. One missing Berens River value was estimated using the Georges Island level record.

Daily weather data was downloaded from the Atmospheric Environment Service Canadian Daily Climate Data CD, with data up to 1997. Post-1997 temperature data was not acquired. The average May through August mean temperature for weather stations at Grand Rapids, Berens River and Beausejour was calculated as an indicator statistic of summer temperature. For the one station-year with missing data, Beausejour-1989, the mean summer value was calculated by regression with Grand Rapids summer temperature (r=0.96, Prob.=0.000, n=11).

Wind data for weather stations at Norway House, Grand Rapids, Georges Island, Berens River and Gimli, for the years 1985-2000, were purchased from the Atmospheric Environment Service of Environment Canada.

Several wind statistics were calculated and tested for correlation with AVHRR-derived TSS: means, 3rd quartiles and maximums for antecedent 6h, 2 d, 5 d and 7 d periods. The highest correlations were consistently found between TSS and wind measured over the antecedent 2 d.

3.3 Satellite data: Selection, calibration, NDVI calculation, DOS, land & cloud masking

3.3.1 Image Selection

Archived NOAA AVHRR images were obtained for the period 1985-2000. The temporal data was selected to meet a number of objectives. August imagery was obtained to study long term interannual trends in surface suspended solids quantity and patterns in L. Winnipeg; seasonal imagery (June–September) was used to quantify annual variation within the lake. The seasonal imagery were selected to include warm (1991) and cool (1992) summers, and, based on Red River discharges, high flow (1997, 1998) and low flow (1991, 1992) years.

To ensure that the best quality imagery was selected, hundreds of images were reviewed using NOAA's Satellite Active Archive (SAA) (http://www.saa.noaa.gov/), CCRS's Earth Observation Catalogue (CEOCat) (http://ceonet.ccrs.nrcan.gc.ca) and U.S. Geological Survey (USGS) Global Land Information System (GLIS) (http://edcwww.cr.usgs.gov/nfwebglis). Thumbnail images (Figure 5) were reviewed to assess image quality, the presence of haze and cloud, and position of the lake relative to nadir.

Images selected for the Lake Winnipeg study were typically near nadir to maximize radiometric and geometric quality of the images, cloud free, and if possible coincident with the period of relatively low winds (<15 km/hr) to minimize variability in TSS due to a particular weather event. All available imagery within 1-2 days of surface validation dates was acquired. Where cloud free imagery was not available for both the north and south basin simultaneously, multiple images were acquired. The selected images are

listed in Table 2. All purchased raw AVHRR data are archived on CDs accompanying this report. Times of overpass are listed and cloud cover over Lake Winnipeg is described in Table 3.

Figure 5. Thumbnail image as seen on CEOCat, August 23, 2000.

Table 2. Source information for NOAA AVHRR images obtained for this study.

3.3.1.1.1 Date	Orbit	Sat#	Source	3.3.1.1.2 Date	Orbit	Sat#	
19850726	3194	9	USGS	19960827	8555	14	SAA
19850824	3603	9	USGS	19970606	12548	14	SAA
19860812	8583	9	USGS	19970729	13296	14	SAA
19870820	4790	10	USGS	19970821	13620	14	SAA
19880815	18937	9	USGS	19970826	13691	14	SAA
19890815	24089	9	SAA	19970924	14100	14	SAA
19900821	9822	9	SAA	19980622	17924	14	SAA
19910621	14113	11	SAA	19980719	18305	14	SAA
19910713	14423	11	SAA	19980727	18418	14	SAA
19910811	14832	11	SAA	19980817	18714	14	SAA
19910920	15397	11	SAA	19980911	19067	14	SAA
19920615	19194	11	SAA	19990812	23795	14	SAA
19920722	19717	11	SAA	19990818	23879	14	SAA
19920816	20070	11	SAA	19990819	23894	14	SAA
19920818	20098	11	SAA	19990824	23964	14	SAA
19920911	20437	11	SAA	19990826	23992	14	SAA
19930820	25281	11	SAA	20000822	29102	14	SAA
19940810	30295	11	USGS	20000823	29116	14	SAA
19940819	30422	11	USGS	20000825	29145	14	SAA

19950821	3307	14	SAA	20000914	29427	14	SAA

Table 3. Overpass times of AVHRR imagery obtained for this study. X indicates images used to create TSS maps illustrated in Figure 11-19. Cloud-free area (%) is listed in columns 3-12 for polygons identified in Figure 20.

Image date/time (CST)	TSS maps illustrated in report	1 NR	1 OFF	2 NR	2a OFF	2b OFF	3	4	5	6	7
1985 Jul 26 14:36	X	100	100	100	100	100	93	100	100	100	100
1985 Aug 24 14:28	X	95	95	90	100	100	96	98	68	100	75
1986 Aug 12 15:18	X	59	47	72	66	90	89	93	34	33	89
1988 Aug 15 15:41	X	99	100	100	100	100	100	100	100	100	100
1989 Aug 15 12:27	X	0	0	0	0	0	19	4	93	96	100
1990 Aug 21 13:17	X	100	100	98	100	97	100	91	97	99	100
1991 Jun 21 13:36	X	100	100	100	100	100	100	100	100	100	100
1991 Jul 13 14:23	X	100	100	100	100	100	100	97	99	100	100
1991 Aug 11 13:52	X	100	100	100	100	100	97	98	100	100	100
1991 Sep 20 14:33	X	100	100	100	100	100	100	100	100	100	100
1992 Jun 15 13:34	X	100	100	100	100	100	100	100	99	100	90
1992 Jul 22 14:33	X	92	96	98	100	100	97	96	98	100	98
1992 Aug 16 14:35	X	24	14	66	17	98	99	100	100	100	100
1992 Sep 11 14:25	X	86	99	96	100	100	61	87	100	100	100
1993 Aug 20 15:31	X	100	100	100	100	100	100	100	97	100	100
1994 Aug 10 16:49		5	0	42	38	0	100	67	100	100	100
1994 Aug 19 16:42	X	87	99	91	95	100	100	100	100	100	100
1995 Aug 21 13:33	X	100	100	100	100	100	100	100	100	100	100
1996 Aug 27 13:20	X	100	100	100	100	100	100	78	100	100	100
1997 Jun 06 13:48	X	100	99	100	100	100	100	98	100	100	100
1997 Jul 29 14:12	X	100	100	100	100	100	100	100	100	98	98
1997 Aug 26 14:06	X	91	96	96	100	100	100	97	59	88	74
1997 Sep 24 13:49	X	99	100	99	100	96	100	100	100	100	100
1998 Jun 22 14:21	X	100	100	100	100	100	100	97	99	100	100
1998 Jul 19 14:24	X	71	86	99	100	100	97	98	79	9	19
1998 Jul 27 14:36		7	0	4	2	0	5	0	88	99	96
1998 Aug 17 14:03	X	100	100	99	100	99	96	100	100	100	100
1998 Sep 11 14:28	X	99	100	100	100	99	100	100	99	100	100
1999 Aug 12 15:45	X	77	91	92	100	99	59	98	87	11	0
1999 Aug 24 15:06	X	100	100	100	100	100	100	99	100	100	99
1999 Aug 26 14:43	X	97	99	97	100	100	97	95	100	100	100
2000 Aug 22 15:50	X	76	70	91	89	100	99	88	5	21	83
2000 Aug 23 15:38	X	100	100	100	100	100	99	98	63	74	98
2000 Sep 14 16:27	X	79	88	99	100	100	55	74	100	100	98

3.3.2 AVHRR data Calibration

3.3.2.1 **Radiance Top Of Atmosphere (TOA)**

Calibration of satellite imagery refers to the relationship between an integer value on a computer tape and the radiation field incident at the satellite instrument. The radiation field is expressed as spectral radiance (Wm^{-2} sr^{-1} μm^{-1}). Radiometric calibration is accomplished using the following equation (Teillet and Holben, 1994):

$$L_i = (D_i - D_{oi})/G_i$$

where: L = radiance ($Wm^{-2}sr^{-1}\mu m^{-1}$)
D = digital signal level (counts)
D_o = calibration offset coefficient (counts) (Table 5-7)
G = calibration gain coefficient [counts/(Wm^{-2} sr^{-1} μm^{-1})]
and subscript i refers to AVHRR channel 1 or 2.

Channel 1 and 2 AVHRR imagery was calibrated to normalized effective albedo (percent) for Channels 1 and 2. The effective albedo in percent is defined as (Teillet and Holben, 1994):

$$A_i = \gamma_i(D_i - D_{oi})$$
$$= \gamma_i D_i - \delta_i$$

where: $\gamma_i = 100\pi / (E_{oi}G_i) = 100\pi\alpha_i/E_{oi}$
$\delta_i = -\gamma_i D_{oi}$

E_{oi} = exoatmospheric solar irradiance (Wm^{-2} μm^{-1}) for channel i (Table 4).
$\alpha_i = 1/G_i$ where G_i = calibration gain coefficient counts/(Wm^{-2} sr^{-1} μm^{-1})
γ_i = calibration gain coefficient
δ_i = calibration offset coefficient

The time dependent gains and offsets as described by Teillet and Holben (1994) are computed daily using the equations above and the parameters listed in Tables 5-7.

Table 4. Exo-atmospheric solar irradiances and equivalent bandwidths for AVHRR channels 1 and 2 (Teillet and Holben, 1994). Units: (Wm^{-2} μm^{-1}) $\Delta\lambda(\mu m)$

NOAA	Channel 1	Channel 2	Channel 1	Channel 2
6	1642	1048	0.109	0.223
7	1644	1052	0.108	0.249
8	1623	1056	0.113	0.230
9	1635	1054	0.117	0.239
10	1656	1043	0.108	0.222
11	1629	1053	0.113	0.229
12	1613	1050	0.124	0.219
14*	1605	1029	0.129	0.244

*URL: http://www.ccrs.nrcan.gc.ca/ccrs/tekrd/rd/ana/calval/noaa14e.html

Table 5. Coefficients for piecewise linear representations of the time dependence of AVHRR calibration gain and offset coefficients, NOAA 9, channels 1 and 2. Gain = A*(day#) + B and offset = C*(Day #) + D; Radiance is in units of Wm^{-2} sr^{-1} μm^{-1} (Teillet and Holben, 1994).

Launch Date	NOAA 9	Band	A (counts/ radiance)/ day	B (Counts/ radiance)	C (Counts/ day)	D (Counts)
12/12/1984	1985	1	-0.000323	1.76	-0.000185	38.0
	1985	2	-0.000364	2.52	-0.00153	40.3
	1986	1	-0.000264	1.74	-0.000201	38.0
	1986	2	-0.000277	2.49	-0.00109	40.1
	1987	1	-0.000205	1.69	-0.000216	38.0
	1987	2	-0.000192	2.42	-0.000658	39.8
	1988	1	-0.000147	1.63	-0.000232	38.0
	1988	2	-0.000107	2.33	-0.000226	39.3

Table 6. Coefficients for piecewise linear representations of the time dependence of AVHRR calibration gain and offset coefficients, NOAA 11, channels 1 and 2. Gain = A*(day#) + B and offset = C*(Day #) + D; Radiance is in units of Wm^{-2} sr^{-1} μm^{-1} (Teillet and Holben, 1994).

Launch Date	NOAA 11	Band	A (counts/radiance /day	B (Counts/ radiance)	C (Counts/ day)	D (Counts)
24/09/1988	1988	1	0	1.77	0	40.0
	1988	1	-0.00028	1.72	0	40.0
	1988	2	0	2.64	0	40.0
	1988	2	-0.000838	2.67	0	40.0
	1989	1	-0.000133	1.71	0	40.0
	1989	2	-0.000462	2.63	0	40.0
	1990	1	0.0001	1.6	0	40.0
	1990	2	0.000132	2.36	0	40.0
	1991	1	0.000333	1.41	0	40.0
	1991	2	0.000726	1.87	0	40.0
	1992	1	0.0000201	1.666	-0.0002435	40.24
	1992	2	0.00003288	2.41	-0.0004842	40.43
	1993	1	0.00002804	1.654	0.0003825	39.26
	1993	2	-0.00004584	2.533	0.0008901	38.29
	1994	1	-0.00005601	1.815	0	40.0
	1994	2	-0.00013	2.701	0	40.0

Table 7. Coefficients for piecewise linear representations of the time dependence of AVHRR calibration gain and offset coefficients, NOAA 14, channels 1 and 2. Gain = A*(day#) + B and offset = C*(Day #) + D; Radiance is in units of Wm^{-2} sr^{-1} μm^{-} (Teillet and Holben, 1994).

Launch Date	NOAA 14	Band	A (counts/radiance /day	B (Counts/ radiance)	C (Counts/day)	D (Counts)
30/12/1994	1995	1	0	1.81	0	35.8
	1995	2	0	2.8	0	33.7
	1996	1	-0.0003047	1.778	0	41
	1996	2	-0.0005088	2.324	0	41
	1997	1	-0.0002671	1.75	0	41
	1997	2	-0.0004275	2.265	0	41
	1998	1	-0.0002356	1.715	0	41
	1998	2	-0.0003644	2.196	0	41
	1999	1	-0.0001209	1.587	0	41
	1999	2	-0.00003714	1.883	0	41
	2000	1	-0.0001249	1.639	0	41
	2000	2	-0.00003837	1.946	0	41

3.3.2.2 Reflectance Top Of Atmosphere (Retoa)

TOA reflectance for channel 1 or 2 is calculated from corrected TOA radiance, L^*_i, with the following formula (Teillet, 1992):

$$\rho_i^* = \frac{\pi d_s^2 * L_i^*}{E_{0,i} \cos\theta_s}$$

where:

ρ_i^* is the top-of-the-atmosphere reflectance
θ_s is solar zenith angle (degrees);
d_s is the Earth-Sun distance (Astronomical Units); (eg., 1.010822)
E_0 is the exo-atmospheric solar irradiance ($Wm^{-2}um^{-1}$); (Table 4).
L_i^* is the radiance ($Wm^{-2}sr^{-1}um^{-1}$);
The subscript i refers to AVHRR channel number (1 or 2).

3.3.2.3 Atmospherically Corrected Surface Reflectance

Radiometric correction for atmospheric effects was made using an algorithm called SMAC (Rahman and Dedieu, 1994) to account for two-way gaseous transmission and for Rayleigh as well as aerosol scattering. The algorithm requires vertically integrated gaseous contents and the aerosol optical depth at 550 nm for each pixel. Input parameters typical of continental type climates are listed in Table 8. For the purposes of this study a standard continental atmosphere was assumed as detailed information of atmospheric parameters were unavailable. NOAA AVHRR scenes were further radiometrically corrected using dark object corrections (see below).

Table 8. General SMAC input Parameters for typical continental atmosphere

Input Parameters	**Value**
Delta	0.0139
AerosolOpticalDepthAt550nm	0.06
TotalWaterVapourContent	2.3 g/cm2
TotalOzoneContent	0.319 cm-atm
Band-specific SMAC input parameters: (1,2)	
WaterTransmissionCoefficients	-0.009067, 0.691401
OzoneTransmissionCoefficients	-0.076979, 0.989521
CarbonDioxideTransmissionCoefficients	0.0, 0.0
AtmosphericSphericalAlbedoCoefficients	1.055854 0.224353
TotalAtmosphericTransCoefficients	1.086792, -0.188651, -0.217220
RayleighOpticalDepth	0.05321
AerosolOpticalDepthCoefficients	-1.00e-06, 0.84175
AerosolScatteringAlbedo	0.88630
AerosolAssymetryFactor	0.63315
AerosolPhaseFunctionCoefficients	1.7723 -2.4268e-02 9.2084e-05

Surface reflectances were calculated using the top of atmosphere reflectance in channel 1 and 2 data. To take into account variations in illumination geometry within and between scenes satellite zenith angle (θ_v), solar zenith angle (θ_s), relative azimuth angle (θ)(the angle between θ_s and θ_v) are incorporated in the formulation(Rahman, H., and G. Dedieu, 1994).

3.3.2.4 NDVI

To examine the distribution of chlorophyll within the lake Winnipeg basin a normalized difference vegetation index (NDVI) was computed. Vegetation indices are designed to detect and quantify green biomass. Although typically used to map terrestrial vegetation, NDVI was adopted to map chlorophyll in the aquatic environment.

The NDVI values were calculated using the surface reflectance data ρ_i^* (channels 1 and 2..

$$NDVI = \frac{(\rho_2^* + \rho_1^*)}{(\rho_2^* - \rho_1^*)}$$

3.3.3 Dark-object subtraction (DOS)

More radiance measured by an orbiting sensor is due to atmospheric path radiance than to radiance from the earth's surface. While discreet cloud-cover can be identified and mapped, temporal (between image) variations in this atmospheric contribution may, if not corrected, exceed variations in lake surface radiance.

A common procedure for normalization of atmospheric path radiance and water volume reflectance (i.e. water with TSS=0) in suspended sediment studies is subtraction of the radiance (or albedo) of the darkest pixel. If both can considered to be spatially homogeneous throughout the study area, then this normalization corrects for both atmospheric and water volume reflectance simultaneously. This procedure treats a clear water body as a standard reflector with zero reflectance due to suspended sediment (Philpot and Klemas, 1979; Chagarlamudi, 1980).

In this study, we retrieved the darkest albedo recorded over a set of 34 lakes, mostly in the Precambrian Shield to the north, east and southeast of Lake Winnipeg. The north basin of Lake Winnipeg was included in this set. The minimum AVHRR Channel 1 albedo recorded in this set of lakes, in all images, was 0.3%. Hence, we corrected all images by subtracting the difference between individual image dark lake minima and 0.3% (Table 9). This effectively resets the minimum calibrated albedo in the image to the theoretical at-lake-surface albedo (for the Lake Winnipeg region, for that day) over a clear (TSS=<1 $mg \cdot L^{-1}$) lake.

This minimum value, 0.3% represents the sum of atmospheric and water volume albedo over clear water. The minimum albedo over the north basin of Lake Winnipeg, for all images, was 0.7%, indicating that the volume reflectance over Lake Winnipeg is rarely, if ever, as low as over the clearest nearby lakes.

The minimum albedo measured by shipboard field spectrometer in a cruise over the whole of Lake Erie by one of the authors (McCullough, 1998) was 0.5% in the spectral range recorded by AVHRR Channel 1 sensor (580-680 um). This was at a site where *TSS*=1 $mg \cdot L^{-1}$ (the analytical detection limit and therefore an approximate value). The minimum of 0.7% for Lake Winnipeg seems reasonable by comparison to this Lake Erie value.

Table 9. Value subtracted (dark object subtraction value=DOS) from each AVHRR Channel 1 and Channel 2 calibrated albedo to calculate $A_{1,DOS}$. Values are %*100 (Calibrated albedo in the AVHRR images is recorded as %*100.)

Image overpass date	CH1	CH2	Image overpass date	CH1	CH2
1985 Jul 26	105	13	1995 Aug 21	86	78
1985 Aug 24	94	24	1996 Aug 27	0	16
1986 Aug 12	136	24	1997 Jun 06	27	4
1988 Aug 15	73	23	1997 Jul 29	40	1
1989 Aug 15	83	20	1997 Aug 26	88	4
1990 Aug 21	60	12	1997 Sep 24	30	14
1991 Jun 21	13	7	1998 Jun 22	39	24
1991 Jul 13	86	0	1998 Jul 19	92	58
1991 Aug 11	98	32	1998 Jul 27	137	111
1991 Sep 20	53	0	1998 Aug 17	25	49
1992 Jun 15	456	282	1998 Sep 11	55	26
1992 Jul 22	148	126	1999 Aug 12	116	39
1992 Aug 16	223	143	1999 Aug 24	32	17
1992 Sep 11	218	172	1999 Aug 26	36	62
1993 Aug 20	16	30	2000 Aug 22	17	25
1994 Aug 10	454	13	2000 Aug 23	10	20
1994 Aug 19	34	13	2000 Sep 14	50	16

3.3.4 Land and Cloud Masking Procedure

A mask was prepared using a digital shoreline map of Lake Winnipeg with a 2 km buffer into the lake, thereby removing from further analysis all data less than 2 AVHRR pixels from shore. This is a precaution used to eliminate potential elevation of apparent lake albedo by radiance "drift" from adjacent land pixels. The land mask including 2 km buffer includes all islands on a 1:1,000,000 map, making the effective diameter of even small islands at least 5x5 km, and eliminating water in, for instance, much of the Narrows.

Cloud cover over Lake Winnipeg was masked to ensure data integrity with regards to mapping of TSS. AVHRR channels 1 (580-680 nm), 2 (725-1100 nm) and 4 (10.30-11.30μm) were used as inputs to identify cloud versus water/land background. Channel 1 provided good contrast between clouds and vegetated land surfaces, channel 2 (NIR) provided a good contrast between water (dark target) vs. cloud, and the channel 4 (thermal) was able to best detect the more subtle cloud contamination that was not readily identifiable in channels 1 and 2.

An unsupervised classification approach was adopted to identify cloud cover. This method employed an iterative optimization clustering procedure (migrating means technique) based on the isodata algorithm develop by Ball and Hall (1965). This approach, although computationally intensive provided a robust method of identifying cloud cover. To further enhance the ability of the clustering algorithm to discriminate the subtleties of cloud cover versus turbid water within Lake Winnipeg, a Boolean land mask was applied to each image prior to classification to mask all land and water surfaces outside the basin. All classes identified in multi-spectral space where therefore directly related to either water or cloud within Lake Winnipeg. Since the classification procedure was unsupervised, classes (water vs. cloud) were manually assigned to ultimately create a cloud mask unique to each image

3.3.5 Map projection

For all mapping, the Lambert conformal conic projection was used. This projection is suitable for large areas in mid-latitudes by minimizing distortion, maintaining shape, and bearings. This is a common projection for remote images which cover large areas and are used to form mosaics for large countries like Canada. A common coordinate system, the Universal Transverse Mercator, is not well suited to map an area as large as Lake Winnipeg as deformation becomes evident.

3.4 Estimation of TSS by AVHRR albedo

3.4.1 Development of an albedo-TSS model

An excellent cloud-free image of Lake Winnipeg was obtained on 23 August 2000, during the 22-25 August cruise. We used TSS data derived from the continuous-flow turbidity meter record to determine a model for estimation of TSS from AVHRR Channel 1 dark-objected subtracted albedo ($A_{1,DOS}$). Because this is a geographically continuous set, there is undoubtedly spatial autocorrelation in the data, the precision of the model was tested using paired AVHRR and on-lake sample data from different dates. The statement of precision thus derived incorporates both within-image and between-image atmospheric variability.

TSS measured on the August 2000 cruise ranged from 5-42 $mg \cdot L^{-1}$ (Figures 6 and 7). The range of test data available is slightly larger: 2.5-59 $mg \cdot L^{-1}$. TSS predicted by AVHRR images over Lake Winnipeg, using this model range from <1 $mg \cdot L^{-1}$north of Long Point to >100 $mg \cdot L^{-1}$ in plumes along the northeast shore.

TSS derived from the continuous flow turbidity meter along the August 2000 cruise track is compared in Figure 6 with TSS derived from two AVHRR images, acquired on 22 and 23 August. Note that TSS is plotted against time, and that the continuous flow record continued when the ship was at rest. Apparent gaps in AVHRR data are associated with these station sampling stops. The surface data of 23 August is the most coincident with the AVHRR-derived TSS shown. In general, local maxima and minima in the AVHRR-derived TSS are coincident with those in the surface data, although the peak encountered while stopped sampling at 13:00-14:00 h is missing from the AVHRR record.

It is also of note that TSS derived from the two AVHRR scenes is highly coincident both in pattern and absolute value, except in the late afternoon of 24 August. This section of poorer fit is in the Berens Island –north Narrows region. It was apparent during the cruise that this is hydraulically dynamic region. It is unsurprising that surface sediments should have moved in the 24 h between the times of the two satellite overpasses, and between both overpass and the time the region was sampled. In the scatter plot of TSS versus $A_{1,DOS}$, the high scatter for mid-range TSS (Figure 7) is mostly from the this region.

On the other hand, the pattern in the continuous flow and filtration data recorded on the morning of 25 August are moderately well matched by the pattern indicated by AVHRR (Figure 6) in spite of strong southerly winds on the morning of 24 August. In fact, the relatively turbid plume represented by the broad peak in the continuous flow meter plot at 10:00 to 11:00 on the 25th may have drifted several kilometers southward subsequent to the time of the AVHRR image, the 23rd, but it is fairly similarly represented by both

instruments. This is useful to remember, because this South Basin data anchors the upper end of the calibration equation developed from the cruise data.

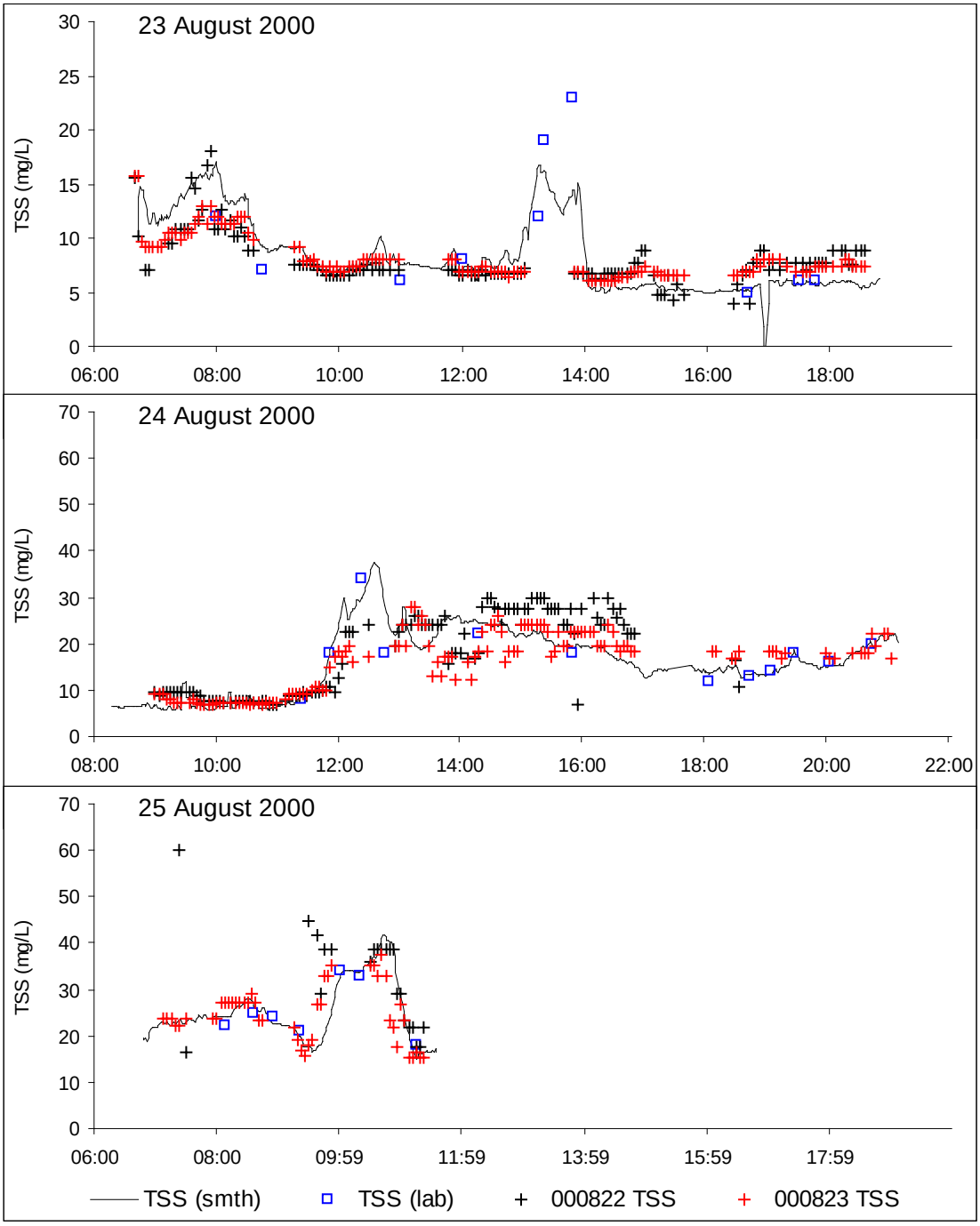

Figure 6. Turbidity-derived TSS (smth=running mean of 3), TSS by filtration (TSS lab) and TSS estimated by both 22 and 23 August AVHRR for the 23-25 August cruise transect. The 23 August image was acquired at 14:38 CDST. Apparent gaps in AVHRR data are associated with times when the ship was at rest for sampling.

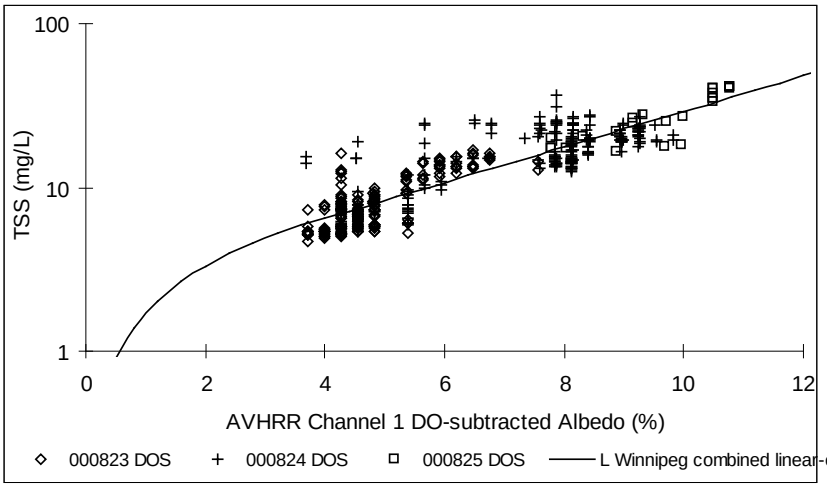

Figure 7. Plot of TSS versus $A_{1,DOS}$ for the August, 2000 Cruise. TSS are estimates from continuous-flow turbidity meter data. The model is a combination of linear interpolation for $A_{1,DOS} < 3.5\%$ and the best fit exponential regression line between TSS and $A_{1,DOS}$.

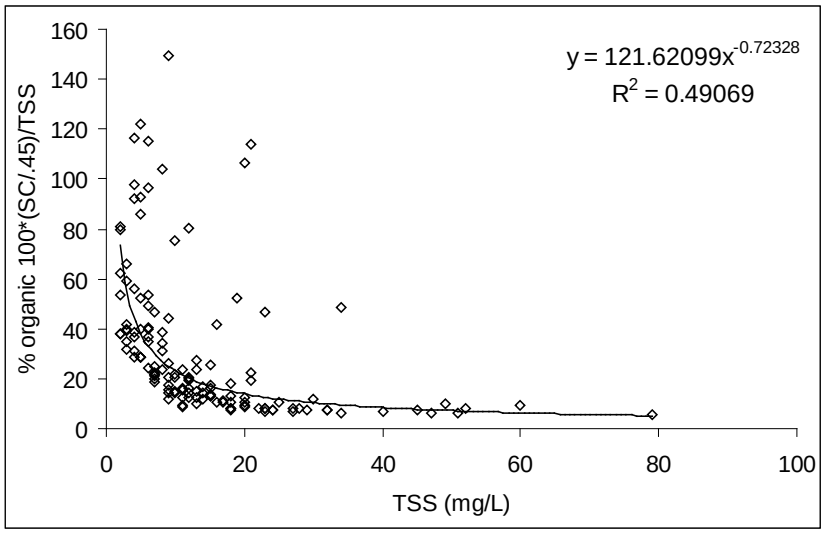

Figure 8. Organic fraction of TSS (%). Computed as 100 * (SC/0.45) / TSS where SC=suspended carbon (mg/L) and TSS=total suspended solids (mg/L). (Data contributed by M. Stainton.) Inherent in this computation is the assumption that organic matter is 45% carbon by weight. Scatter about the best fit power relationship is skewed above the regression line, and some computed % organic exceeds 100%. This would be the result expected if 45% (C in organic matter) is the mean of a skewed distribution with the greater range below the mean (a reasonable assumption because C in organic matter is most frequently in combination with at least one (heavier) oxygen atom and several hydrogen atoms, and therefore does not exceed 45% by weight of the most common organic molecules).

The relationship between light upwelling from water bodies and TSS, whether measured as radiance or albedo, has frequently been shown to be exponential at high TSS (e.g. Munday and Alfoldi, 1979, Stumpf, 1987). The best fit of $A_{1,DOS}$ regressed against 23-25 August TSS is exponential. However, the exponential fit overestimates low TSS and in fact would estimate 2.4 $mg \cdot L^{-1}$ at zero albedo, an impossible value. We chose to fit by eye a linear extension to the exponential model (Figure 7).

The linear extension passes through 1 $mg \cdot L^{-1}$ at albedo=0.5%. This value was chosen based on earlier research on Lake Erie. The minimum albedo integrated over wavelengths 580-680 nm (the spectral range of AVHRR Channel 1) measured by shipboard field spectrometer in a cruise over Lake Erie by one of the authors (McCullough, 1998) was 0.5% in the spectral range recorded by AVHRR Channel 1 sensor (580-680 um). This was at a site where TSS=1 $mg \cdot L^{-1}$ (the analytical detection limit and therefore an approximate value). The upper end of the linear range was selected to strike the exponential curve tangentially, at approximately TSS=6 $mg \cdot L^{-1}$. and albedo=3.5%.

It is not unreasonable to expect a shift in the relationship between TSS and albedo at low TSS. For Lake Winnipeg suspended solids, in the range 5-15 $mg \cdot L^{-1}$ the organic fraction begins to rise steeply from 5-15% to 20-100%. This pattern has also been shown on Lake Erie (McCullough, 1998, Figure 16) and by Stumpf (1987) in Chesapeake Bay. He derived a complex expression from consideration of interaction of backscatter and absorption which is exponential at high TSS but which drops off steeply at TSS<10 $mg \cdot L^{-1}$. By iterative estimation of reasonable backscatter and absorption coefficients, his curve can be made to follow approximately the model line shown in Figure 7.

The model used to estimate TSS and shown in Figure 7 is as follows:

IF $100 \cdot A_{1,DOS} < 350$

THEN $TSS = 0.0160\ 100 \cdot A_{1,DOS} + 0.1000$

ELSE $TSS = 2.38115552e^{(0.00250177\ 100.A1,DOS)}$

where

TSS = total suspended solids measured by filtration (GFC, nominally 1.1. um, $mg \cdot L^{-1}$)

$100 \cdot A_{1,DOS}$ = AVHRR Channel 1 albedo after dark-object subtraction (note that 100 times albedo is used in this expression. This is because calibrated albedo in the Idrisi raster files used to map TSS are recorded as 100 times %: i.e. albedo=3.5% is stored in the raster images as the integer 350, and the break between linear and exponential expressions in the model occurs at 3.5%.

3.4.2 Tests of TSS prediction by AVHRR

The model tends to overestimate TSS on other dates, by an average of 1.8 $mg \cdot L^{-1}$ (s.d.=5.7 $mg \cdot L^{-1}$, n=39. AVHRR images on 12, 24 and 26 August 1999 and 22 August 2000) (Figure 9). If only 4 outliers are removed, the average overestimation drops to 0.7 $mg \cdot L^{-1}$, although the standard deviation (=4.8 $mg \cdot L^{-1}$, n=35) remains high..

The model is robust enough to predict Lake Erie TSS at least as well (Figure 10). For a larger sample, derived from direct filtration measurements (n=13), Secchi transparency (n=90) and beam transmissometer measurements (n=43) collected over a 20 y period, the average error of prediction was 0.4 $mg \cdot L^{-1}$ (also overestimation, s.d.=1.9 $mg \cdot L^{-1}$, n=114. There was some overlap between Secchi and beam transmissometer measurements). The error is most probably smaller than for the Lake Winnipeg data only because most of the Lake Erie data was for TSS<10 $mg \cdot L^{-1}$.

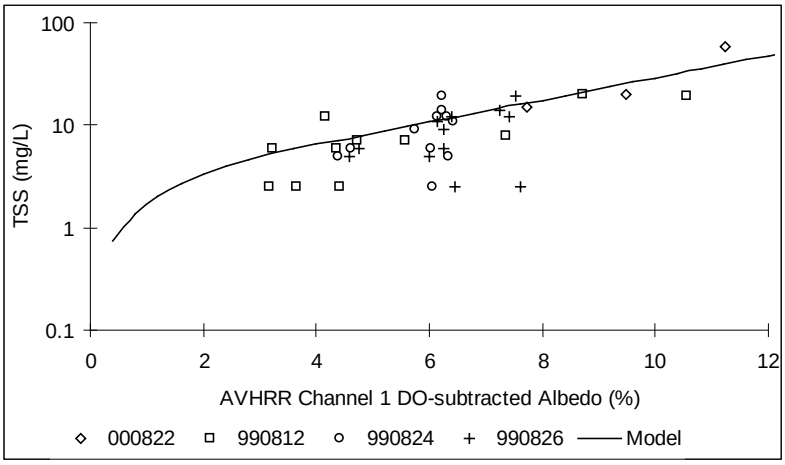

Figure 9. TSS versus $A_{1,DOS}$ for samples on 12, 24 and 26 August 1999 and 22 August 2000. Line is the Lake Winnipeg linear-exponential model.

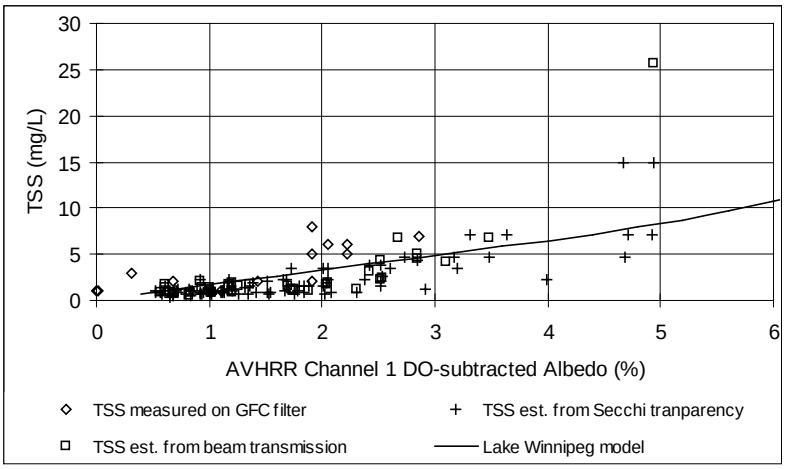

Figure 10. TSS versus $A_{1,DOS}$ for samples taken on Lake Erie. Line is the Lake Winnipeg linear-exponential model.

3.5 Statistical methods

3.5.1 Descriptive statistics

Maps were prepared of the mean, maximum, minimum and standard deviation of TSS. Images were selected to represent mid-late summer, and range from 22 July to 27 August.

The mean, are for 15 of the 16 years in the series 1985-2000 (Table 9). No midsummer cloud-free image was obtained for 1987. Only >85% cloud-free images were included. Clouds were masked, i.e. given the value zero, in individual maps, but mean, minimum and maximum TSS are mapped for the whole lake. Because statistics were calculated on only cloud-free pixels, the sample number varies slightly among pixels, with the number of images used in the calculation being the maximum sample number.

This is not the case for standard deviation, for which only pixels which are cloud-free in all images are shown on the resulting map. Hence, for all pixels, the sample number is the number of images used in the calculation. Because clouds cover is additive in calculating the standard deviation, a smaller sample number, 12, was achieved.

Table 10. Dates of AVHRR images used to calculate maps of descriptive statistics for Lake Winnipeg at mid-late summer for the period 1985-2000.

Images used to calc. max. and min.	Images used to calc. mean and s.d.	% cloud-free over L. Winnipeg
1985 Jul 26	1985 Jul 26	100
1986 Aug 12		44
1988 Aug 15	1988 Aug 15	99
1989 Aug 15		12
1990 Aug 21	1990 Aug 21	97
1991 Aug 11	1991 Aug 11	100
1992 Jul 22		94
1993 Aug 20	1993 Aug 20	100
1994 Aug *a	1994 Aug *a	95
1995 Aug 21	1995 Aug 21	100
1996 Aug 27	1996 Aug 27	97
1997 Aug *b	1997 Aug *b	98
1998 Aug 17	1998 Aug 17	99
1999 Aug 24	1999 Aug 24	100
2000 Aug 23	2000 Aug 23	95

a. 1994 image is a composite of 10 and 19 August 1994 data.
b. 1997 image is a composite of 21 and 26 August 1997 data.

3.5.2 Correlation

Maps showing correlation between TSS and environmental variables were calculated in a manner analogous to the calculation of standard deviation. That is, the sums of squared deviations from the mean, and the cross-products were calculated only for pixels which were cloud-free in all images. As for standard deviation, images for use in these calculations had to be chosen with this in mind, in order to minimize the loss of coverage due to cloud. The sample number associated with each pixel in maps of correlation coefficients is always equal to the total number of images analyzed.

Overpass dates for AVHRR images used in creating correlation coefficient maps are listed in Table 10.

Table 11. AVHRR images used to calculate correlations between TSS and environmental variables. N=10 in 2nd summer set because 1998-2000 summer temperature was not acquired. For 1994, two images are combined to achieve maximum cloud-free area.

Mid-late summer (n=12)	**Mid-late summer (n=10)**	**June-Sept set (n=20)**
1985 Jul 26	1985 Aug 24	1985 Jul 26
1988 Aug 15	1988 Aug 15	1988 Aug 15
1990 Aug 21	1990 Aug 21	1990 Aug 21
1991 Aug 11	1991 Aug 11	1991 Jul 13
1993 Aug 20	1992 Jul 22	1991 Aug 11
1994 Aug 10 & 19	1993 Aug 20	1991 Sep 20
1995 Aug 21	1994 Aug 10 & 19	1992 Jun 15
1996 Aug 27	1995 Aug 21	1992 Jul 22
1997 Jul 29	1996 Aug 27	1993 Aug 20
1998 Sep 11	1997 Aug 26	1994 Aug 19
1999 Aug 24		1995 Aug 21
2000 Aug 23		1997 Jun 06
		1997 Jul 29
		1997 Sep 24
		1998 Jun 22
		1998 Aug 17
		1998 Sep 11
		1999 Aug 24
		1999 Aug 26
		2000 Aug 23

4 RESULTS

4.1 Maps of TSS

Figures 11 to 19 are maps of TSS on Lake Winnipeg calculated from AVHRR Channel 1 dark-object corrected albedo. Grey areas on the images indicate cloud cover. TSS rounded to integer values is shown by different colours in 1 $mg \cdot L^{-1}$ increments up to 30 $mg \cdot L^{-1}$. TSS>30 $mg \cdot L^{-1}$ is indicated by dark brown. Lake level and hourly wind speed and direction (at Georges Island) for the day of each image is listed in Table 12 and 13.

Table 12. Winds for 6h and 2 d antecedent to each satellite overpass. V=mean speed (km/h), dir=mean direction (degrees/10 azimuth). S.d.=standard deviation of direction.

	Georges Island						Gimli					
Overpass date	V 6h	dir 6h	dir s.d. 6h	V 2d	dir 48h	dir s.d. 48h	V 6h	dir 6h	dir s.d. 6h	V 2d	dir 48h	dir s.d. 48h
1985 Jul 26							9	10	2	9	25	10
1985 Aug 24							8	13	14	6	14	12
1986 Aug 12							16	21	1	8	19	9
1987 Aug 20							10	17	10	9	24	7
1988 Aug 15	15	19	8	12	22	8	20	22	4	10	22	10
1989 Aug 15	9	28	1	13	16	12	6	6	4	9	20	14
1990 Aug 21	26	22	1	14	18	2	9	16	3	7	12	7
1991 Jun 21	15	8	1	21	17	14	17	4	2	19	8	9
1991 Jul 13	7	20	2	18	19	14	9	9	1	13	11	12
1991 Aug 11	21	19	1	18	17	2	6	9	3	7	16	7
1991 Sep 20	42	20	1	32	22	12	20	18	2	15	23	4
1992 Jun 15	7	10	4	16	22	12						
1992 Jul 22	25	23	0	18	25	4						
1992 Aug 16	20	25	6	18	19	3						
1992 Aug 18	13	28	2	20	30	3						
1992 Sep 11	42	18	0	26	12	6						
1994 Aug 10	13	11	14	16	24	6	3	11	16	6	16	12
1994 Aug 19	9	17	11	11	17	13	18	14	16	10	18	15
1995 Aug 21	16	31	2	33	29	3	9	28	13	19	28	5
1996 Aug 27	31	24	2	24	21	6	27	21	1	13	19	7
1997 Jun 06	7	17	5	20	23	12	10	6	3	15	11	14
1997 Jul 29	11	23	3	14	21	12	9	14	3	10	22	14
1997 Aug 21	6	12	17	19	26	12	11	14	17	12	24	11
1997 Aug 26	29	32	0	23	23	8	14	32	1	17	23	8
1997 Sep 24	25	27	0	27	21	8	24	27	1	20	22	8
1998 Jun 22	17	32	0	25	31	9	14	20	15	17	26	7
1998 Jul 19	23	31	2	15	22	8	17	30	2	12	21	9
1998 Jul 27	14	24	3	28	26	5	20	29	1	18	26	5
1998 Aug 17	8	15	13	28	15	13	17	6	1	21	18	11
1998 Sep 11	13	32	1	23	25	8	16	19	18	18	23	10
1999 Aug 12	15	32	1	17	27	11	18	5	2	12	22	14
1999 Aug 18	10	17	8	13	20	9	9	35	2	9	21	14
1999 Aug 19	21	21	2	16	21	4	11	25	1	8	22	11
1999 Aug 24	24	18	0	17	22	9	8	11	6	8	20	12
1999 Aug 26	21	24	2	28	19	5	21	34	1	20	20	6
2000 Aug 22	16	28	1	18	22	6	19	24	2	19	23	4
2000 Aug 23	21	18	1	17	24	3	16	23	1	13	25	4
2000 Aug 25	22	34	2	22	25	7	14	24	16	14	25	8
							21	34	1	14	30	3

Table 13. Lake Winnipeg level at Berens River and at Gimli, and the difference (Gimli-Berens) on the dates of satellite overpasses. Units: m above M.S.L.

Date	Berens R	Gimli	Gimli - Berens
1985 Jul 26	217.662	217.769	0.107
1985 Aug 24	217.804	217.846	0.042
1986 Aug 12	217.842	217.645	-0.197
1988 Aug 15	217.010	216.988	-0.022
1989 Aug 15	217.403	217.437	0.034
1990 Aug 21	217.598	217.604	0.006
1991 Jun 21	217.165	217.273	0.108
1991 Jul 13	217.214	217.265	0.051
1991 Aug 11	217.210	217.206	-0.004
1991 Sep 20	217.023	216.783	-0.240
1992 Jun 15	217.530	217.576	0.046
1992 Jul 22	217.748	217.671	-0.077
1992 Aug 16	217.826	217.738	-0.088
1992 Sep 11	217.818	217.566	-0.252
1993 Aug 20	217.861	217.904	0.043
1994 Aug 10	217.724	217.747	0.023
1994 Aug 14	217.710	218.065	0.355
1994 Aug 19	217.668	217.780	0.112
1995 Aug 21	217.642	217.847	0.205
1996 Aug 27	217.840	217.506	-0.334
1997 Jun 06	218.116	218.225	0.109
1997 Jul 29	217.908	217.959	0.051
1997 Aug 21	217.771	217.883	0.112
1997 Aug 23	217.775	217.671	-0.104
1997 Aug 26	217.785	217.932	0.147
1997 Sep 24	217.707	217.576	-0.131
1998 Jun 22	217.889	218.051	0.162
1998 Jul 19	217.879	218.031	0.152
1998 Jul 23	217.857	218.064	0.207
1998 Jul 27	217.832	217.965	0.133
1998 Aug 17	217.701	217.836	0.135
1998 Sep 11	217.594	217.740	0.146
1999 Aug 12	217.710	217.818	0.108
1999 Aug 24	217.690	217.723	0.033
1999 Aug 26	217.775	217.530	-0.245
2000 Aug 22	217.840	217.832	-0.008
2000 Aug 23	217.822	217.815	-0.007
2000 Sep 14	217.766	217.977	0.211

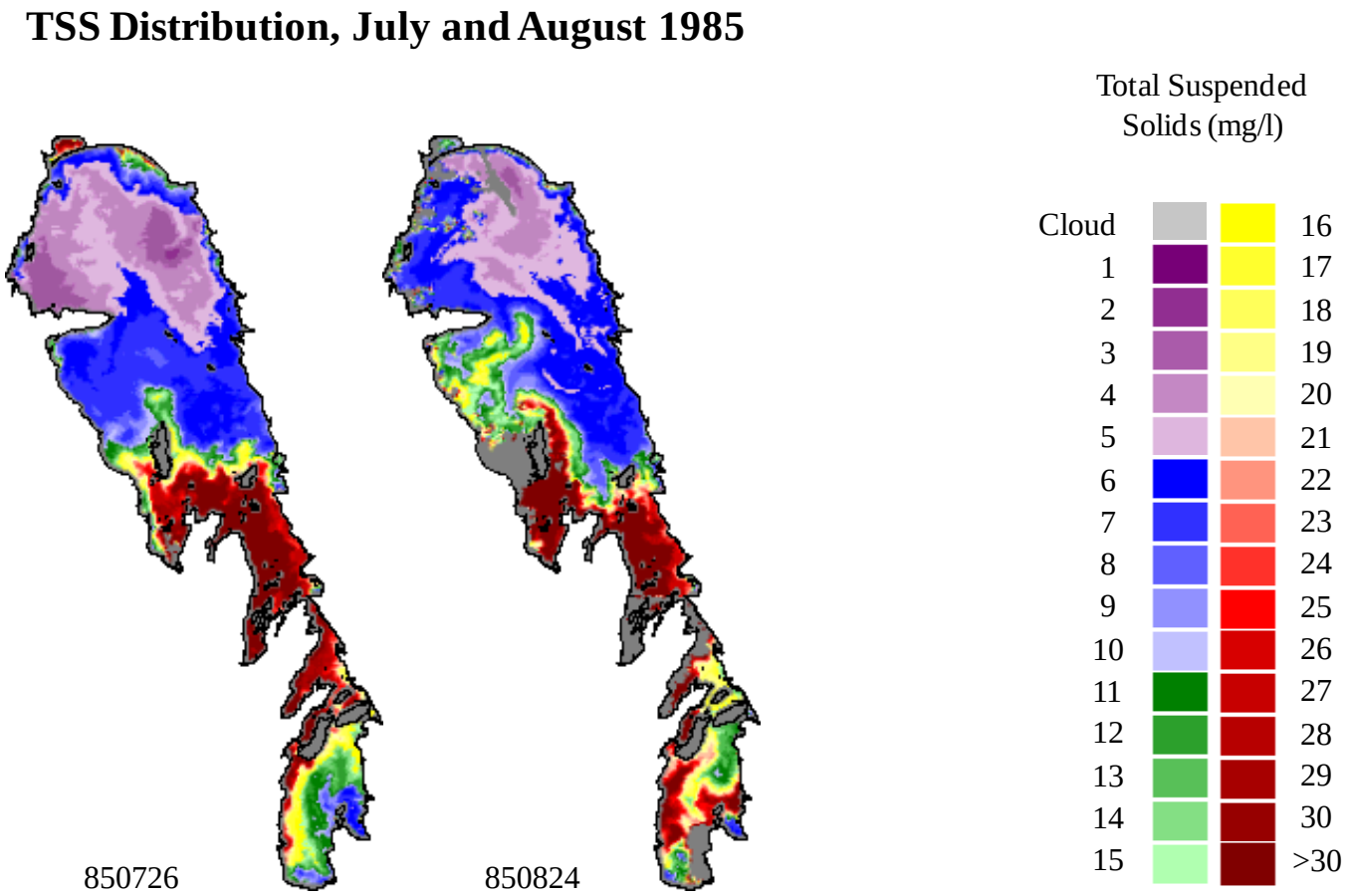

Figure 11. Total suspended solids (TSS) determined from NOAA AVHRR data, July and August 1985.

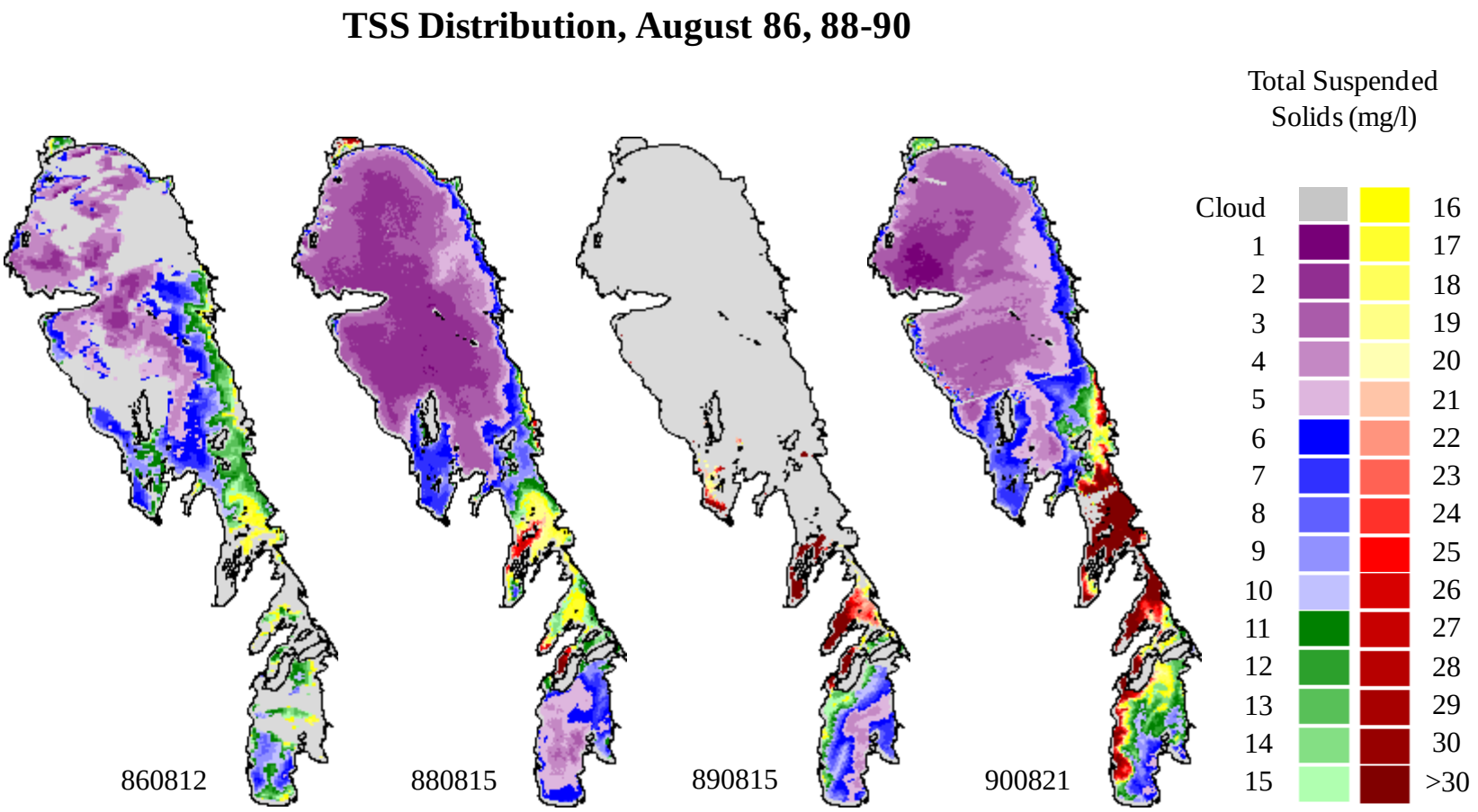

Figure 12. Total suspended solids (TSS) determined from NOAA AVHRR data, August 1986, and 1988-90.

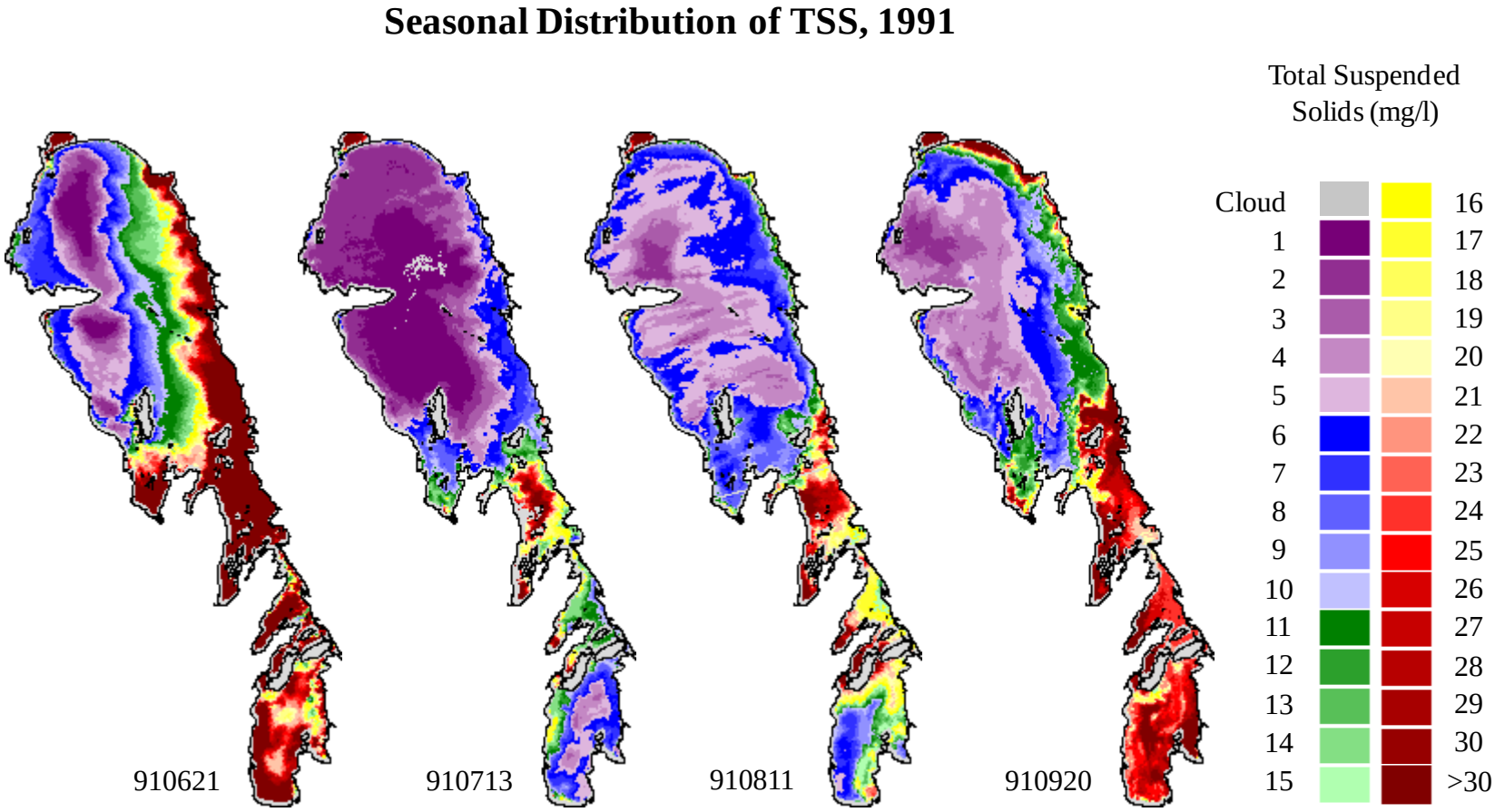

Figure 13. The seasonal distribution of total suspended solids determined from AVHRR data, 1991

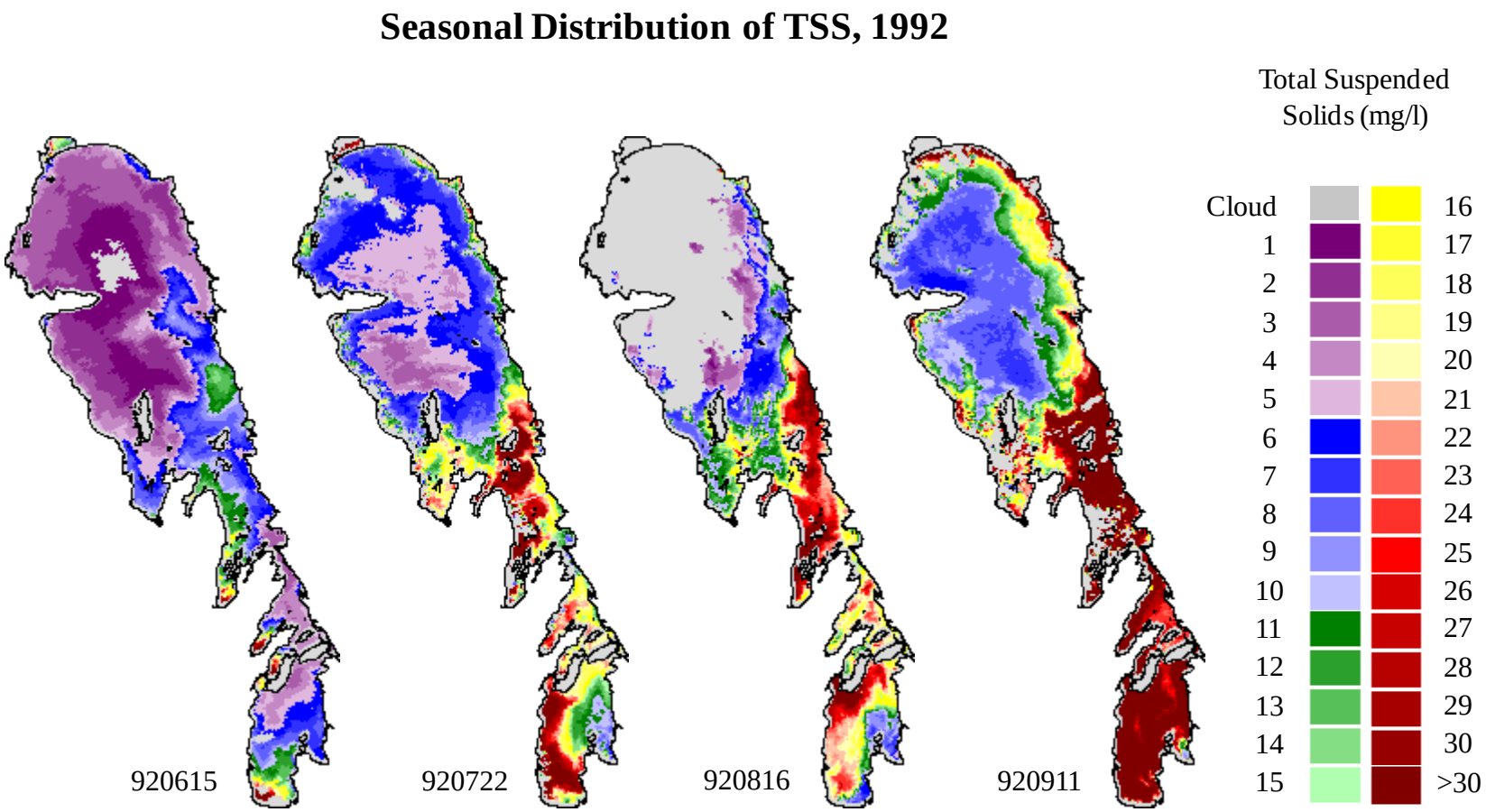

Figure 14. The seasonal distribution of total suspended solids determined from AVHRR data, 1992.

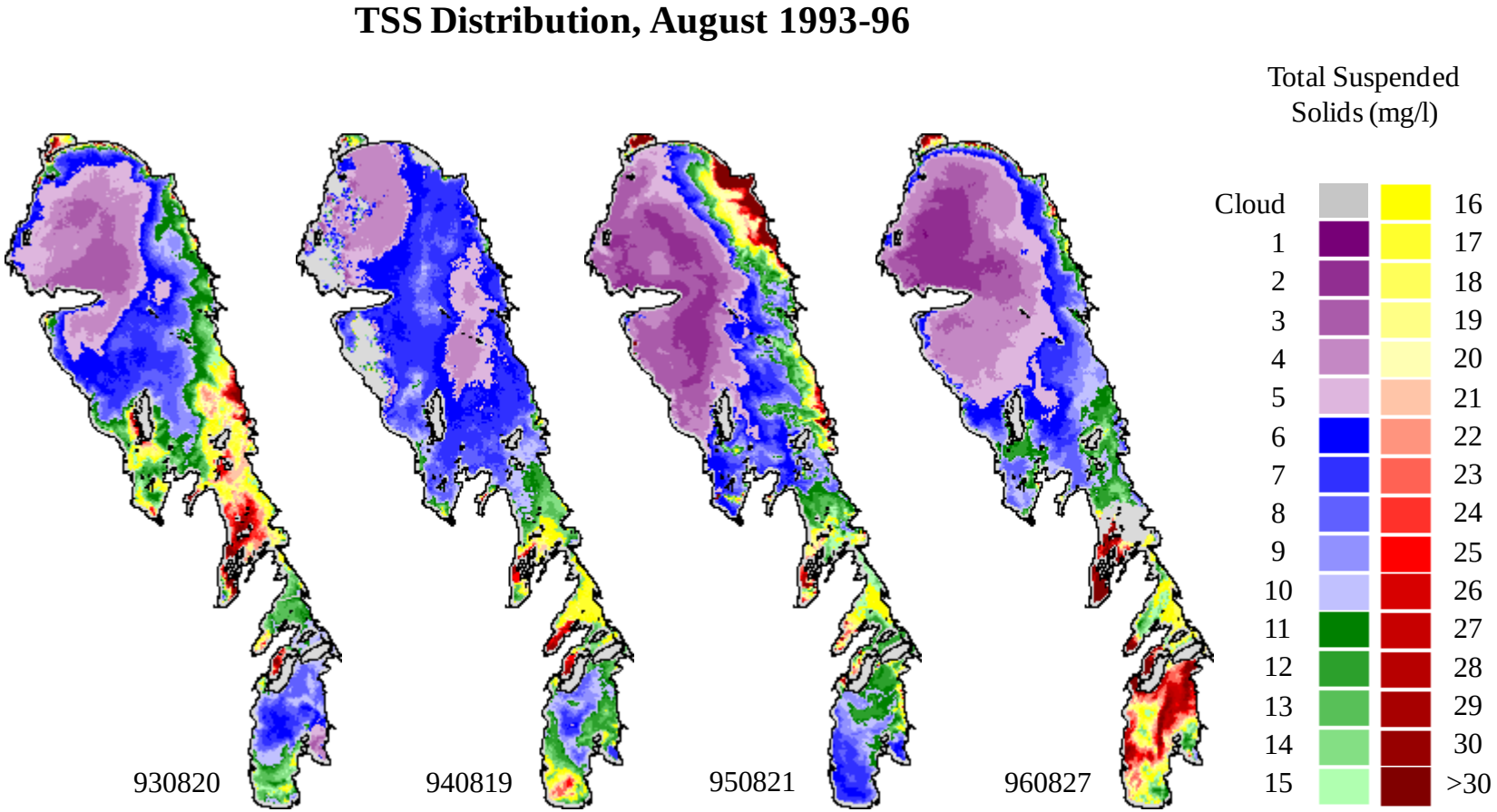

Figure 15. The distribution of total suspended solids determined from AVHRR data, August, 1993-96.

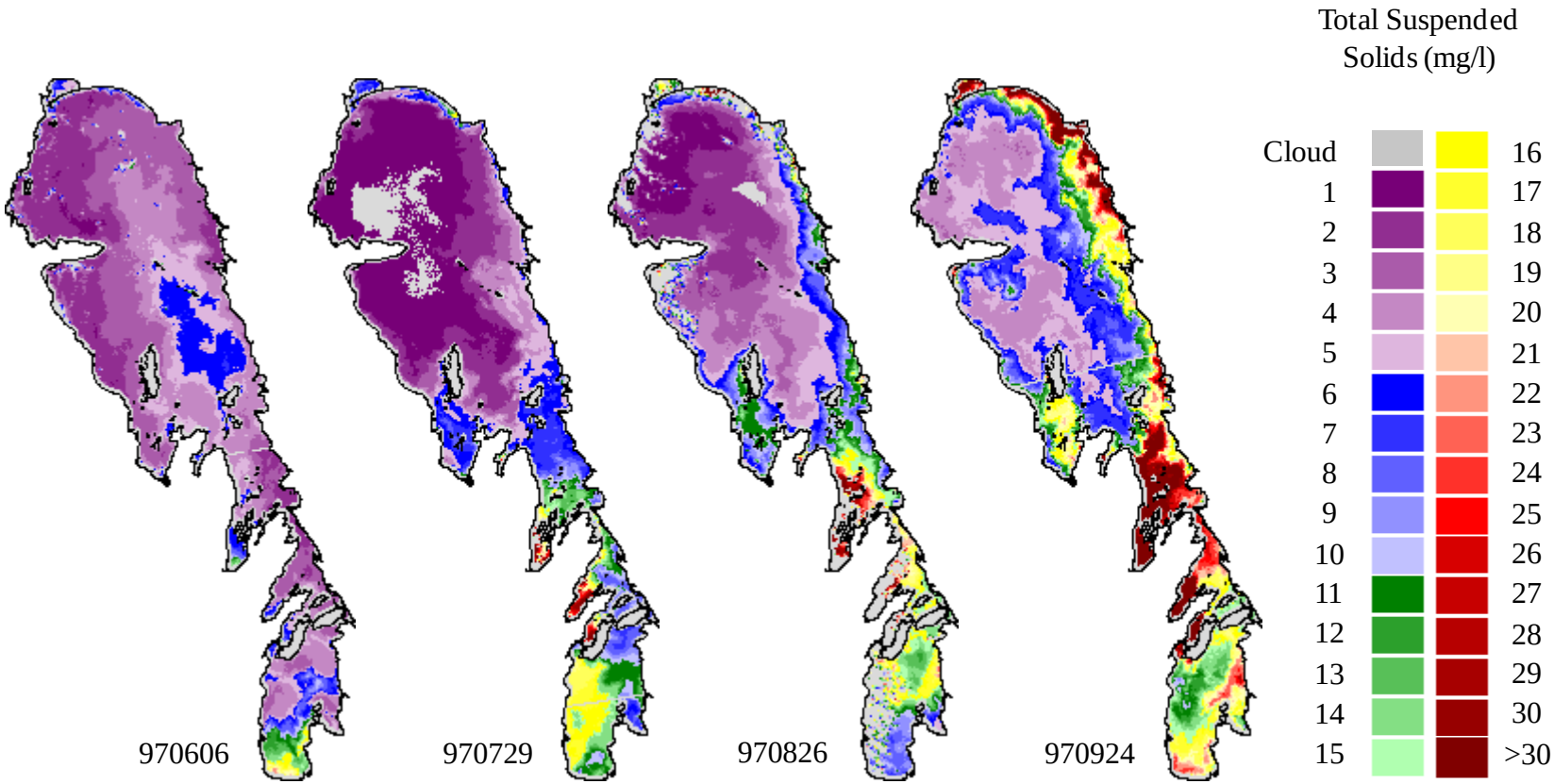

Figure 16. The seasonal distribution of total suspended solids determined from AVHRR data, 1997

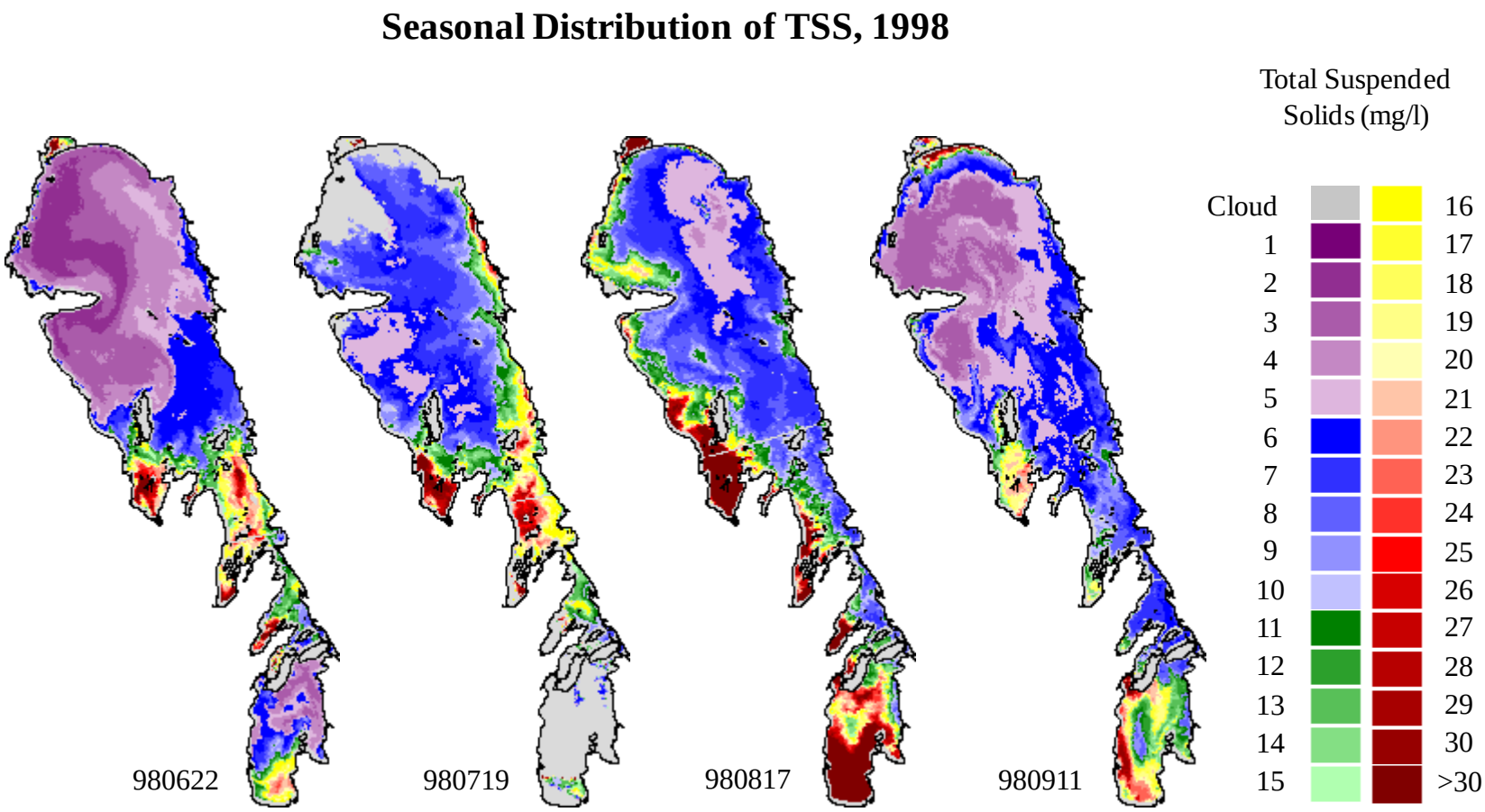

Figure 17. The seasonal distribution of total suspended solids determined from AVHRR data, 1998

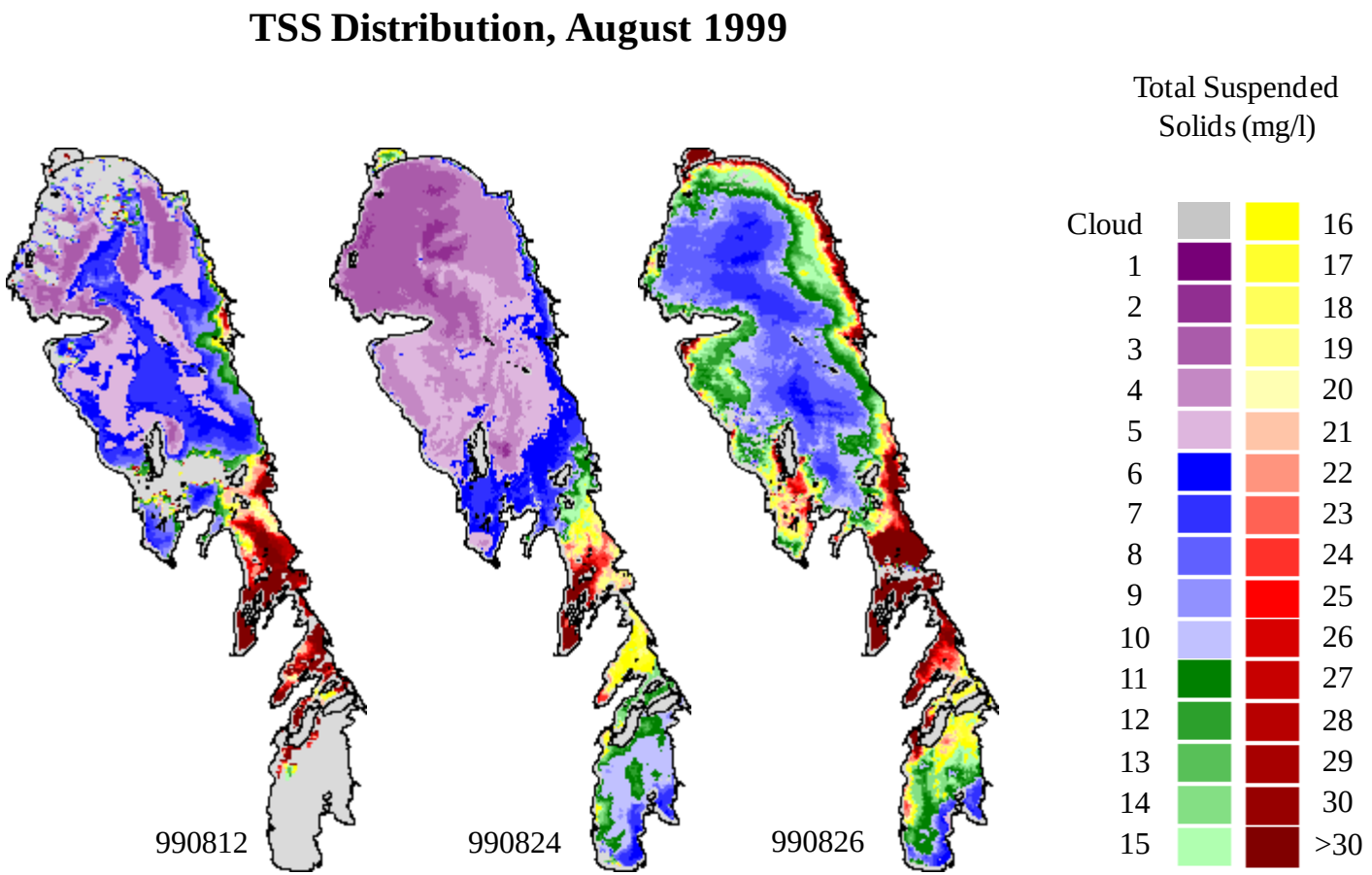

Figure 18. The distribution of total suspended solids determined from AVHRR data, August 1999.

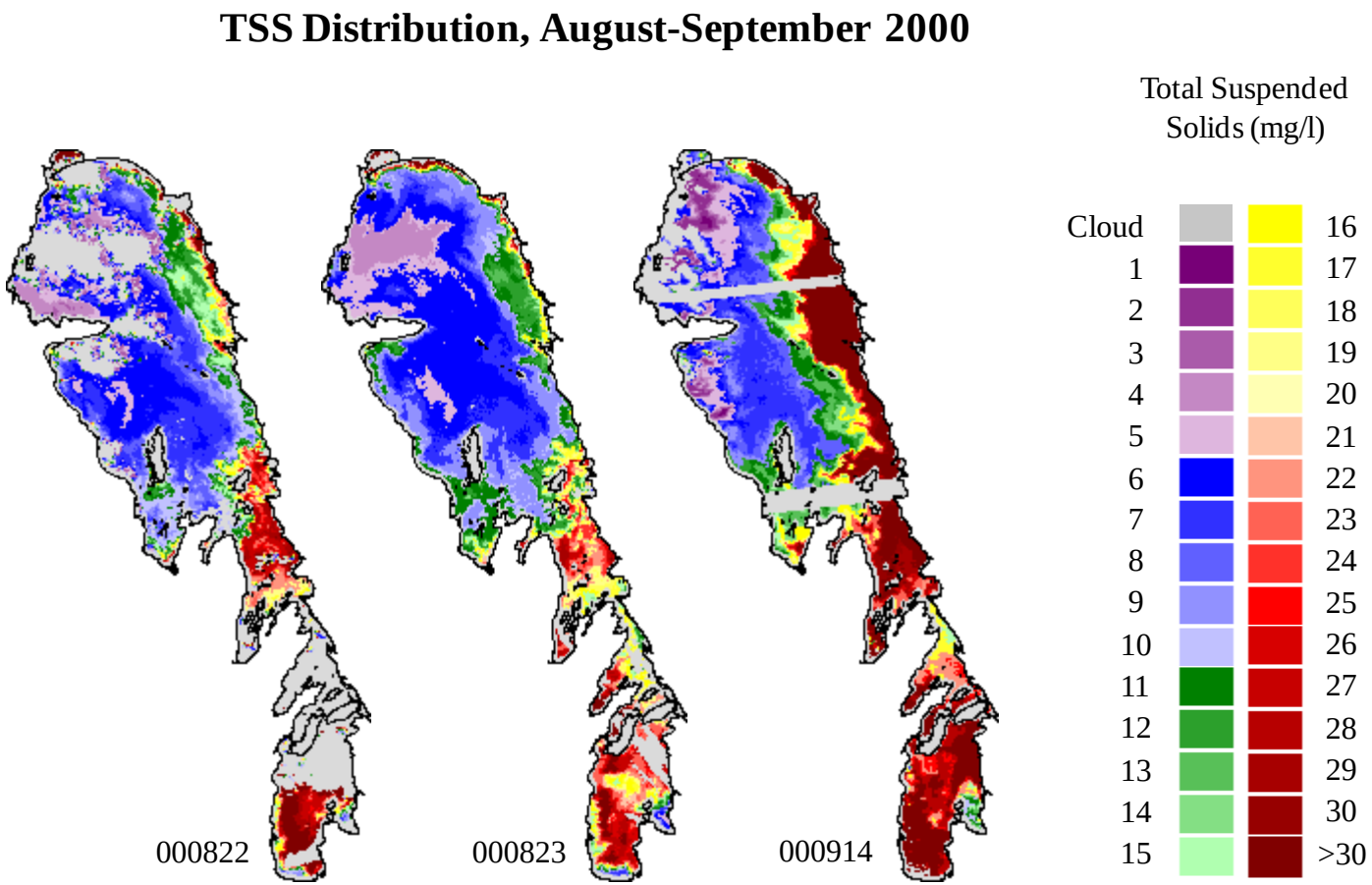

Figure 19. The distribution of total suspended solids determined from AVHRR data, August-September, 2000.

5 ANALYSIS

5.1 Regional and time series analysis

Mean TSS was calculated for regions for the purposes of calculating and graphing the history of regional TSS. Primary regional subdivisions are based on natural physical constrictions, and to some extent on regional patterns in mean TSS. The North Basin was subdivided at 15 km from shore into nearshore ("NR" in Figure 20) and pelagic ("OFF") subregions. All other regions, including nearshore regions, are themselves bounded by a line about 3-4 km from shore to minimize the effect of very localized nearshore plumes on the mean TSS for the region.

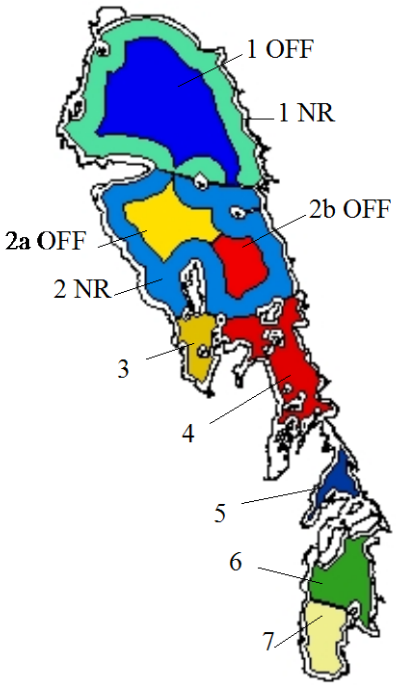

Figure 20. Regions for extraction of descriptive statistics. "OFF"=offshore; "NR"=nearshore. Regions labeled offshore are bounded by a line 15 km from shore. All other regions are bounded by lines 3-4 km from shore.

As would be expected, mean TSS in the northern regions, 1 and 2, is lower than for the southern regions (Table 14) and TSS is lower in the pelagic regions (offshore) than nearshore. Perhaps surprisingly, the standard deviation does not differ much between pelagic and nearshore. However, the nearshore regions each comprise "nearshore" waters on both east and west shores, so that descriptive statistics reflect spatial as much as temporal distributions. At least for these spatially complex nearshore regions, it is more useful to examine the maps of these descriptive statistics illustrated and discussed in below.

TSS in Region 3, Sturgeon Bay, is higher than in the North Basin generally, and similar Region 4 (south of Berens Island) to the east. TSS is generally highest in the Narrows regions (4 and 5), though not significantly higher than in the South Basin. Interesting the mean and maximum TSS in the Narrows regions are almost as high as for Region 7, near the mouth of the Red River.

Table 14. Descriptive statistics by regions for late-July-August TSS data set. (Units: $mg \cdot L^{-1}$)

Region	mean	s.d.	min.	max.	n
1NR	7	3	2	14	19
2NR	8	3	3	12	23
1OFF	5	2	1	9	23
2OFF	6	2	2	10	24
2aOFF	6	3	1	11	23
2bOFF	7	2	3	13	24
1	6	2	2	12	19
2	7	2	3	11	23
3	14	9	6	41	26
4	18	7	8	34	25
5	20	7	11	35	23
6	13	5	6	23	24
7	15	9	5	48	24

Figure 21 shows time series of Late July-August mean TSS by regions of Lake Winnipeg for the period 1985-2000. Figure 22 shows seasonal times series (June-September) of mean TSS by regions of Lake Winnipeg for 1991, 1992, 1997 and 1998.

Although if one ignores the1985 data, the plots for Regions 1, 2, 6 and 7 suggest a small rising trend in TSS (Figure 21) none of the regional mean TSSs show a significant linear time trend. This is true even if the two high values at the beginning of the series (1995) are removed from the set.

Regions 1 and 2 were relatively clear in 1990-1991 and 1995-97, but that pattern is not evident in the more southerly regions. What interannual pattern there is does appear to be supported by multiple within-year, summer samples, i.e. multiple TSS values within a given year tend to shift as a group compared to previous and subsequent years. Obvious exceptions are Region 4, 1991, and Region 1, 1998.

There is not a strong, and certainly not a significant seasonal pattern in the data (Figure 22) unless the June, 1999 data points are excluded. In the 3 other years, TSS tends to be least variable and frequently lowest in June, and in some regions (e.g. Regions 6, 7) is highest and most variable in September, but there are numerous exceptions.

One expects this to be the case in the pelagic zone in the North Basin (Region 1OFF, 2OFF) where TSS is low and comprised mostly of plankton which should typically peak

in August. However, in the South Basin, where TSS is higher and comprised mostly of mineral sediments, we expect high TSS to be related either to higher flows in the Red River (the main source of sediments to the South Basin) or to higher winds driving shore erosion or bottom resuspension. This question is revisited in below, in a discussion of maps of correlation between TSS and time of year..

Regional mean TSS was tested for correlation with several environmental variables (summer air temperature, summer inflows, wind, lake levels). Coefficients of correlations were rarely significant. On the other hand pixel-by-pixel correlations with these variables showed more local areas of correlation. These results are illustrated and discussed in Section 5.3.

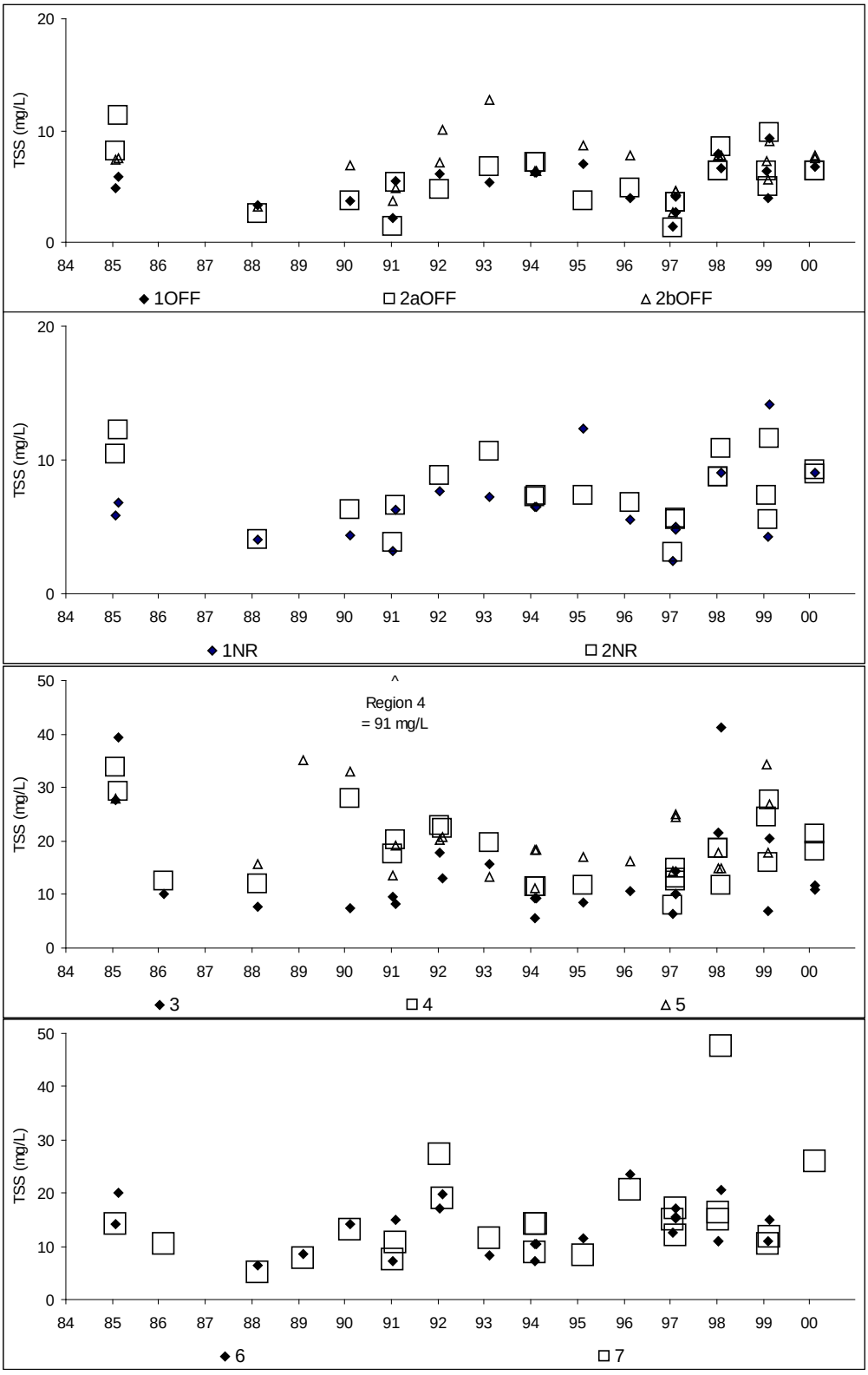

Figure 21. Late July-August mean TSS by regions of Lake Winnipeg for the period 1985-2000. Means are shown only for dates with <15% cloud cover within the region. Note expanded TSS scale for Regions 1 and 2 as compared with Regions 3-7.

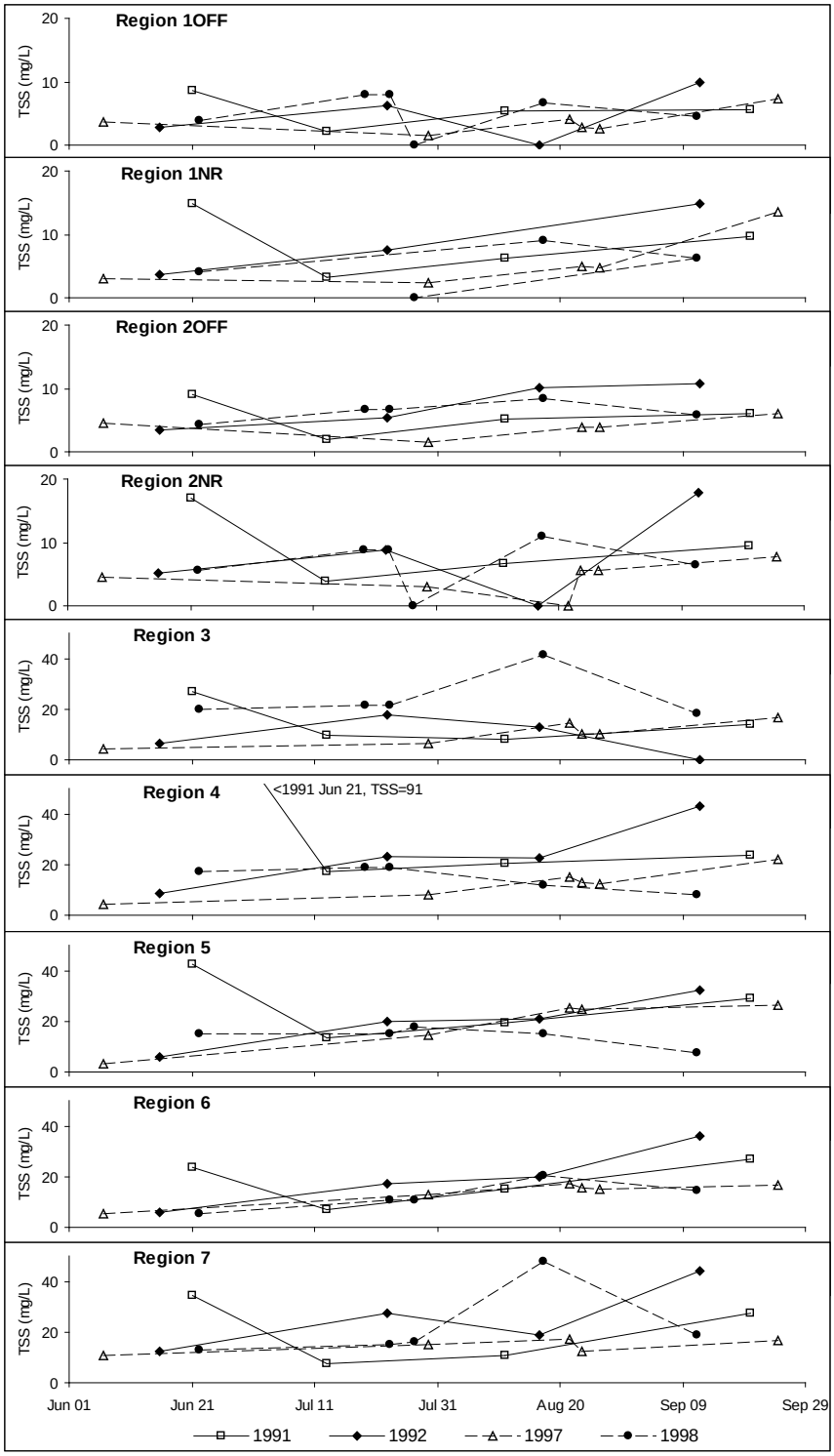

Figure 22. Seasonal times series of mean TSS by regions of Lake Winnipeg for 1991, 1992, 1997 and 1998. 2OFF = mean TSS for Regions 2aOFF and 2bOFF. Means are shown only for dates with <15% cloud cover within the region. Note expanded TSS scale for Regions 1 and 2 as compared with Regions 3-7.

5.2 Maps of descriptive statistics for TSS

Figure 23 shows maps of the minimum, mean and maximum TSS in Lake Winnipeg. Maximum TSS is highest in the bays along the west shore from Sturgeon Bay to the Narrows west of Hecla Island, at the south end of the south basin, near the mouth of the Red River, and at the north end of the lake along the northeast lakeshore (erosion plumes) and in Limestone Bay. As for maximum TSS, the highest mean and highest minimum TSS is in the bays along the west side of the Narrows, and in Limestone Bay. Mean TSS in the South Basin is slightly lower than in these bays, and indeed, lower than in most of the Narrow and Fisher Bay region. Not surprisingly, the lowest maximum, mean and minimum TSS all occur in the pelagic zone of the North Basin, all in the region north of Long Point.

The maximum mid-summer TSS in the South Basin is 83 $mg \cdot L^{-1}$; in Washow Bay, TSS is higher, up to 136 $mg \cdot L^{-1}$. The maximum TSS was calculated in the nearshore plume near Warren's Landing, up to 680 $mg \cdot L^{-1}$, though these values are well-beyond the range of the validation data set, and may be exaggerated by the exponential model. The maximum values in the pelagic regions of the North Basin, Regions 1OFF, 2aOFF and 2bOFF (Figure 23) are 24, 17 and 23 $mg \cdot L^{-1}$, respectively.

Except in the bays along the west shore of the Narrows, and Limestone Bay, minimum TSS is less than about 6-7 $mg \cdot L^{-1}$ in most of the lake. The highest minimum TSS in the whole lake, in Fisher Bay, is 23 $mg \cdot L^{-1}$. In much of the area at the north end of the Narrows and into Fisher Bay, the minimum summer TSS is 10-20 $mg \cdot L^{-1}$. The minimum value over more than half of the North Basin is ≤ 3 $mg \cdot L^{-1}$. However, the absolute minimum value in the late July-August data set is 1.4 $mg \cdot L^{-1}$. This is higher than the expected value, and implies over prediction by the model at very low TSS. Nonetheless, any such over prediction will not affect the order of TSS magnitude predicted, so that the pattern indicating lowest TSS in the region north of Long Point remains valid.

Figure 24 shows two maps describing the variability of TSS in Lake Winnipeg. Both are maps of standard deviation of TSS normalized by dividing it by the mean TSS. Figure 24a was calculated from 12 one-per-year late July-August TSS maps, and Figure 24b was calculated from a larger set of 20 TSS maps including June-September maps. Dark grey tones in the maps indicate pixels with cloud cover in at least one source image, and therefore, pixels for which standard deviation could not be calculated.

Variability is generally lower in the pelagic zone, and higher nearshore. This is most apparent in the North Basin, where the highest normalized standard deviation (n.s.d.) occurs along the eastern shore, the windward shore for prevailing summer winds. Including spring and autumn data (Figure 24b) increases both the magnitude and size of the north-eastern nearshore high n.s.d. zone.

Including spring and autumn data also increases n.s.d. in the area from the Narrows to Berens Island (although some of this area is cloud-covered in Figure 24a). TSS in the Sturgeon Bay-Reindeer Island-Berens Island area is moderately high, although not as high as the eastern shore and the Narrows-Berens Island area.

Unexpectedly, variability in the southern South Basin is higher for the late July-August data set than for the larger June-September set. Variability in the northern South Basin is lower, and about the same magnitude as much of the pelagic North Basin.

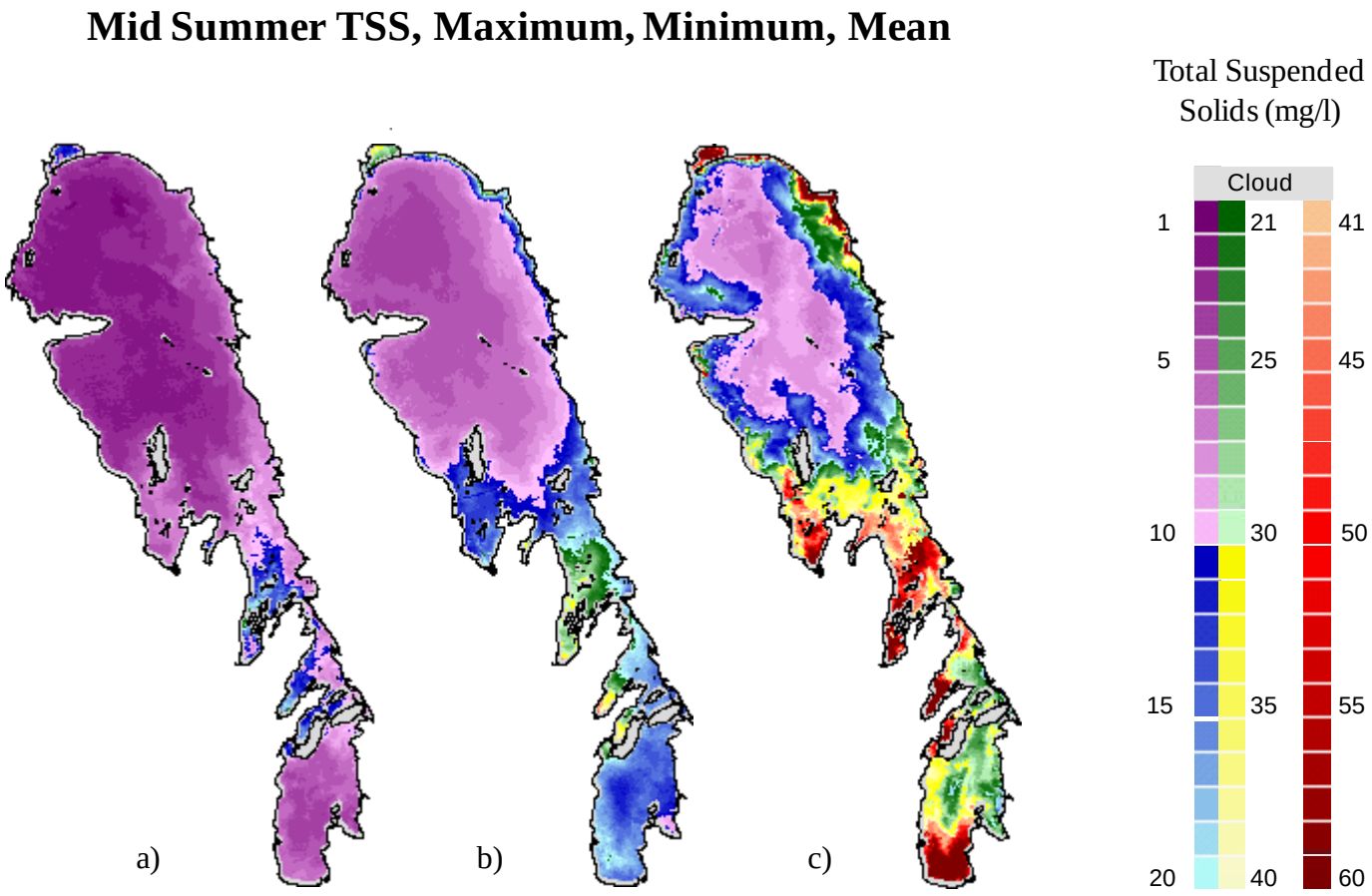

Figure 23.Total suspended solids for late July-August images a) minimum TSS, b) mean TSS, c) maximum TSS, 1985-2000

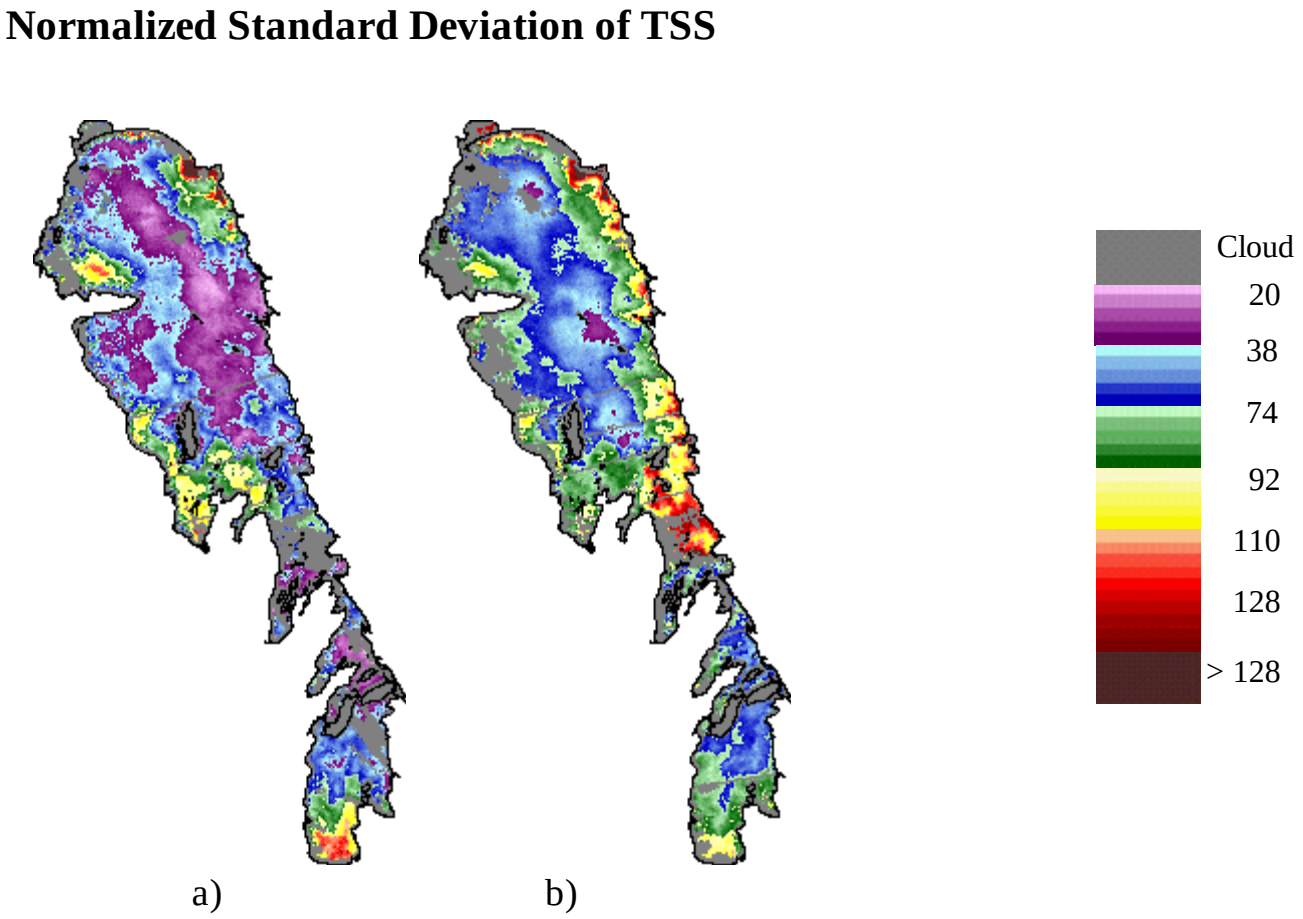

Figure 24. a) Standard deviation of TSS normalized by mean TSS (100*s.d /mean), 12 images late July-August. b) standard deviation of TSS normalized by mean TSS (100*s.d /mean), 20 images late July-August.

5.3 Environmental effects on TSS

Figures 26 to 30 are maps of the coefficient of correlation (r) between TSS and several environmental variables which might be expected to have some influence on TSS in Lake Winnipeg. All coefficients mapped are for correlation between untransformed variables.

Correlations could only be determined on regions of the lake which are clear of cloud-cover on all images. Hence, subsets of the TSS maps shown in Figures 11 to 19 were used. Where variables might be associated with individual scenes, regardless of season (e.g. Julian day, wind, lake level) we analyzed a set of 20 relatively cloud-free TSS maps acquired from 1985-1999, and representing all months from June to September. To investigate inter-annual variability (associated with, e.g. river inflow) we were limited to 12 TSS maps, again from 1985-1999, and all acquired between late July and the end of August. In the case of summer temperature, we were further limited by lack of post-1997 data to 10 TSS maps.

Negative r (inverse relationship) is indicated by purples, blues and greens, and positive r by yellows, oranges, reds and browns (see legends accompanying Figures 26 to 30). Values of r associated with regression slopes significant at 95% and 99% confidence are shown in Table 15. For instance, for n=20, if r>=0.45 then we have 95% confidence that slope of the relationship between two variables is significant. Thus for n=20, purple (inverse correlation) and red and brown (positive) indicates regions of significant correlation at >=95% confidence.

Table 15. Minimum absolute values of r for which the slope of a relationship is significant at 99% and 95% confidence. n = number of paired observations in sample.

	P-value (Confidence)	
n	**0.01 (99%)**	**0.05 (95%)**
10	0.76	0.63
12	0.71	0.58
20	0.57	0.45

Interannual factors (temperature, spring and summer inflow) are discussed first. Although regions of significant correlations are described, it is important to note that the sample size (10 to 12) is very small, and some apparent correlations may be spurious. Inferences are particularly weak in regions of low TSS variability (Figure 24).

The effect of wind and lake level is discussed after. Because these parameters operate on a scale of days, rather than years, the sample size can be somewhat larger (n=20) and greater confidence can be placed in positive results.

5.3.1 Julian Day

Twenty TSS maps were used to investigate correlation between TSS and Julian day (figure 26a). Julian days in the sample ranged from 159 (6 June) to 269 (24 Sept.). Positive correlation would indicate an increasing trend in TSS through the open water season. With n=20, correlation is significant (95% confidence) at r>+/-0.45 and highly significant (99%) at r>+/-0.57. Reds and browns indicate significant positive correlation. Correlation (r) is significant for only small areas at the extreme north end of the North Basin, south of Long Point and parts of the north-eastern third of the South Basin. In only a very few of these pixels is r highly significant.

At least where TSS concentration is mainly a function of erosion, one might think that this is due to stronger or more northerly winds in late summer and autumn as compared with early in the open water season on Lake Winnipeg. However, at least in this data set, stronger winds are not likely the main cause of higher late season TSS. In the North Basin, the regions of highest r are coincident with low mean and maximum TSS (Figure 23). The TSS in these regions would have been predominantly plankton, and therefore a function of productivity, not erosion. Moreover, the regions of highest correlation between TSS and Julian day are not strongly coincident with regions of strongest correlation between TSS and wind (compare Figure 28 and 29). In fact, although the wind data used in this study does appear to be slightly higher in August and September as compared with June (Figure 25) neither mean or maximum winds for the two day periods antecedent to each AVHRR image are significantly correlated with Julian day.

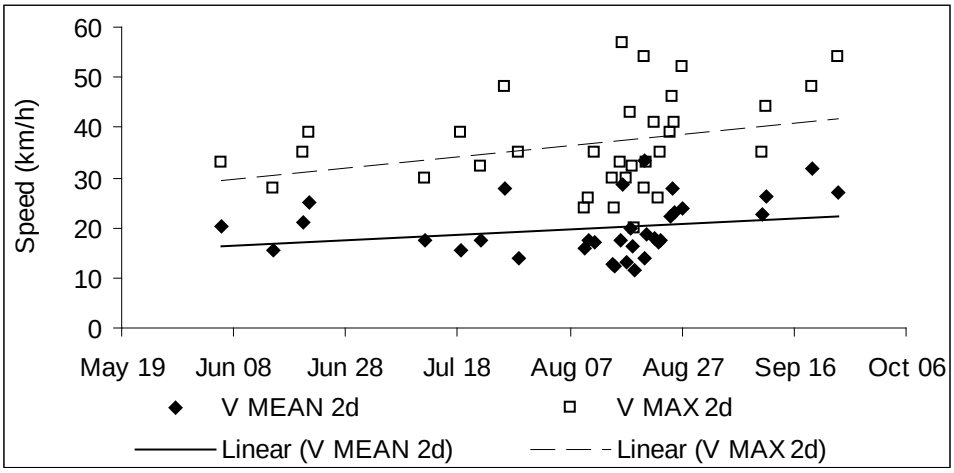

Figure 25. Seasonal pattern in wind speeds at Georges Island, for the days of the AVHRR images used in this study (means and maxima for 2 d antecedent periods). Neither trend line is significant at 95% confidence.

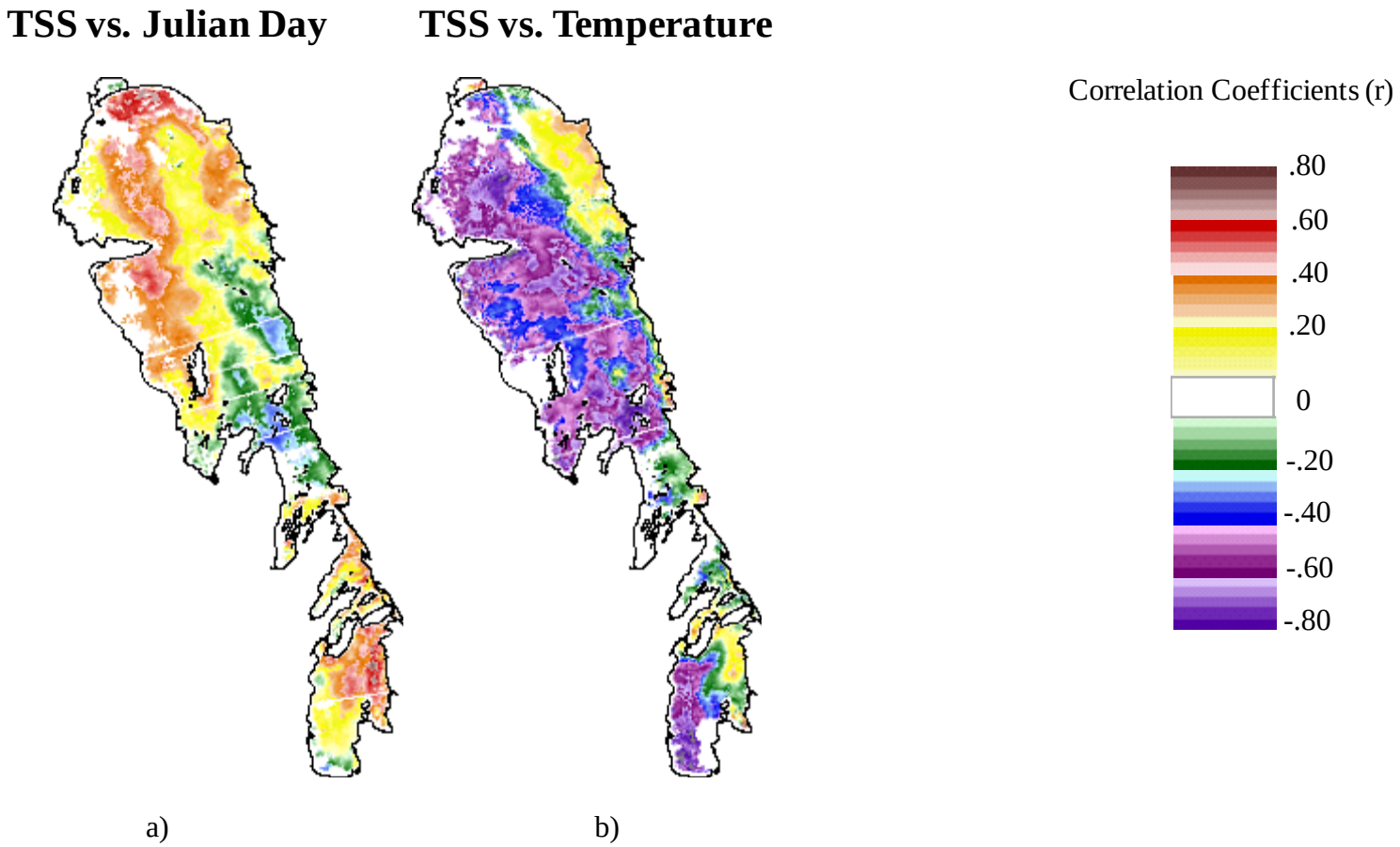

Figure 26. a) Correlation (r) between TSS and Julian day for 20 AVHRR-derived TSS maps (1985-1999) each with <2% cloud-cover, and b) between TSS and mean May-August air temperature at Grand Rapids, Berens River and Beausejour for 10 images (1985-1997, late July-August images).

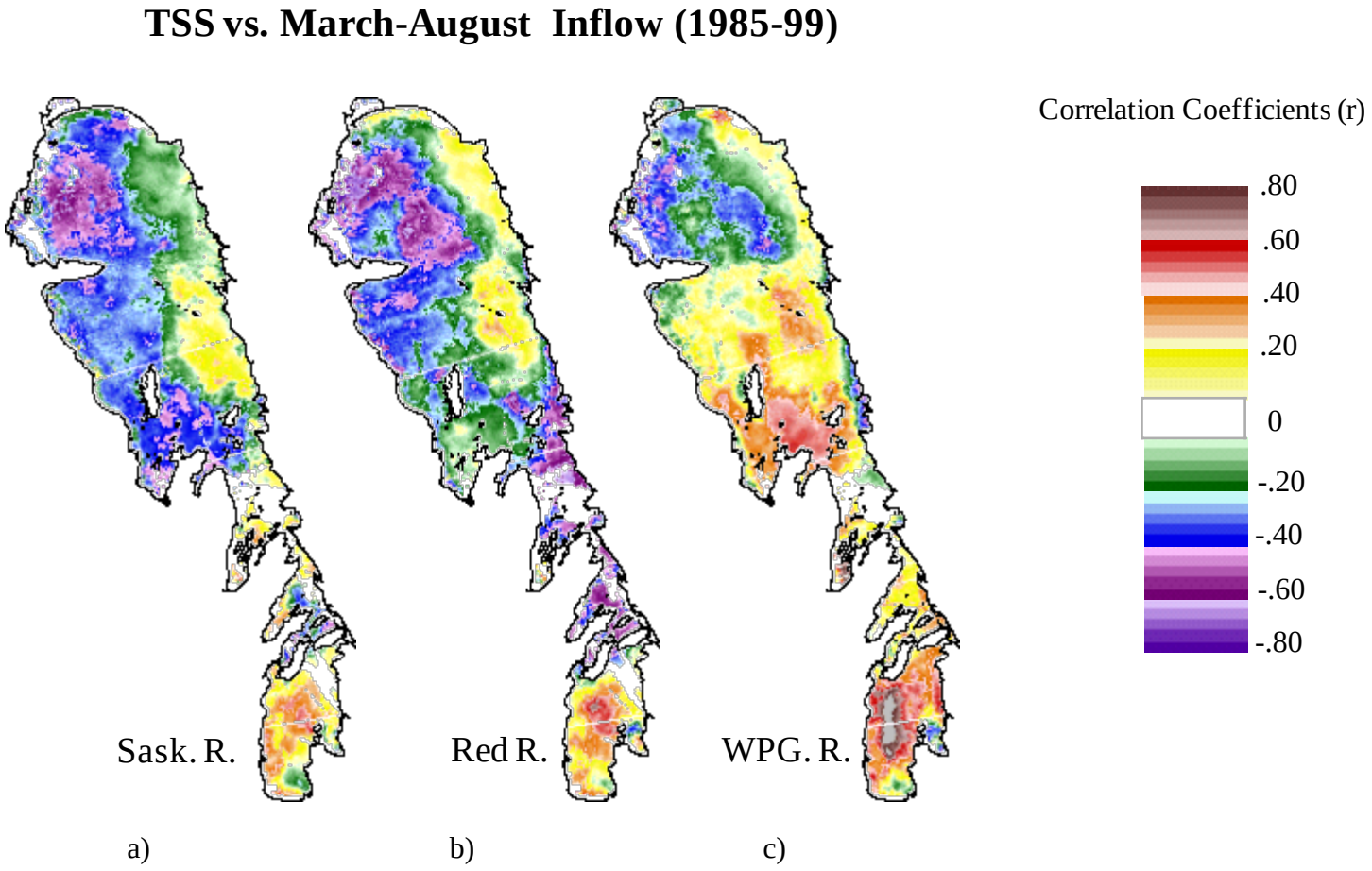

Figure 27. Correlation (r) between TSS and March-August inflow for 12 AVHRR-derived TSS maps (1985-1999, late July-August images) each with <2% cloud-cover: a) Saskatchewan R. March-August flow, b) Red R. March-August flow, c) Winnipeg R. March-August flow.

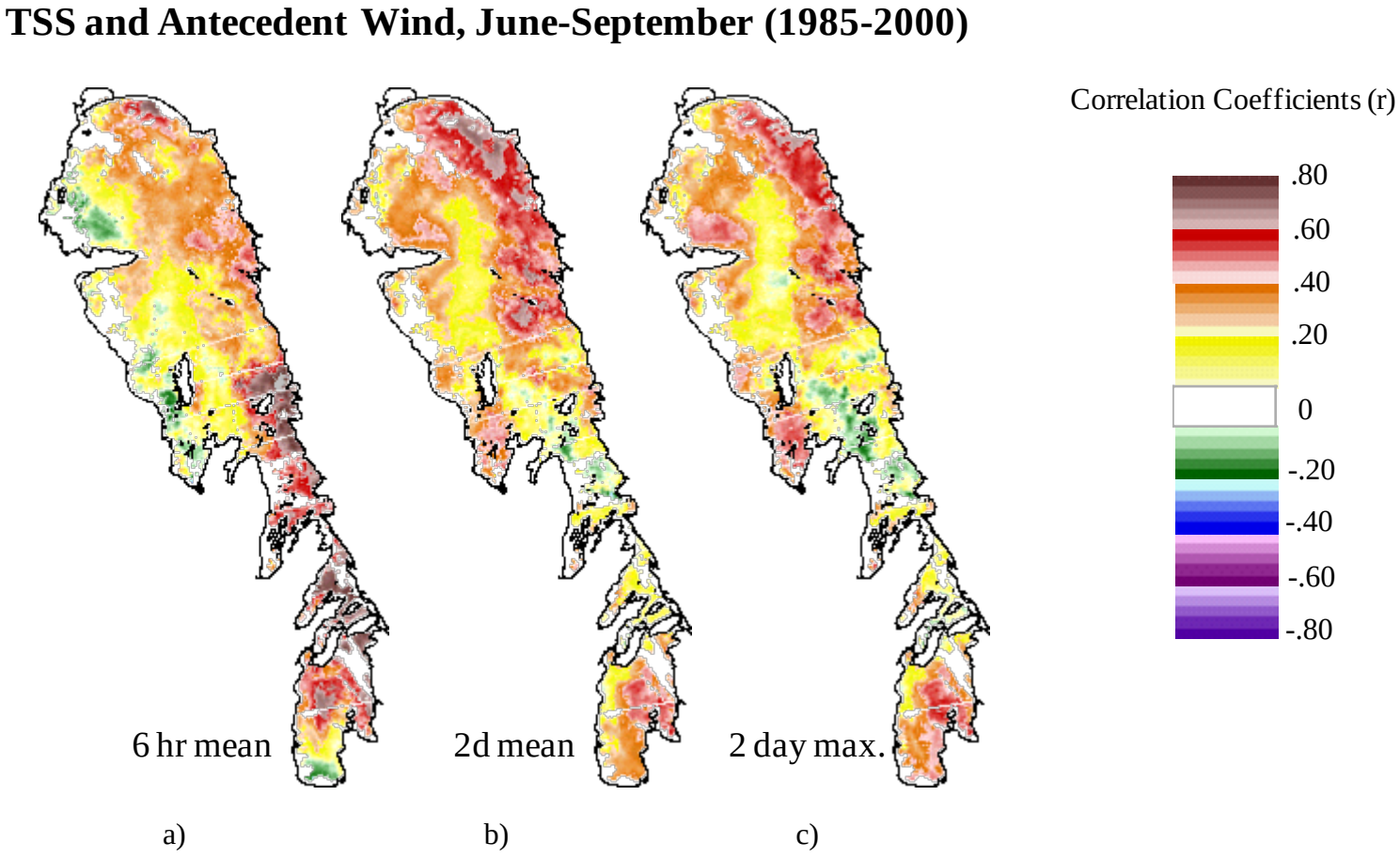

Figure 28. Correlation (r) between TSS and antecedent wind for 20 AVHRR-derived TSS maps (1985-2000, June-September images) each with <2% cloud-cover. a) 6 h mean wind, b) 2 d mean wind, c) 2 d maximum wind.

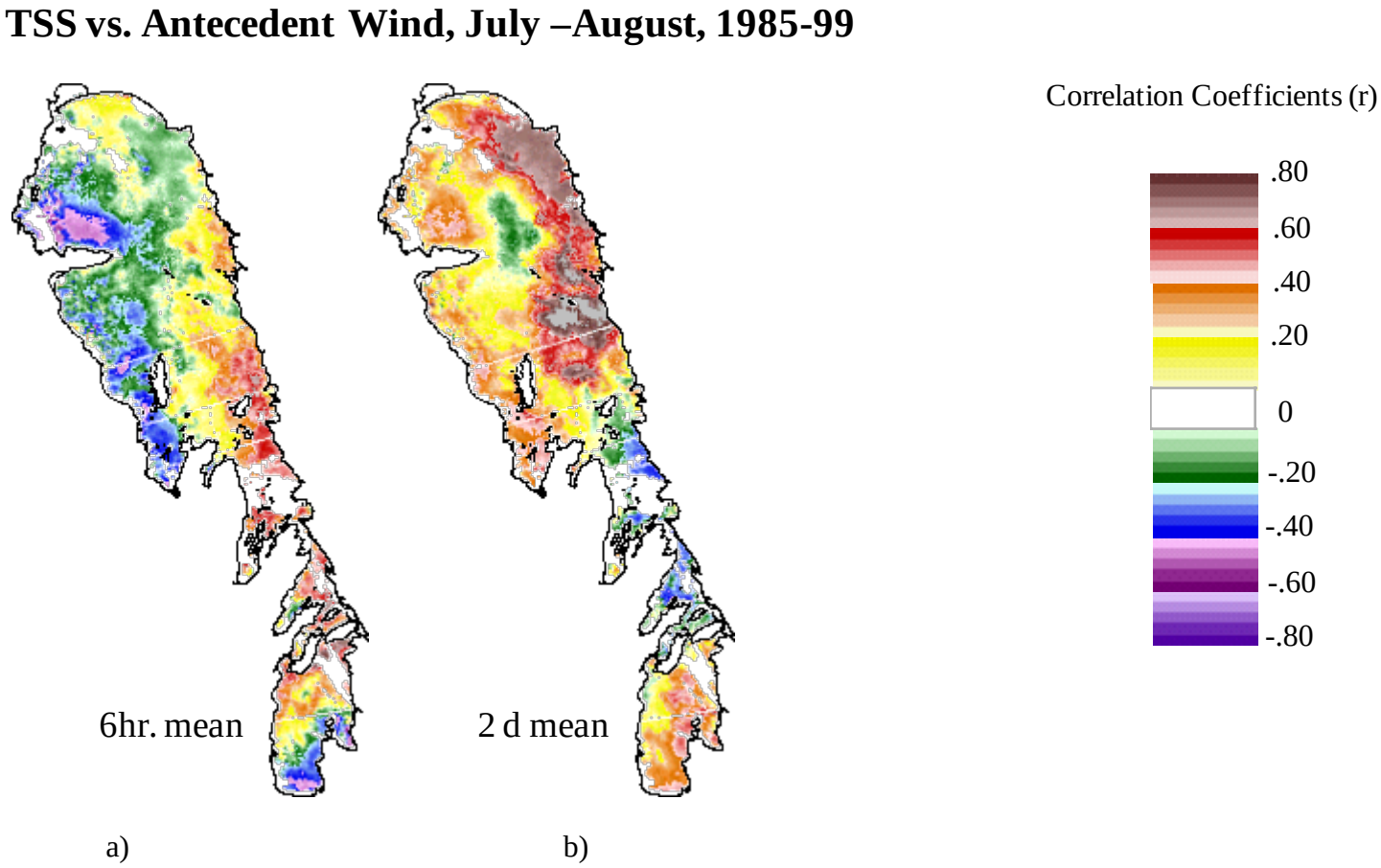

Figure 29. Correlation (r) between TSS and antecedent wind for 12 AVHRR-derived TSS maps (1985-1999, late July-August images) each with <2% cloud-cover: a) 6 h mean wind, b) 2 d mean wind

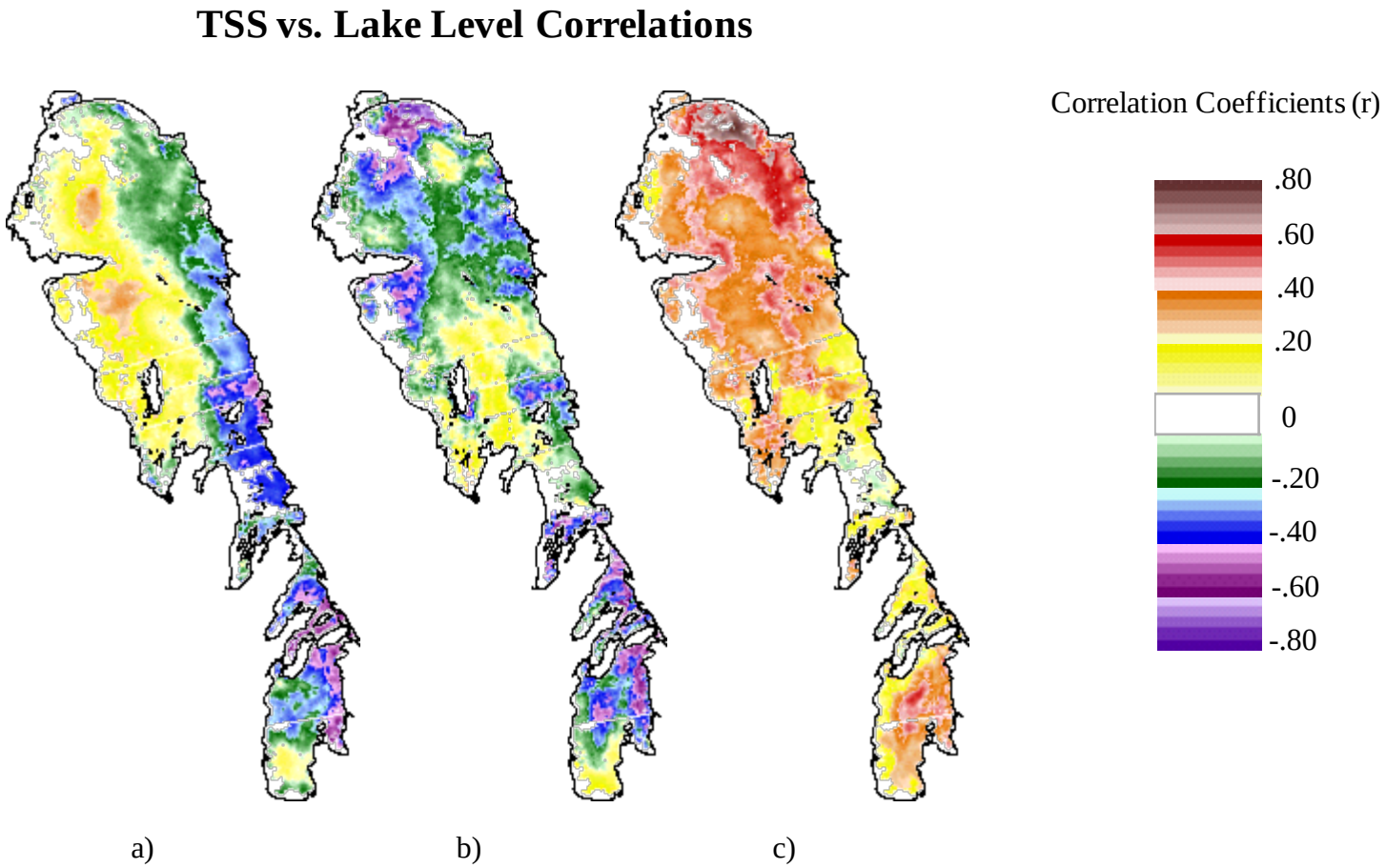

Figure 30. Correlation (r) between TSS and lake level, and TSS and measures of the difference between South and North Basin levels for 20 AVHRR-derived TSS maps (1985-1999)

5.3.2 Summer temperature

May-August mean temperatures for the period of this study at Grand Rapids, Berens River and Beausejour are shown in Figure 31, below. The mean of the 3 stations was used in calculating maps of correlation between TSS and summer temperature.

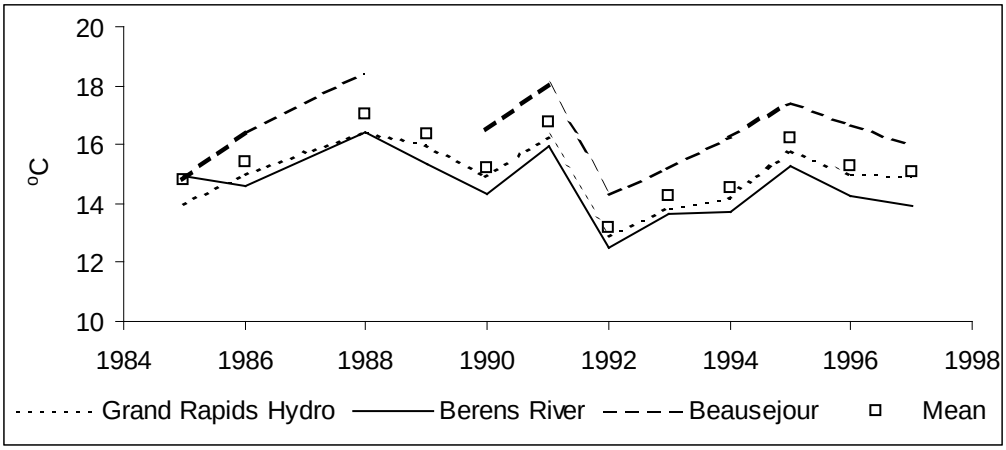

Figure 31. May-August mean temperature at Grand Rapids (Manitoba Hydro station) Berens River and Beausejour (Atmospheric Environment Service stations). Mean value for 1989 was calculated by including an estimation Beausejour temperature by regression with paired Grand Rapids data (r^2=0.93, n=11).

.

We tested correlations of spring-summer temperature with only late July-August TSS data (Figure 26b). With n=10, correlation is significant (95% confidence) at r>+/-0.63 and highly significant (99%) at r>+/-0.76. Regions coloured purple indicate significant negative correlation of late July-August TSS with summer air temperature. Thus there is a patchy indication of negative correlation throughout the central and eastern North Basin, and in the southern half of the South Basin. The former is a region of predominantly low TSS (Figure 23b – 4<TSS<10 mean summer values) and the latter moderately high (10<TSS<20 mean summer values).

There is no evidence of positive correlation between summer TSS and temperature. May-August temperature is here used as a surrogate for midsummer water temperature, or possibly growing degree days in the water. It was included in this analysis because it had been thought that productivity in the water column would be positively correlated with summer water temperature. If so, then plankton contribution to TSS would be higher in warmer summers. At least in the eastern and northern North Basin, where TSS is low and dominated by plankton, this implies a positive correlation between TSS and summer temperature. However, this data set does not lend any support to that hypothesis.

5.3.3 Spring and summer inflow

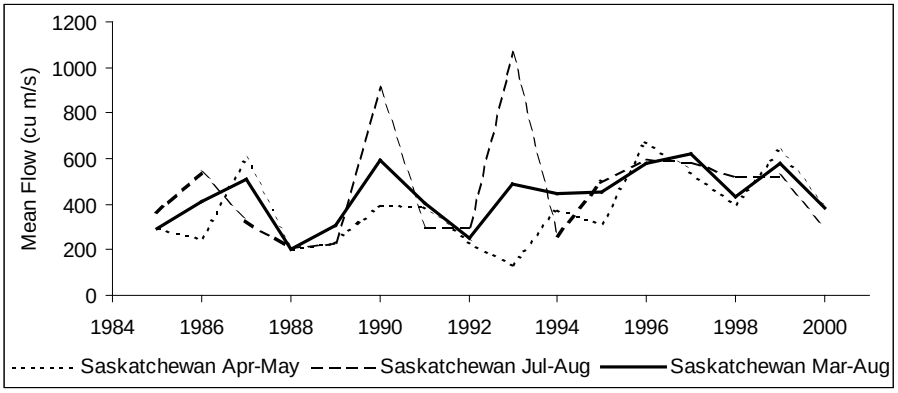

Figure 32. Saskatchewan River flow at Grand Rapids averaged for the periods March-April, July-August and March-August, 1985-2000.

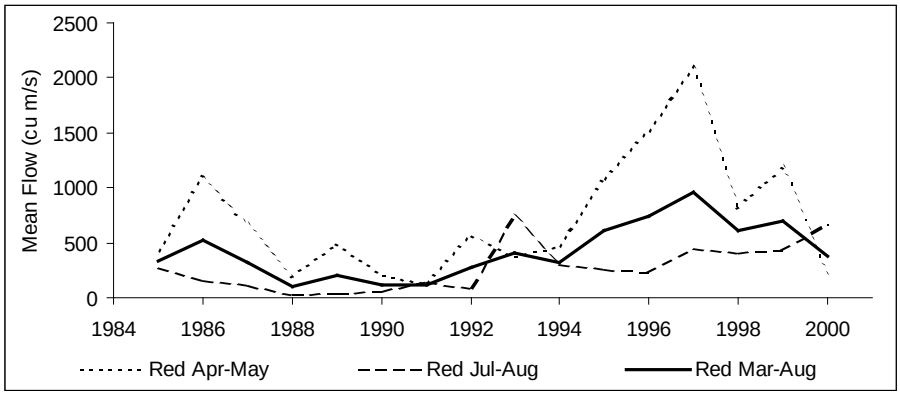

Figure 33. Red River flow at Lockport averaged for the periods March-April, July-August and March-August, 1985-2000. Flows for the year 2000 are estimated from Red R. at Emerson and Assiniboine R. at Headingley records.

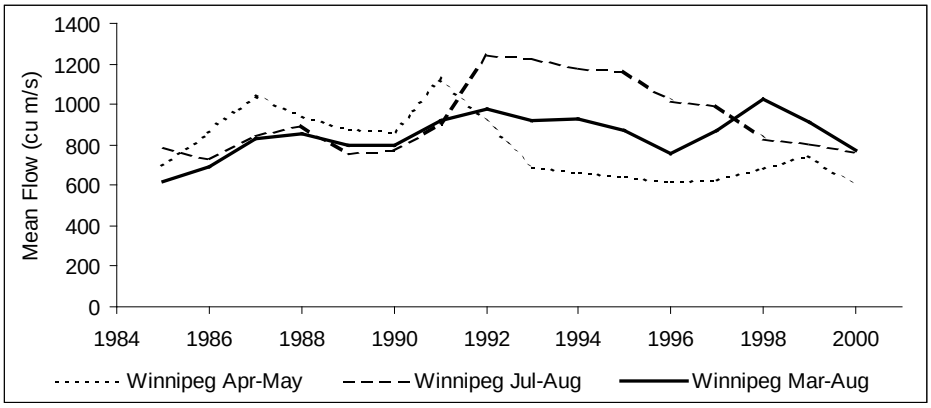

Figure 34. Winnipeg River flow at Pine Falls averaged for the periods March-April, July-August and March-August, 1985-2000.

Major tributary inflow averaged for the periods March-April, July-August and March-August, 1985-2000, is shown in Figure 32-34. Although preliminary tests of correlation with March-April and July-August mean inflow, only correlation between TSS and March-August is discussed below.

Twelve late July-August TSS maps were tested for correlation between TSS and summer inflow (Figure 27). With n=12, correlation is significant (95% confidence) at r>+/-0.58 and highly significant (99%) at r>+/-0.71.

Late July-August TSS is highly, positively correlated with Winnipeg River mean March-August flow at least in the centre-west portion of the South Basin, and significantly correlated over a large part of that basin. In the South Basin there is only weak evidence of correlation with Red River March-August flow.

Surprisingly, there is a region of significant negative correlation of TSS with Red River flow north of Long Point. TSS in the same region is also significantly correlated with Saskatchewan River flow. It seems likely that Saskatchewan River water is responsible for both negative correlations in this region near its mouth. The apparent correlation with Red River flow is probably an artifact resulting from the correlation between the summer discharges in the two rivers (r=0.60, Prob.=0.014, n=16).

Flows lagged one year were also tested for correlation with TSS to determine whether nutrient loading might affect turbidity in the following year. Assuming that nutrient loading is proportional to flow, this might be the case at least in the low TSS regions in the North Basin where TSS is comprised mostly of plankton, if nutrient loading is However, there are few significant positive correlations associated with lagged inflow, and none in the North Basin.

5.3.4 Wind

Mean wind speed and direction for 6 h and 2 d periods antecedent to AVHRR overpass times are listed in Table 12. Correlations between TSS and antecedent wind speed were mapped using both the 20-image June-September set of TSS maps, and the smaller 12-image late July-August set (Figure 28 and 29).

With n=20 (Figure 28) brown indicates highly significant positive correlation (r>0.57), and medium-dark red indicates significant positive correlation (r>=0.45). With n=12 only brown indicates significant correlation.

Over most of the western half of the northern two-thirds of the North Basin, TSS is positively correlated with the mean wind over a 2 d period prior to the AVHRR overpass. In a smaller region in the South Basin, around Elk Island, r is also significant. The pattern of r is much the same whether the mean, maximum or 3rd quartile of the antecedent 2 d wind is used (only the correlations with the mean are illustrated).

Although there are also large regions in which TSS is significantly correlated with the 6 h antecedent wind, the pattern is very different. In the northern region, r remains significant only in very small areas along the north shore, and in the shallow region near Poplar Point, However, in contrast to the pattern for 2 d winds, correlation between TSS and 6 h winds is significant from south of Hecla Island, through the Narrows and up to the north of Berens Island. In much of this region, the correlation is highly significant.

In these analyses, the winds are averaged without regard to direction. However, for the sample of winds antecedent to the AVHRR images, hourly wind directions are broadly distributed (Figure 35). Binned at 30^{o} intervals, in the 2 d sample winds are almost equally distributed between northerly (47%) and southerly (53%), as well as between easterly (44%) and westerly (56%). The 6 h winds are slightly more frequently southerly and westerly.

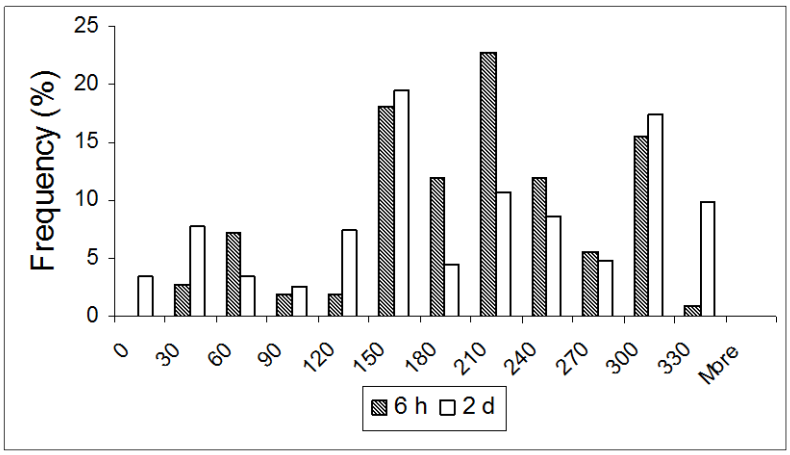

Figure 35. Frequency of hourly wind directions antecedent to AVHRR overpasses in the sample used to create correlation coefficient maps. 6 h = mid-day period antecedent to images. 2 d = 2 day antecedent period.

5.3.5 Lake level

Lake levels recorded at Berens River and Gimli are shown in Figure 36 and listed in Table 13. Twenty TSS maps were used to investigate correlation between TSS and Julian day. Julian days in the sample ranged from 159 (6 June) to 269 (24 Sept.). Positive correlation would indicate an increasing trend in TSS through the open water season. With n=20, correlation is significant (95% confidence) at r>+/-0.45 and highly significant (99%) at r>+/-0.57.

There is little significant correlation between TSS and lake level, except for a small area of inverse correlation along the northeastern shore of the South Basin. Likewise, there is little correlation between TSS and the difference in level of the North and South Basins as recorded at Berens River and Gimli,

The absolute value of the difference in level of the North and South Basins is, however, correlated with TSS in several areas in the lake and the pattern of significant correlation is very much like the pattern for correlation between TSS and mean 2 d antecedent wind. This is expected, because large difference in levels between the basins is due to setup caused by sustained strong winds. It is also associated with fast currents in the Narrows, though there is no evidence (in the form of a correlation with TSS) of increased turbidity being associated with these strong currents.

The 2 d mean wind speed at Georges Island is correlated with the absolute value of the difference in lake level between Gimli and Berens River (r-0.72, P=0.000, n=30). The difference in lake level might actually be a better indicator of sustained high winds than any simple statistic (such as the antecedent 2 d mean speed) in identifying lake wide high wind events.

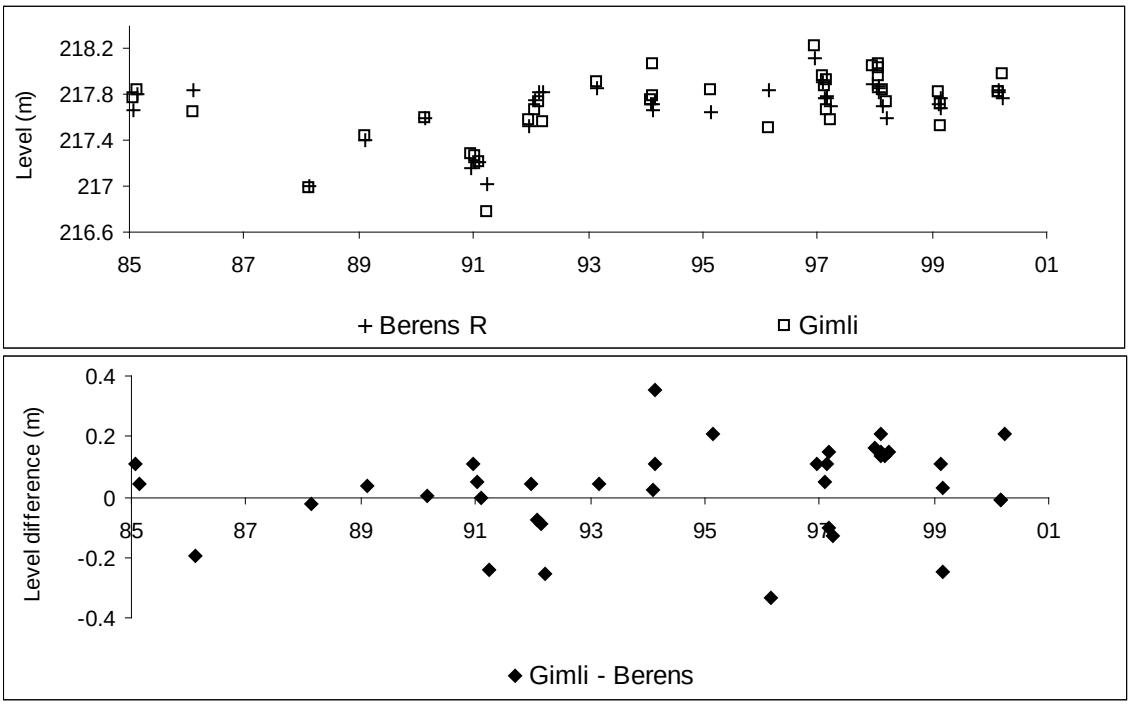

Figure 36. Lake level at Berens River and at Gimli, and the difference in levels between the two stations.

5.4 Comparison of NDVI data with chlorophyll

As described above, chlorophyll fluorescence was measured using a continuous flow Turner fluorometer on August 1999 and 2000 cruises. At the time of writing we are still unable to unequivocally calibrate the fluorometer with the chlorophyll sample data available. In the discussion below, we limit ourselves to investigating the relationship between AVHRR-derived normalized difference vegetation index (NDVI) and chlorophyll fluorescence, as opposed to chlorophyll itself.

Although a good quality AVHRR image was obtained coincident with one day of the 1999 cruise, unfortunately for most of that day, 12th"August, the fluorescence was running at or above the fluorometer range, and little useful data was recorded. There is some rough correlation between fluorescence and AVHRR-derived NDVI for the transect of the following day, the 13th, but as is made apparent below, more nearly simultaneous measurements of albedo and chlorophyll concentration will be required to adequately validate the relationship. In the analysis below, we use only data from the 23-25 August 2000 cruise.

We compared NDVI maps calculated from the 23 August 2000 image with chlorophyll fluorescence (voltage) recorded continuously on the cruise. Figure 37 shows the cruise path superimposed on the NDVI map.

Figure 38 is a time series plot of NDVI and chlorophyll fluorescence along the transect. Apparent gaps in the NDVI time series (e.g.13:00 and 16:00 on the 23rd) occur because the fluorometer operated continuously during station sampling stops where of course only one AVHRR pixel was sampled at the sample location. The NDVI peak at 12:00-14:00, 23 August in Figure 38 appears as a yellow patch north of Reindeer Island in Figure 37. The peaks between 12:00-15:00, on the 24th are east and southeast of Berens Island, where they appear as yellow and green patches.

The fluorescence peak on the 24th is displaced about 2 h (almost 20 km to the north) from the peak NDVI. This gives some indication of the dynamic nature of the algal blooms that cause these fluorescence peaks, and of the need for simultaneous measurements if good cross-calibration of these instruments is to be achieved.

The data from the 23rd is the most nearly simultaneous of the data set. The AVHRR overpass occurred at 14:28, about half an hour after the ship passed through a high region of high chlorophyll fluorescence. The shift from high to low NDVI at 14:00 is coincident with a sharp drop in fluorescence. Both NDVI and fluorescence peak to the left of that drop, although the NDVI peak is almost twice as broad as the fluorescence peak. Data to the left is higher and more variable than to the right for both NDVI and fluorescence.

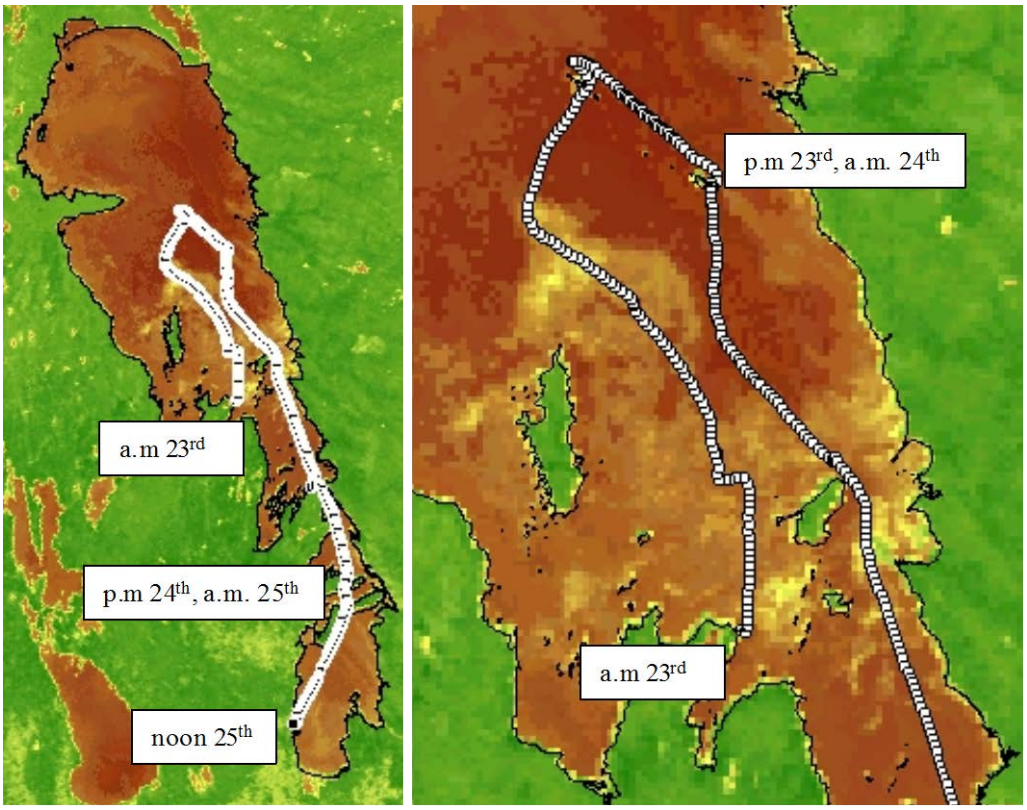

Figure 37. Path of 23-25 August 2000 cruise superimposed on an NDVI map calculated from a 23 August 2000 AVHRR image. The progression brown through yellow to green indicates low through medium to high NDVI.. Dates identify the start and end point of each daily transect.

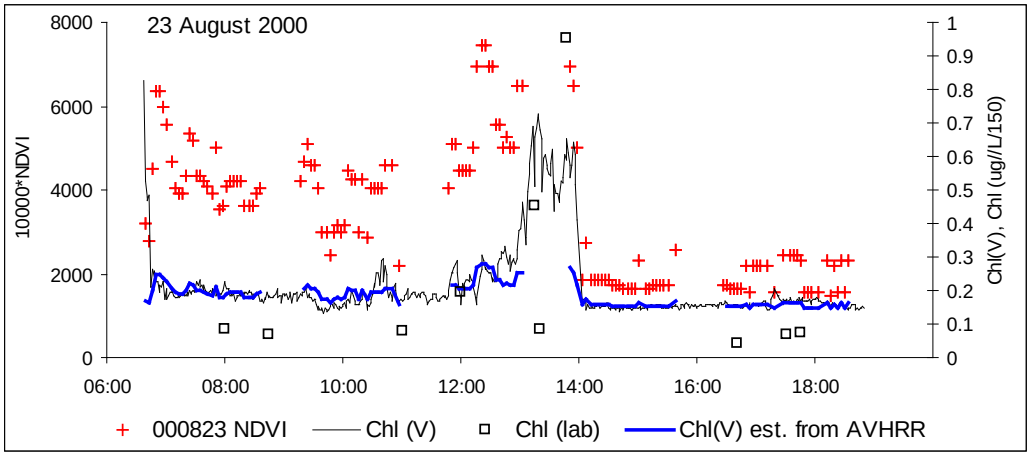

Figure 38. NDVI from 23 August 2000 AVHRR (000823 NDVI), chlorophyll fluorescence continuous flow record (Chl V), chlorophyll by filtration (Chl lab, ug/L divided by 150 to fit right axis scale) and chlorophyll fluorescence (V) estimated from AVHRR as described in text (AVHRR equation). See Figure 37 for transect location. The 23 August image was acquired at 14:38 CDST. Apparent gaps in AVHRR-derived data are associated with times when the ship was at rest for sampling.

The estimated chlorophyll fluorescence in Figure 38 is based on a best-fit exponential regression of fluorescence on NDVI. Linear and exponential relationships were tested; the latter resulted in higher r (r=0.74 after 5 outliers removed, n=128) and lower error. A multiple regression using TSS in combination with NDVI was tested and failed to improve upon the single variable model. Because the source data are from a continuous transect, the correlation coefficient is invalid. However, using the data set with outliers removed, for 7 subsets created by taking every 8th observation (i.e. observations at 8 km intervals) the mean r=0.77 and for 6 out of 7 tests r is highly significant.

We had thought that including TSS in the regression might improve the correlation. NDVI is the ratio of the difference between infrared (AVHRR Channel 2, 725-1100 nm) and red (AVHRR Channel 1, 580-680 nm) radiance to their sum. It is an indicator of chlorophyll because chlorophyll is strongly reflective in the infrared and relatively absorptive in the red. However, in a water body the great difference in attenuation between red and infrared light (Figure 2) makes interpretation of this ratio more complex. Because it sees more deeply into the water column, red light is more sensitive than infrared to low suspended mineral concentrations. The ratio of reflectance is reduced with increasing concentration. That is, the NDVI is affected by mineral sediment concentration as well as by presence of chlorophyll. However, simply adding TSS as a variable in multiple regression made only a small, probably not significant improvement in the prediction of chlorophyll fluorescence.

Figure 38 shows fluorescence estimated from NDVI. Only 23 August data were used to calculate the regression. The regression predicts small peaks and valleys in the a.m. 23rd data fairly well. However, it dramatically under predicts the magnitude of the large peak at midday on the 23rd. This peak is problematic because it occurs almost entirely at a station sampling point. Three laboratory chlorophyll samples from the vicinity of this station indicated dramatically different chlorophyll concentrations. This is important because the AVHRR integrates average albedo over 1 km^2. Sub-kilometre areas of very high concentration are averaged down.

To test whether with improved spatial resolution we could develop a better performing equation, we calculated NDVI for spectral albedo samples recorded during the cruise. These spectral distributions are illustrated in Appendix 4. Figure 39 is a scatterplot of chlorophyll versus NDVI from these samples. Obviously this is a very small data set from which to construct a model. However, it has the advantage of allowing us to calculate a chlorophyll-NDVI relationship where dependent and independent variables are sampled at more nearly the same scale. The data are from widely spaced stations (mostly >30 km apart) and essentially independent of spatial correlation.

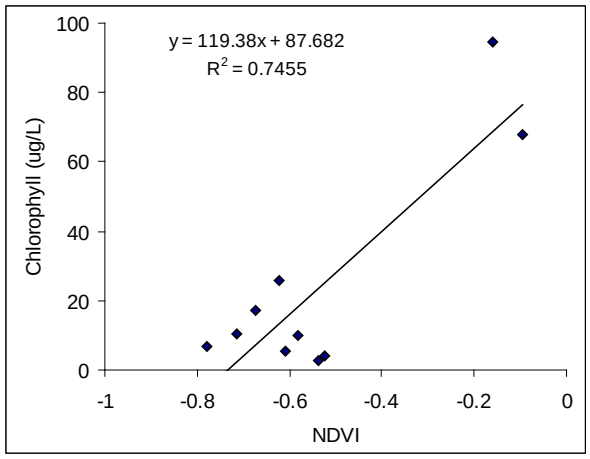

Figure 39. Chlorophyll versus NDVI calculated from spectral albedo recorded with an ASD spectrometer handheld at 1-2 m above the lake surface, off the ship's side.

With an additional linear adjustment to back-calculate fluorescence voltage from estimated chlorophyll, substituting AVHRR NDVI for x in the equation in Figure 39 gives the bold line in Figure 40, "Chl(V) est. from AVHRR". This estimation of fluorescence is considerably improved on the direct fluorescence versus AVHRR NDVI approach, probably largely because the peak fluorescence values are better sample. Intermediate values, e.g. for the morning of 23 August, are overestimated, and some low values are underestimated, but the large peak on the 23rd is accurately reproduced. The plot of the 24th indicates an estimated peak of magnitude equal to the one recorded by the continuous flow fluorometer, though it is displaced from it by about 20 km. For this section of the cruise transect, the AVHRR data is from a day earlier. Spatial distribution of algal concentrations, particularly in this region just north of the Narrows, might well have changed greatly between the time of the two records.

It is apparent from this exercise that better calibration of NDVI for chlorophyll mapping will require higher spatial resolution data than AVHRR itself. However, the performance of the model based on shipboard spectral samples seems very good given the very limited sample number from which it was derived.

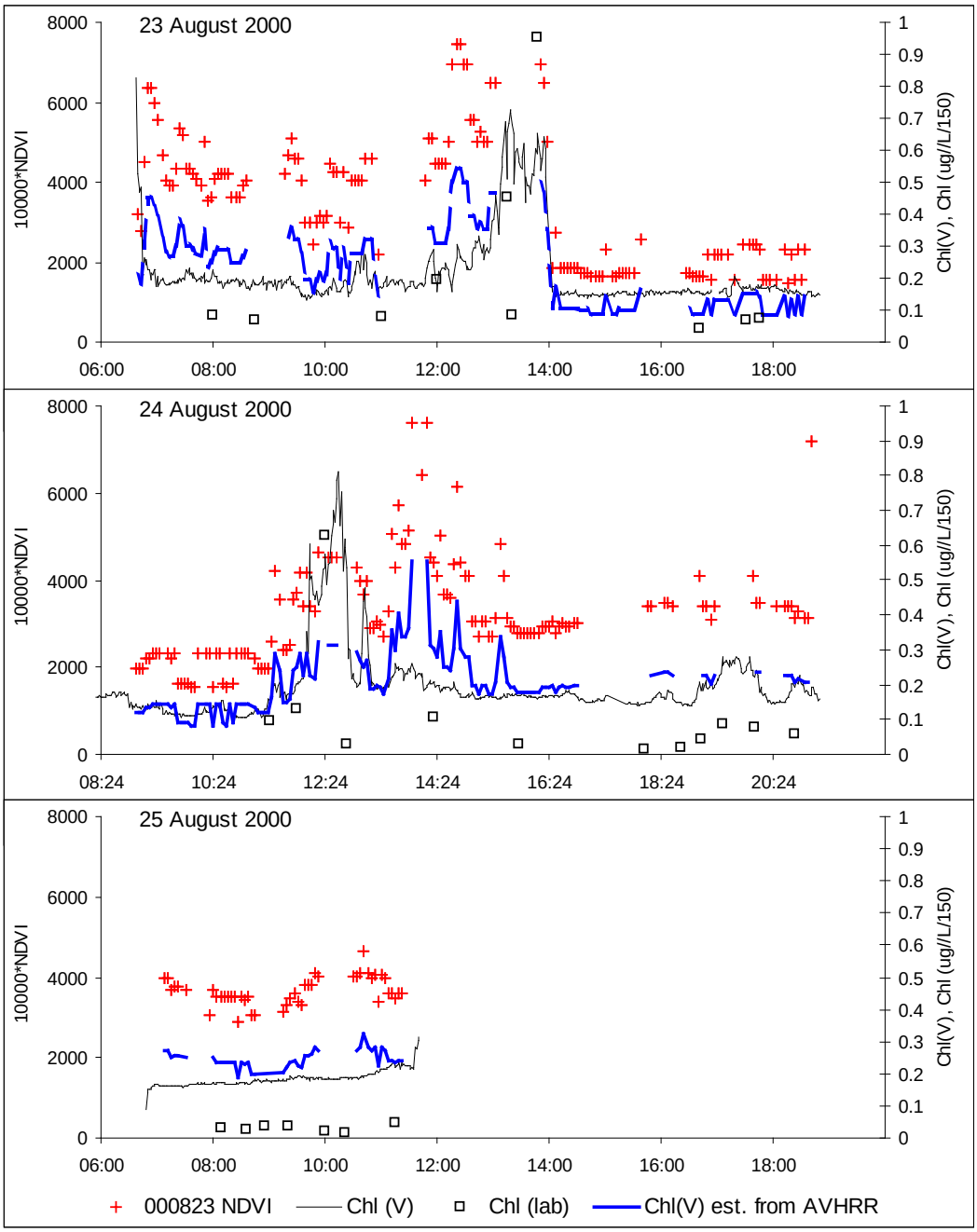

Figure 40. NDVI from 23 August 2000 AVHRR (000823 NDVI), chlorophyll fluorescence continuous flow record (Chl V), chlorophyll by filtration (Chl lab, ug/L divided by 150 to fit right axis scale) and chlorophyll fluorescence (V) estimated from AVHRR as described in text (ASD equation). See Figure 37 for transect location. The 23 August image was acquired at 14:38 CDST. Apparent gaps in AVHRR-derived data are associated with times when the ship was at rest for sampling.

6 CONCLUSIONS AND RECOMMENDATIONS

6.1 Conclusions

33 maps of surface suspended solids in Lake Winnipeg have been created, spanning the period 1985-2000. Fifteen of these illustrate Lake Winnipeg in late July-August, when productivity is expected to be near its annual maximum. Sixteen form seasonal time series, June-September for 1991, 1992, 1997 and1998. In them we find no obvious trend through time. The lake seems appears to be a little more turbid in summer and autumn than in June, but the difference is not statistically significant.

The pelagic zone in the North Basin is consistently the least turbid region, and within it, the area north of Long Point is usually clearest. The maximum TSS in the central north basin is <10 $mg \cdot L^{-1}$, and the average for a large part of the region is less than 5 $mg \cdot L^{-1}$. The eastern side, out to 10-20 km from shore is often much more turbid in response to wind-driven shore erosion and bottom resuspension events; the highest observed TSS, in excess of 200 mg.L-1, were measured along this shore.

The South Basin is more turbid. Although minimum TSS is <5 $mg \cdot L^{-1}$, the average over most of the Basin is 10-20 $mg \cdot L^{-1}$. Traverse Bay, at the mouth of the Winnipeg River, is an exception, however. The average TSS there is about 7-8 $mg \cdot L^{-1}$. The maximum TSS in the South Basin is of the order of 100 $mg \cdot L^{-1}$.

Higher TSS occurs frequently in the bays along the west side of the Narrows. In fact high TSS is very persistent in these bays, where the mean TSS is 20-40 $mg \cdot L^{-1}$. High TSS is frequent also in the area from the Narrows to Berens Island and west from there to Sturgeon Bay. This is a broad, shallow mixing area, between South and North Basin waters, and it shares with the northeast shore, near Warrens Landing, the distinction of being the area of greatest variability in TSS in the lake.

TSS in Lake Winnipeg appears to be dependent more on wind than any other factor. Correlations with the discharge of influent rivers were weak, except for the widespread inverse correlation in the North Basin with Saskatachewan River mean spring and summer discharge. Surprisingly, we did not find any correlation with the Red River discharge, in spite of including years of drought and a major spring floods.

However, there is highly positive correlation with the antecedent wind, throughout most of the east half of the North Basin, and the much of the South Basin. A similar pattern of correlation with the absolute value of the difference between North and South Basin levels is probably an artifact of the functional relationship between lake level setup and sustained winds. There is also an area of significant correlation in the Narrows-to-Berens Island area. Interestingly, this correlation is strong with the 6 h antecedent winds,

whereas turbidity in the much larger east half of the North Basin is a function of winds sustained over the longer 2 d period.

NOAA AVHRR is an ideal sensor for this type of study. Scenes are available free or at small cost beginning in 1985, and can be retrieved from off-line archives for the earlier period 1978-1984. Daily data is archived since at least 1990, allowing synoptic coverage of the whole of Lake Winnipeg for every cloud-free day over that period. The archive for the 1980s, although incomplete, nonetheless contains frequent images.

NOAA AVHRR has traditionally been used to map chlorophyll successfully mostly in Case I water, that is, in the relatively clear water of the open ocean. It is apparent from examination of Lake Winnipeg data that NDVI derived from AVHRR shows patterns of surface chlorophyll in this relatively turbid system. In this study we have shown that NDVI shows promise as a quantitative as well as qualitative measure of surface chlorophyll in Lake Winnipeg.

6.2 Recommendations

1. TSS mapping: The validation data set is weak at both high and low TSS. In practise, it is difficult to direct a program to capturing specifically high or low TSS on only cloud-free days. An alternative is to use a field spectrometer to collect data specifically for validation, possibly with a small boat off the main cruise when in appropriate waters.

2. Only a very small sample was used in testing for relationships between TSS patterns and environmental variables. In particular, the tests using the late-July August series would as a mid-summer average conditions would be enhanced by multiple sampling for each year. As an example of the short term variability in the lake, note the much higher TSS in much of Lake Winnipeg on 26 August 1999 as compared with 26 August. On the intervening day the record at Georges Island shows sustained winds in excess of 40 $km \cdot h^{-1}$.

3. Validation of the NDVI – chlorophyll relationship requires paired sampling of albedo, chlorophyll and TSS at high spatial resolution sampling. Sampling under AVHRR, with its 1 km pixel, works for TSS because TSS is more persistent over time and more homogenous over large areas than chlorophyll. It is possible and would be useful to run a field spectrometer continuously on a cruise, to take maximum advantage of the continuous record from the fluorometer and turbidity meter.

4. The calibration of the flow-through fluorometer system is critical to good validation of satellite data for both TSS and chlorophyll mapping. In particular, the existing database of chlorophyll should be checked and used to check the precision and reproducibility of the continuous-flow system.

5. Chlorophyll mapping. MODIS imagery (high spectral resolution, medium spatial resolution, almost daily overpass) should be used for future mapping work. For local studies (<100 kmx100 km) Landsat TM has high spatial and spectral resolution. TM data is available from 1984 to the present. Its major limitation is the 16-day repeat overpass, which, given average cloud conditions, results in very few clear images per open water season. For retrospective analysis, AVHRR is ideal instrument (daily coverage, free data) making further effort to validate the NDVI relationship worthwhile.

6. as a first step to improving AVHRR chlorophyll mapping capability, the MODIS data for 22-25 August 2000 should be acquired, and a cross-platform undertaken. This would take advantage of the existing TSS and chlorophyll validation data set together with the better chlorophyll response of MODIS to develop a whole-lake validation data set for AVHRR-derived NDVI.

7. The AVHRR thermal channel data is well-established as for measuring lake surface temperature. It is used operationally to map Great Lakes surface temperature. The visible and near infra-red data can also be used to map ice-off and freeze-up. Especially in a vertically mixed lake like Lake Winnipeg, these parameters in combination could be used to estimate heating degree days and midsummer temperatures for the period of AVHRR record, both parameters that would be useful in any retrospective analysis of productivity.

7 REFERENCES

Ball, G.H., and Hall, D.J., 1965. *A Novel Method of Data Analysis and Pattern Classification.* Menlo Park, CA: Stanford Research Institute.

Brunskill, G.J., Elliot, S.E.M., Campbell, P. 1980. *Morphometry, hydrology and watershed data pertinent to the limnology of Lake Winnipeg*. Canadian Manuscript Report of Fisheries and Aquatic Sciences 1556. v+32 p.

Bukata, R. P., J. H. Jerome, K. Y. Kondratyev, and D. V. Pozdnyakov. 1995. *Optical Properties and Remote Sensing of Inland and Coastal Waters.* Boca Raton, Florida: CRC Press.

Chagarlamudi, P., R. E. Hecky, and J. S. Schubert. 1980. "Quantitative Monitoring of Sediment Levels in Freshwater Lakes From Landsat." Pp. 115-18 in *The Contribution of Space Observations to Water Resources Management*, Editors V. V. Salomonson and P. D. Bhavasar. Oxford, New York: Pergamon Press.

Han, Luoheng. 1997. Spectral Reflectance With Varying Suspended Sediment Concentrations in Clear and Algae-Laden Waters. *Photogrammetric Engineering and Remote Sensing* 63(6):701-5.

Kidwell, Katherine B. 1997. *NOAA Polar Orbiter Data User Guide* (TIROS-N, NOAA-6, NOAA-7, NOAA-8, NOAA-9, NOAA-10, NOAA-11, NOAA-12, NOAA-13 AND NOAA-14). (World Wide Web URL http://www2.ncdc.noaa.gov/docs/podug/ for most recent edition)

Kirk, J. T. O.. 1980. Spectral Absorption Properties of Natural Waters: Contribution of the Soluble and Particulate Fractions to Light Absorption in Some Inland Waters of South-eastern Australia. *Australian Journal of Marine and Freshwater Research* 31:287-96.

McCullough, G.K. Determining Precision of Aquatic Turbidity Measurement by NOAA-N Series AVHRR. University of Manitoba M.A. Thesis. vi+145 p.

Morel, A. 1974. Optical Properties of Pure Water and Pure Sea Water. Pp. 1-24 in *Optical Aspects of Oceanography*, 1st ed. Ed. N. G. Jerlov and E. S. Nielsen. London: Academic Press

Morel, André and Louis Prieur. 1977. Analysis of Variations in Ocean Color. *Limnology and Oceanography* 22(4):709-22.

Munday, J.C. and Alfoldi, T.T. 1979. Landsat test of diffuse reflectance models for aquatic suspended solids measurements. *Remote Sensing of Environment.* 8:169-183.

Per Halldal. 1974. Light and Photosynthesis of Different Marine Algal Groups. Pp. 345-60 in *Optical Aspects of Oceanography*, 1st ed. Ed. N. G. Jerlov and E. S. Nielsen. London: Academic Press Inc.

Rahman, H., and G. Dedieu. 1994. SMAC: a simplified method for the atmospheric correction of satellite measurements in the solar spectrum. *International Journal for Remote Sensing* 15: 123-143.

Ritchie, J. C., F. R. Schiebe, and J. R. McHenry. 1976. Remote Sensing of Suspended Sediments in Surface Waters. *Photogrammetric Engineering and Remote Sensing* 42(12):1539-45.

Stainton, M.P., Capel, M.J. and Armstrong, F.A.J. 1977. *The Chemical Analysis of Fresh Water*. 2nd Edition. Canada Department of Fisheries and Marine Services Miscellaneous Special Publication 12. 166 p.

Stumpf, R. P. 1987. Remote Sensing of Suspended Sediments in Estuaries Using Atmospheric and Compositional Corrections to AVHRR Data. Pp.205-222 in: *21st International Symposium on Remote Sensing of Environment* (Ann Arbour, Michigan, 26 Oct-30 Oct).

Teillet, P. M. 1992. An algorithm for the radiometric and atmospheric correction of AVHRR data in the solar reflective channels. Remote Sensing of Environment 41: 185-195.

Teillet, P.M., and B.N. Holben. 1994. Towards operational radiometric calibration of NOAA AVHRR imagery in the visible and near-infrared channels. *Canadian Journal of Remote Sensing* 20: 1-10.

Whitlock, C. H., L. R. Poole, W. M. Usry, W. G. Witte, W. D. Morris, and E. A. Guganus. 1981a. Comparison of Reflectance With Backscatter and Absorption Parameters for Turbid Waters. *Applied Optics* 20:517-22.

Whitlock, C. H., W. G. Witte, T. A. Talay, W. D. Morris, J. W. Usry, and L. R. Poole. 1981b. Research for Reliable Quantification of Water Sediment Concentrations From Multispectral Scanner Remote Sensing Data. Pp. 495-510 in *Applied Modelling in Catchment Hydrology* (Proceedings of the International Symposium on Rainfall-Runoff Modelling) (Mississippi State University, Mississippi, 18 May-21 May), Ed. W. P. Singh. Littleton, Colorado: Water Resources Publications.

8 APPENDIX 1. CONTRACT REQUIREMENTS AND DELIVERABLES

Contract Requirements and Deliverables

Project Authority: Mike Stainton
Aquatic Chemistry Project Leader
Freshwater Institute
501 University Crescent
Winnipeg Manitoba
R3T 2N6

Requirement:

There are two requirements:

3. To identify possible trends in surface suspended solids quantity and patterns in L. Winnipeg over the period 1985-2000.

4. To study intra- and inter-annual seasonal variability in surface suspended solids quantity and patterns in Lake Winnipeg for flood and drought years and between warm and cool summers.

Specifically the contractor will:

Field work

Collect simultaneous lake surface albedo spectra, total suspended solids (TSS), chlorophyll and turbidity measurements on L. Winnipeg for statistical validation of relationship between in-situ suspended solids-related measures vs. at-satellite albedo.

Data assembly

Assemble historical (summers of 1994, 1999, and 2000) TSS, chlorophyll and turbidity data for L. Winnipeg from Canada Department of Fisheries and Oceans and Manitoba Department of Natural Resources.

Purchase L. Winnipeg historical hourly wind record from A.E.S.

Assemble set of historical Advanced Very High Resolution Radiometer (AVHRR) satellite scenes of L. Winnipeg, meeting the following criterion:
Calibration data set: time-coincident with historical water quality samples above. (5-10 scenes)

Inter-annual trend data set: 1985-2000 annual mid-August clear sky scenes. Some years may require more than one scene to achieve >95% clear sky coverage of L. Winnipeg. (13-20 scenes; 16 years of which 3 years acquired for item 1.)
Intra-annual variability data set: In addition to mid-August scenes (item 2), June, July and September scenes during one flood year, one drought year, one hot year, one cool year. (12-20 scenes.)

Create TSS and NDVI maps

Spatially/temporally match water quality samples with clear sky pixels on calibration scenes. Establish relationship between in-situ suspended solids-related measures vs. at-satellite albedo.

Calculate TSS map for each scene using validated relationship.

Calculate NDVI map for each scene as (C2-C1)/(C2+C1).

Prepare as a set of figures for hard copy report and as electronic files on accompanying CD.

Analysis

PRECISION

Report and discuss precision of estimated, mapped parameters.

ASSOCIATION OF NDVI WITH CHLOROPHYLL-A

Analyze and discuss correlations between NDVI and surface measurements of chlorophyll-a.

ASSOCIATION OF TSS AND NDVI

Analyze and discuss spatial correlations between TSS and NDVI.

TSS AND NDVI TREND, 1985-2000

Subdivide lake into major regions (e.g. N ½ of N basin, S ½ of N basin, Narrows region, S. basin) and tabulate TSS and NDVI stats for each scene/region.

Plot time series. Discuss plot trends, anomalies, etc. in terms of antecedent wind, mean summer temperature, lake level, major river antecedent inflow.

TSS AND NDVI COMPARED FOR FLOOD VS. DROUGHT AND WARM VS. COOL SUMMER

Tabulate TSS and NDVI for regions as for inter-annual trend, above.

Plot and discuss as for inter-annual trend, above.

Deliverables are:

TSS AND NORMALIZED DIFFERENCE VEGETATION INDEX (NDVI) TREND, 1985-2000

Annual mid-August maps of TSS and NDVI for L. Winnipeg, 1985-2000 (print copy and digital files on CD. Data on CD will include L. Manitoba, L. Winnipegosis, Cedar L.).

Plots of TSS and NDVI trends by major regions of L. Winnipeg (e.g. N ½ of N basin, S ½ of N basin, Narrows region, S. basin).

Discussion of plot trends, anomalies, etc. in terms of antecedent wind, mean summer temperature, lake level, major river antecedent inflow.

TSS AND NDVI COMPARED FOR FLOOD VS. DROUGHT AND WARM VS. COOL SUMMER

Mid-June, July, August, September maps of TSS and NDVI for L. Winnipeg for 4 different years, including one each of flood, drought, warm and cool summer (print copy and digital files on CD. Data on CD will include L. Manitoba, L. Winnipegosis, Cedar L).

Comparison of TSS and NDVI between flood vs. drought, warm vs. cool summer, by major regions of L. Winnipeg (e.g. N ½ of N basin, S ½ of N basin, Narrows region, S. basin).

Discuss data in terms of antecedent wind, mean summer temperature, lake level, major river antecedent inflow

9 APPENDIX 3. WIND DATA FOR DATES OF AVHRR OVERPASSES

Table 3.1. Hourly 10 m above surface wind data recorded at Gimli and Georges Island. Bold: speed ($km \cdot h^{-1}$). Regular: Direction (10s of degrees azimuth). Hours are indicated in Row 1.

Date	Station	1	2	3	4	5	6	7	8	9	10	11	12	13	14	15	16	17	18	19	20	21	22	23	24
1985 Jul 26	Gimli 1	**7**	**7**	**7**	**9**	**7**	**7**	**7**	**7**	**9**	**11**	**9**	**7**	**9**	**11**	**13**	**13**	**13**	**13**	**11**	**11**	**7**	**9**	**13**	**13**
		28	27	27	26	25	26	25	25	24	24	25	30	35	5	20	7	3	36	4	36	35	33	35	33
1985 Aug 24	Gimli 1	**0**	**7**	**7**	**7**	**6**	**7**	**6**	**0**	**0**	**6**	**15**	**11**	**9**	**9**	**6**	**9**	**7**	**6**	**4**	**6**	**7**	**7**	**7**	**6**
		14	15	12	12	12	12	14	28	34	30	26	1	7	6	10	0	0	0	0	1	0	0	33	34
1986 Aug 12	Gimli 1	**9**	**13**	**11**	**11**	**11**	**11**	**13**	**15**	**19**	**15**	**15**	**15**	**15**	**19**	**17**	**20**	**15**	**11**	**15**	**9**	**9**	**7**	**6**	**6**
		27	30	0	0	25	27	26	25	24	0	10	11	11	11	12	13	14	16	24	24	0	21	21	21
1987 Aug 20	Gimli 1	**7**	**7**	**7**	**7**	**9**	**11**	**7**	**7**	**13**	**7**	**4**	**9**	**11**	**13**	**15**	**11**	**9**	**9**	**7**	**2**	**6**	**6**	**11**	**19**
		26	25	0	25	25	27	25	27	25	26	25	24	26	23	24	26	24	24	24	23	0	31	24	25
1988 Aug 15	Georges I 2	**9**	**11**	**17**	**19**	**17**	**20**	**20**	**24**	**19**	**24**	**11**	**9**		**11**	**6**	**17**	**11**		**22**	**15**	**11**	**9**		**6**
						36	36	2		28	27	28	31			18	19		18	18	18	17			
1988 Aug 15	Gimli 1	**11**	**11**	**6**	**7**	**6**	**7**	**7**	**19**	**20**	**17**	**19**	**22**	**20**	**19**	**19**	**17**	**15**	**9**	**9**	**9**	**15**	**11**	**7**	**7**
		34	33	31	30	29	30	30	28	30	32	30	12	11	12	11	10	13	13	14	15	17	16	20	17
1989 Aug 15	Georges I 2	**7**	**6**	**7**	**6**	**6**	**7**	**9**	**7**	**9**	**9**	**11**	**9**	**7**	**11**	**15**	**17**	**17**	**15**	**13**	**13**	**11**	**9**	**7**	**7**
		5	5	5	5	6	9	9	9	10	10	10	12		6	2	2	1	34			32	32	32	30
1989 Aug 15	Gimli 1	**7**	**7**	**7**	**4**	**6**	**7**	**7**	**0**	**0**	**6**	**6**	**6**	**7**	**9**	**9**	**9**	**7**	**7**	**6**	**0**	**0**	**6**	**7**	**6**
		33	33	33	33	33	33	33	33	34	36	3	4	4	6	7	6	2	7	3	36	0	30	29	29
1990 Aug 21	Georges I 2	**7**	**9**	**15**	**22**	**24**	**22**	**22**	**28**	**28**	**26**	**24**	**28**	**26**	**22**	**19**	**20**	**19**	**13**	**19**	**13**	**11**	**15**	**22**	**22**
		18	18	19	19	20	18	19	21	19	17	18	18	18	18	18	18	18	18	18	17	17	16	15	15
1990 Aug 21	Gimli 1	**9**	**9**	**2**	**4**	**6**	**7**	**6**	**7**	**7**	**7**	**7**	**11**	**11**	**11**	**7**	**13**	**7**	**11**	**6**	**7**	**9**	**9**	**7**	**6**
		5	7	9	17	23	21	0	19	17	0	9	12	12	11	10	7	6	9	8	10	12	11	18	17
1991 Jun 21	Georges I 2	**17**	**20**	**22**	**22**	**22**	**24**	**26**	**24**	**20**	**20**	**19**	**13**	**9**	**7**	**6**	**4**	**6**	**6**	**17**	**19**	**17**	**17**	**19**	**20**
		35	32	36	4	4	5	5	5	4	2	5	5	5	7	5	1	36	34	32	32	32	32	32	32
1991 Jun 21	Gimli 1	**30**	**31**	**22**	**24**	**24**	**22**	**22**	**17**	**13**	**13**	**17**	**19**	**19**	**19**	**19**	**19**	**19**	**19**	**13**					
		3	3	3	4	6	6	6	6	3	3	2	2	2	2	3	3	4	1	1					
1991 Jul 13	Georges I 2	**26**	**20**	**19**	**15**	**13**	**7**	**4**	**6**		**6**	**4**	**6**	**9**	**9**	**9**	**9**	**13**	**9**	**11**	**9**	**7**	**6**	**7**	**7**
		36	10	10	8	5	5	5	5	5	5	5	5	5	5	5	3	4	2	4	5	36	36	32	32
1991 Jul 13	Gimli 1	**11**	**9**	**9**	**9**	**9**	**6**	**7**	**7**	**9**	**7**	**7**	**9**	**9**	**11**	**9**	**11**	**9**	**6**	**15**					
		6	6	5	4	4	2	2	4	3	2	2	2	2	3	4	1	1	36	35					

Table 3.1 (continued). Hourly 10 m above surface wind data recorded at Gimli and Georges Island. Bold: speed ($km \cdot h^{-1}$). Regular: Direction (10s of degrees azimuth). Hours are indicated in Row 1.

Date	Station	1	2	3	4	5	6	7	8	9	10	11	12	13	14	15	16	17	18	19	20	21	22	23	24
1991 Aug 11	Georges I 2	**9**	**13**	**19**	**22**	**22**	**20**	**22**	**22**	**22**	**24**	**22**	**22**	**19**	**17**	**17**	**15**	**11**	**11**	**11**	**9**	**9**	**6**	**6**	**7**
		18	18	18	18	18	18	18	18	18	18	18	18	18					16	16	15	14	14	14	14
1991 Aug 11	Gimli 1	**6**	**6**	**7**	**7**	**6**	**9**	**7**	**4**	**4**	**4**	**6**	**7**	**6**	**9**	**9**	**9**	**9**	**9**	**9**					
		23	22	28	17	19	23	22	18	20	20	13	12	14	11	10	11	13	16	0					
1991 Sep 20	Georges I 2	**28**	**33**	**37**	**37**	**43**	**41**	**43**	**43**	**43**	**43**	**43**	**39**	**41**	**41**	**43**	**43**	**37**	**35**	**32**	**26**	**24**	**26**	**24**	**26**
		36	33	33	3	2	3	1	3	1	35	34	33	33	32	32	25	30	32	30	25	23	22	22	18
1991 Sep 20	Gimli 1	**19**	**13**	**19**	**19**	**19**	**15**	**15**	**15**	**17**	**19**	**20**	**24**	**19**											
		28	28	27	27	28	28	27	27	27	27	27	27	27											
1992 Jun 15	Georges I 2	**17**	**17**	**15**	**15**	**13**	**9**	**7**	**6**	**6**	**7**	**9**	**6**		**6**	**4**	**6**	**6**	**7**	**7**	**6**	**6**	**11**	**9**	**11**
		35	36	36	4	5	5	7	9	12	9	10	10		12	15	19	23	32	31	32	32	32	32	32
1992 Jul 22	Georges I 2	**17**	**17**	**20**	**24**	**32**	**24**	**24**	**20**	**24**	**28**	**26**		**24**	**24**	**26**	**22**	**20**	**19**	**15**	**13**	**19**	**15**	**15**	**17**
		23	23	23	24	25	25	26	26	27	27	27	27	28	27	29	29	28	26	23	23	23	21	20	19
1992 Aug 16	Georges I 2	**17**	**11**	**19**	**13**	**26**	**22**	**19**	**19**	**15**	**15**	**20**	**20**	**17**	**33**	**43**	**39**	**37**	**35**	**32**	**28**	**28**	**22**	**17**	**7**
		18	18	18	18	18	18	18	18	18	18	18	18	18	18	18	17	18	18	17	15	15	16	15	15
1992 Aug 18	Georges I 2	**13**	**13**	**13**	**15**	**15**	**15**	**13**	**13**	**15**	**15**	**15**	**13**	**7**	**11**	**9**	**2**	**6**	**7**	**9**	**9**	**6**	**7**	**6**	**6**
		32	27	27	26	29	29	32	32	32	32	32	32	32	32	32	33	35	33	32	32	33	32	32	29
1992 Sep 11	Georges I 2	**15**	**19**	**32**	**35**	**33**	**35**	**32**	**35**	**43**	**41**	**41**	**41**	**41**	**44**	**44**	**35**	**30**	**19**	**24**	**28**	**20**	**24**	**22**	**17**
		5	5	5	5	5	5	5	5	5	5	8	9	8	9	15	16	16	17	18	18	18	18	18	16
1994 Aug 10	Georges I 2	**13**	**17**	**17**	**17**	**15**	**17**	**17**	**15**	**13**	**19**	**13**		**11**	**7**	**11**	**13**	**15**	**19**	**17**	**15**	**9**	**6**	**2**	**6**
		23	25	25	23	25	25	24	25	24	23	23	23	23	23	23	23	23	23	23	23	23	23	23	25
1994 Aug 10	Gimli 2	**4**	**4**	**4**	**0**	**6**	**11**	**0**	**0**	**9**	**0**	**0**	**4**		**0**	**7**	**9**	**13**	**7**	**7**	**7**	**7**	**4**	**6**	**6**
		28	26	28	27	26	25	32	0	21	20	19	21	21	14		10	9	13	15	12	0	0	0	29
1994 Aug 19	Georges I 2	**19**	**11**	**7**	**6**	**6**	**2**	**6**	**6**	**6**	**7**	**6**	**4**	**13**	**15**	**13**	**13**	**17**	**15**	**13**	**9**	**7**	**6**	**6**	**9**
		5	9	10	8	10	6	9	10	10	5	5	5	5	5	3	4		25	32	34	36	36	36	36
1994 Aug 19	Gimli 2	**7**	**9**	**9**	**11**	**9**	**11**	**13**	**15**	**17**	**20**	**19**	**19**	**19**	**15**	**15**	**20**	**15**	**13**	**17**	**9**	**11**	**11**	**11**	**13**
		36		35	33	28	33	30	0	8	5	3	0	8	7	10	9	7	6	5	36	9	5	3	35
1995 Aug 21	Georges I 2	**33**	**37**	**33**	**33**	**30**	**32**	**28**	**26**	**24**	**22**	**20**	**15**	**9**	**4**	**4**	**7**	**7**	**13**	**15**	**11**	**20**	**17**	**22**	**20**
		25	26	28	28	29	28	27	27	29	29	29	27	28	32	32	32	32	32	32	32	32	32	32	32

Table 3.1 (continued). Hourly 10 m above surface wind data recorded at Gimli and Georges Island. Bold: speed ($km \cdot h^{-1}$). Regular: Direction (10s of degrees azimuth). Hours are indicated in Row 1.

Date	Station	1	2	3	4	5	6	7	8	9	10	11	12	13	14	15	16	17	18	19	20	21	22	23	24
1995 Aug 21	Gimli 2	**9**	**11**	**7**	**7**	**6**	**7**	**9**	**6**	**7**	**13**	**9**	**7**	**11**	**7**	**0**	**13**	**11**	**9**	**9**	**9**	**7**	**6**	**4**	**7**
		23	24	24	25	26	25	25	26	27	28	28	28	27	28	28	29	28	30	31	31	30	29	30	30
1996 Aug 27	Georges I 2	**43**	**37**	**44**	**44**	**44**	**52**	**48**	**48**	**46**	**43**	**33**	**26**	**20**	**15**	**11**	**11**	**11**	**13**	**11**	**13**	**15**	**11**	**9**	**9**
		28	32	32	27	32	0	11	12	18	18	18	18	18	17	15	14	14	17	18	18	18	18	18	18
1996 Aug 27	Gimli 2	**24**	**17**	**17**	**19**	**19**	**19**	**17**	**17**	**22**	**20**	**30**	**20**	**33**	**37**	**28**	**32**	**30**	**22**	**17**	**11**	**15**	**11**	**13**	**9**
		29	28	29	29	25	0	25	23	0	20	21	22	14	14	21	23	23	20	18	17	17	18	19	19
1997 Jun 06	Georges I 2	**22**	**24**	**20**	**17**	**13**	**17**	**13**	**13**	**6**	**6**	**7**	**11**	**7**	**7**	**2**	**15**	**13**	**13**	**13**	**11**	**13**	**15**	**13**	**17**
		32	36	5	5	4	36	36	33	35	33	32	36	32	32	32	32	32	32	32	32	33	36	5	5
1997 Jun 06	Gimli 2	**9**	**7**	**9**	**7**	**7**	**6**	**7**	**11**	**13**	**6**	**11**	**7**	**13**	**9**	**15**	**17**	**11**	**11**	**13**	**11**	**7**	**7**	**6**	**9**
		1	2	2	36	34	33	35	2	5	3	33	5	4	3	3	5	2	2	1	2	2	1	36	36
1997 Jul 29	Georges I 2	**9**	**7**	**9**	**11**	**13**	**9**	**7**	**9**	**9**	**6**	**11**	**13**	**15**	**11**	**11**	**13**	**13**	**9**	**15**	**24**	**26**	**26**	**26**	**26**
		5	5	5	5	9	8	5	5	3	2	32	31	29	28	28	31	31	31	32	32	33	34	32	23
1997 Jul 29	Gimli 2	**9**	**6**	**7**	**4**	**0**	**4**	**0**	**7**	**6**	**9**	**6**	**6**	**11**	**17**	**11**	**9**	**15**	**13**	**13**	**9**	**9**	**4**	**4**	**6**
		34	31	29	32	33	32	34	32	35	1	1	4	6	6	5	4	3	3	2	4	32	32	32	32
1997 Aug 21	Georges I 2	**19**	**17**	**15**	**13**	**11**	**7**	**7**	**9**	**7**	**9**	**13**	**2**	**0**	**7**	**11**	**13**	**11**	**11**	**7**	**4**	**6**	**4**	**2**	**2**
		27	32	32	32	32	32	32	31	36	32	32	32	32	32	31	32	32	32	32	32	32	36	36	36
1997 Aug 21	Gimli 2	**4**	**6**	**11**	**7**	**11**	**9**	**13**	**7**	**9**	**9**	**11**	**13**	**13**	**9**	**13**	**13**	**9**	**6**	**0**	**6**	**0**	**0**	**4**	**6**
		19	23	26	28	29	28	28	29	31	31	31	30	30	30	32	35	34	35	35	0	34	30	31	31
1997 Aug 26	Georges I 2	**37**	**32**	**26**	**26**	**26**	**28**	**24**	**26**	**28**	**30**	**30**	**28**	**30**	**26**	**22**	**24**	**28**	**22**	**22**	**19**	**17**	**20**	**32**	**28**
		12	12	11	12	13	13	18	23	28	25	23	23	23	23	26	27	27	26	27	27	28	29	30	32
1997 Aug 26	Gimli 2	**9**	**9**	**13**	**7**	**7**	**7**	**6**	**11**	**11**	**11**	**15**	**19**	**15**	**15**	**19**	**19**	**9**	**6**	**9**	**4**	**6**	**0**	**7**	**7**
		15	16	17	16	17	18	18	20	23	28	27	27	27	26	27	26	27	29	28	28	26	28	26	28
1997 Sep 24	Georges I 2	**24**	**26**	**20**	**19**	**19**	**17**	**17**	**19**	**19**	**22**	**24**	**26**	**28**	**28**	**24**	**24**	**35**	**35**	**33**	**32**	**30**	**26**	**28**	**28**
		18	18	18	18	18	18	18	18	18	18	18	18	18	18	18	18	18	18	18	18	19	23	23	25
1997 Sep 24	Gimli 2	**32**	**24**	**30**	**26**	**17**	**17**	**15**	**15**	**15**	**26**	**26**	**26**	**26**	**26**	**22**	**41**	**26**	**28**	**17**	**13**	**13**	**13**	**15**	**17**
		28	29	29	26	22	23	22	22	22	21	21	20	20	19	19	21	21	21	21	20	20	21	22	23
1998 Jun 22	Georges I 2	**37**	**30**	**24**	**22**	**22**	**19**	**17**	**13**	**15**	**17**	**19**	**19**	**15**	**15**	**11**	**11**	**4**	**4**	**4**	**9**	**11**	**17**	**15**	**13**
		36	36	36	36	36	36	36	36	34	34	34	35	32	32	32	32	32	34	32	36	36	36	36	36

Table 3.1 (continued). Hourly 10 m above surface wind data recorded at Gimli and Georges Island. Bold: speed ($km \cdot h^{-1}$). Regular: Direction (10s of degrees azimuth). Hours are indicated in Row 1.

Date	Station	1	2	3	4	5	6	7	8	9	10	11	12	13	14	15	16	17	18	19	20	21	22	23	24
1998 Jun 22	Gimli 2	**17**	**13**	**13**	**11**	**15**	**15**	**20**	**17**	**15**	**17**	**19**	**13**	**11**	**11**	**9**	**9**	**9**	**11**	**7**	**9**	**7**	**7**	**6**	**4**
		28	25	27	25	25	27	28	28	28	30	30	30	29	30	31	30	29	28	28	30	31	28	30	29
1998 Jul 19	Georges I 2	**19**	**28**	**32**	**39**	**35**	**35**	**30**	**26**	**24**	**26**	**24**	**24**	**20**	**17**	**19**	**17**	**13**	**11**	**13**	**15**	**13**	**13**	**17**	**19**
		23	23	24	20	14	12	15	13	11	15	17	18	16	18	13	13	5	5	36	32	33	23	26	28
1998 Jul 19	Gimli 2	**7**	**20**	**17**	**9**	**11**	**13**	**15**	**17**	**19**	**17**	**19**	**17**	**19**	**13**	**13**	**19**	**11**	**0**	**6**	**6**	**4**	**0**	**0**	**0**
		18	17	0	14	13	14	7	14	15	15	16	12	8	17	21	25	32	31	31	31	28	26	26	25
1998 Jul 27	Georges I 2	**30**	**22**	**24**	**20**	**26**	**20**	**19**	**19**	**17**	**13**	**11**	**17**	**17**	**9**	**24**	**13**	**9**	**22**	**7**	**13**	**20**	**56**	**32**	**32**
		18	25	23	25	27	27	27	29	28	29	29	29	31	31	29	29	30	30	31	32	32	32	32	32
1998 Jul 27	Gimli 2	**11**	**13**	**11**	**11**	**11**	**11**	**11**	**13**	**19**	**19**	**22**	**17**	**20**	**24**	**24**	**17**	**20**	**19**	**15**	**11**	**22**	**9**	**15**	**13**
		19	19	21	12	17	19	22	26	30	31	30	30	30	31	30	31	30	30	31	30	30	28	29	29
1998 Aug 17	Georges I 2	**28**	**28**	**24**	**24**	**22**	**19**	**15**	**15**	**13**	**11**	**6**	**6**	**4**	**6**	**9**	**9**	**9**	**6**	**4**	**4**	**6**	**7**	**9**	**7**
		11	12	15	15	15	19	4	36	36	36	36	36	36	36	36	36	2	36	3	3	3	4	4	4
1998 Aug 17	Gimli 2	**17**	**17**	**15**	**17**	**15**	**17**	**20**	**17**	**20**	**20**	**19**	**17**	**19**	**9**	**11**	**6**	**7**	**6**	**9**	**6**	**7**	**6**	**0**	**4**
		19	20	19	20	20	21	19	19	22	26	30	29	32	31	33	33	35	36	35	35	35	35	1	2
1998 Sep 11	Georges I 2	**17**	**15**	**13**	**17**	**13**	**7**	**7**	**11**	**13**	**15**	**11**	**15**	**15**	**11**	**9**	**9**	**7**	**7**	**13**	**11**	**19**	**19**	**28**	**30**
		16	16	17	16	17	18	18	18	18	18	18	24	31	32	32	32	32	32	32	32	32	32	36	36
1998 Sep 11	Gimli 2	**19**	**15**	**15**	**15**	**11**	**15**	**13**	**15**	**15**	**15**	**13**	**19**	**17**	**19**	**15**	**9**	**9**	**7**	**4**	**0**	**7**	**7**	**6**	**4**
		17	16	16	16	16	16	17	17	19	19	20	18	19	23	25	27	31	33	2	36	35	35	36	36
1999 Aug 12	Georges I 2	**9**	**7**	**6**	**7**	**9**	**7**	**9**	**13**	**15**	**15**	**17**	**13**	**15**	**15**	**19**	**19**	**20**		**30**	**30**	**30**	**24**	**24**	**22**
		2	36	36	4	5	5	5	5	5	4	1	32	32	32	32	32	32	32	32	32	32	35	32	32
1999 Aug 12	Gimli 2	**9**	**11**	**6**	**6**	**6**	**7**	**6**	**6**	**15**	**15**	**15**	**20**	**20**	**20**	**17**	**17**	**17**	**17**	**17**	**9**	**13**	**13**	**11**	**11**
		34	35	35	33	31	30	31	33	34	1	5	5	5	7	7	4	4	4	4	2	35	36	35	36
1999 Aug 18	Georges I 2	**9**	**9**	**9**	**7**	**7**	**6**	**6**	**6**	**0**	**9**	**9**	**11**	**13**	**17**	**17**	**17**	**24**	**24**	**24**	**24**	**28**	**32**	**30**	**28**
		8	9	10	10	11	13	13	15	14	15	18	17	18	18	18	18	18	23	23	23	22	24	26	24
1999 Aug 18	Gimli 2	**13**	**11**	**13**		**11**	**9**	**7**	**11**	**11**	**7**						**11**	**4**	**4**	**6**	**6**	**7**	**6**	**4**	**4**
		0	0	0	2	10	7	8	17	0	15	12	13	13	10	7	7	10	9	7	5	1	33	33	33
1999 Aug 19	Georges I 2	**30**	**28**	**26**	**24**	**22**	**20**	**22**	**20**	**24**	**22**	**19**	**22**	**19**	**17**	**19**	**24**	**22**	**26**	**24**	**26**	**26**	**26**	**17**	**15**
		27	27	27	26	26	25	23	24	0	22	18	21	20	21	18	18	18	18	18	18	18	19	23	23

Table 3.1 (continued). Hourly 10 m above surface wind data recorded at Gimli and Georges Island. Bold: speed ($km \cdot h^{-1}$). Regular: Direction (10s of degrees azimuth). Hours are indicated in Row 1.

Date	Station	1	2	3	4	5	6	7	8	9	10	11	12	13	14	15	16	17	18	19	20	21	22	23	24
1999 Aug 19	Gimli 2	**7**	**4**	**6**	**4**	**6**	**0**	**6**	**7**	**9**	**6**	**13**	**9**	**13**	**17**	**9**	**7**	**7**	**7**	**11**	**6**	**6**	**11**	**9**	**13**
		35	34	32		32	34	34	34	33	36						9	11	8	11	15	27	23	26	22
1999 Aug 24	Georges I 2	**17**	**15**	**22**	**20**	**19**	**13**	**15**	**19**	**20**	**20**	**24**	**28**	**26**	**24**	**26**	**24**	**22**	**20**	**20**	**22**	**28**	**20**	**26**	**26**
		4	7	3	4	36	36	33	32	32	33	32	32	32	32	32	32	34	32	0	23	22	22	23	23
1999 Aug 24	Gimli 2	**4**	**4**	**6**	**6**	**6**	**4**	**4**	**0**	**0**	**6**	**7**	**9**	**11**	**15**	**13**	**11**	**13**	**11**	**7**	**4**	**6**	**6**	**7**	**13**
		25	20	23	28	35	34	2	32	33	33	35	31	33	31	8	1	2	33	36	3	3	0	33	1
1999 Aug 26	Georges I 2	**44**	**41**	**32**	**30**	**33**	**32**	**41**	**35**	**22**	**19**	**19**	**24**	**22**	**20**	**28**	**32**	**28**	**30**	**28**	**30**	**26**	**24**	**30**	**20**
		18	18	18	18	18	17	17	16	15	15	14	14	15	14	14	15	15	15	14	14	15	16	18	18
1999 Aug 26	Gimli 2	**33**	**35**	**33**	**30**	**28**	**24**	**17**	**13**	**30**	**24**	**24**	**20**	**15**	**13**	**13**	**20**	**22**	**19**	**13**	**9**	**11**	**11**	**7**	**7**
		19	20	20	19	20	19	19	19	19	19	18	18	18	17	18	18	18	17	18	18	17	18	19	19
2000 Aug 22	Georges I 2		**17**	**15**	**15**	**15**	**15**	**11**	**11**	**13**	**15**	**22**	**17**	**13**	**15**	**15**	**17**	**13**	**19**	**19**	**9**	**13**	**13**	**13**	**15**
		12	12	22	10	32	27	27	27	27	27	27	27	27	26	24	24	25	24	26	25	26	24	24	24
2000 Aug 22	Gimli 2	**9**	**7**	**11**	**13**	**15**	**19**	**17**	**13**	**15**	**20**	**24**	**17**	**17**	**19**	**19**	**17**	**17**	**13**	**9**	**6**	**0**	**6**	**6**	**9**
		18	20	22	22	26	25	25	27	27	27	26	28	28	27	28	28	28	28	26	23	24	24	25	24
2000 Aug 23	Georges I 2	**15**	**19**	**17**	**15**	**19**	**17**	**17**	**19**	**15**	**17**	**20**	**26**	**26**	**20**	**19**	**22**	**24**	**26**	**30**	**32**	**33**	**33**	**37**	**33**
			23	23	23	22	23	26	26	27	27	28	29	27	27	27	28	27	28	28	27	24	23	23	23
2000 Aug 23	Gimli 2	**6**	**6**	**6**	**7**	**4**	**6**	**6**	**6**	**7**	**9**	**17**	**20**	**22**	**19**	**22**	**20**	**22**	**17**	**11**	**6**	**11**	**9**	**9**	**11**
		23	23	24	24	25	26	25	24	23	24	25	26	23	21	22	23	24	29	31	30	0	28	27	27
2000 Aug 25	Georges I 2	**24**	**24**	**26**	**28**	**37**	**35**	**39**	**32**	**28**	**17**	**15**	**20**	**26**	**28**	**30**	**26**	**28**	**26**	**24**	**20**	**20**	**19**	**19**	**22**
		18	18	18	18	18	21	22	16	18	18	18	18	18	19	31	32	18	25	23	27	27	27	27	28
2000 Aug 25	Gimli 2	**11**	**9**	**13**	**7**	**7**	**7**	**6**	**11**	**13**	**9**	**11**	**17**	**15**	**19**	**24**	**19**	**19**	**11**	**13**	**11**	**11**	**9**	**6**	**7**
		19	19	20	20	21	21	20	20	18	19	20	20	13	15	14	18	22	29	34	33	32	34	34	34
2000 Sep 14	Gimli 2	**15**	**11**	**13**	**17**	**17**	**15**	**15**	**11**	**15**	**17**	**20**	**24**	**22**	**26**	**20**	**19**	**22**	**15**	**11**	**4**	**0**	**7**	**7**	**0**
		27	32	28	28	30	30	29	29	30	29	30	27	29	27	29	32	30	31	31	30	32	31	31	31

10 APPENDIX 3. TIME SERIES OF NDVI MAPS

Normalized Difference Vegetation Index, July and August 1985.

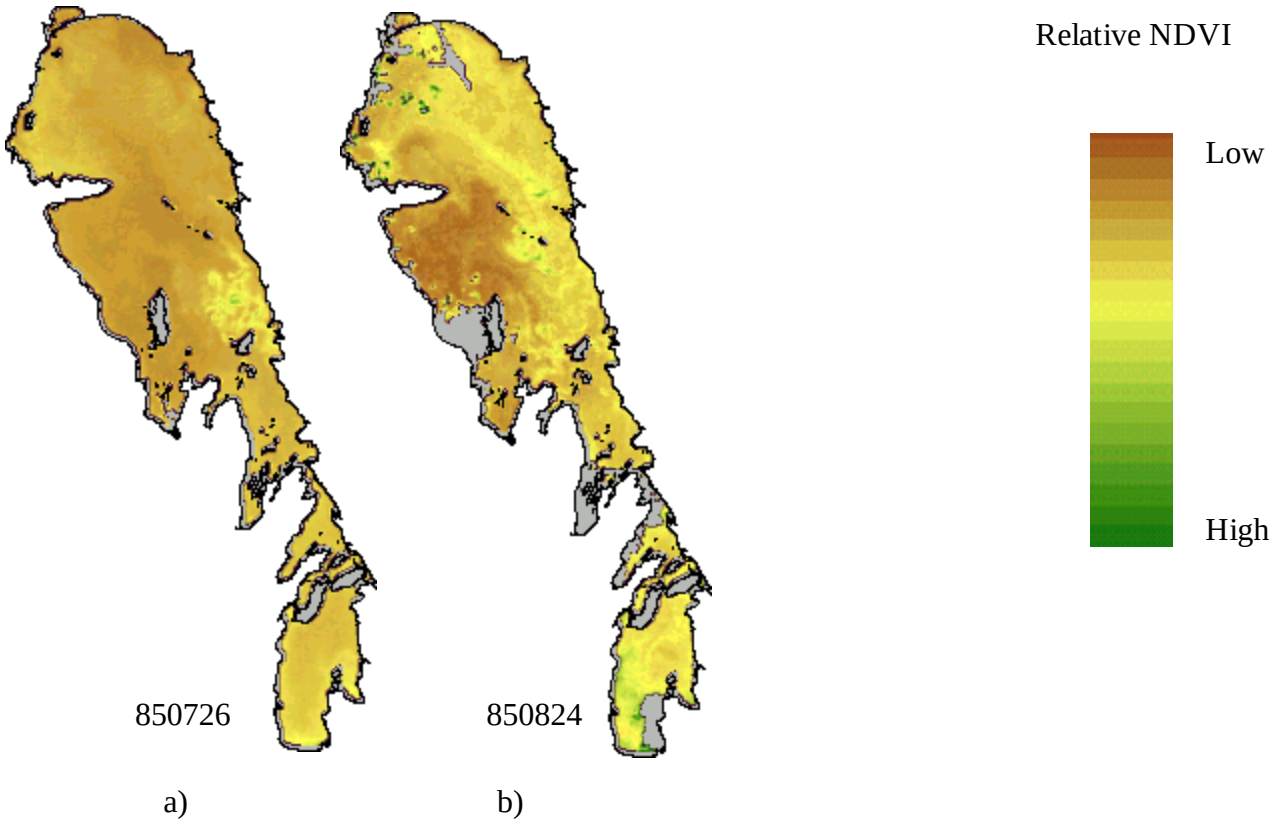

Figure 3.1. NDVI calculated from NOAA AVHRR data. Dates are in YYMMDD format.

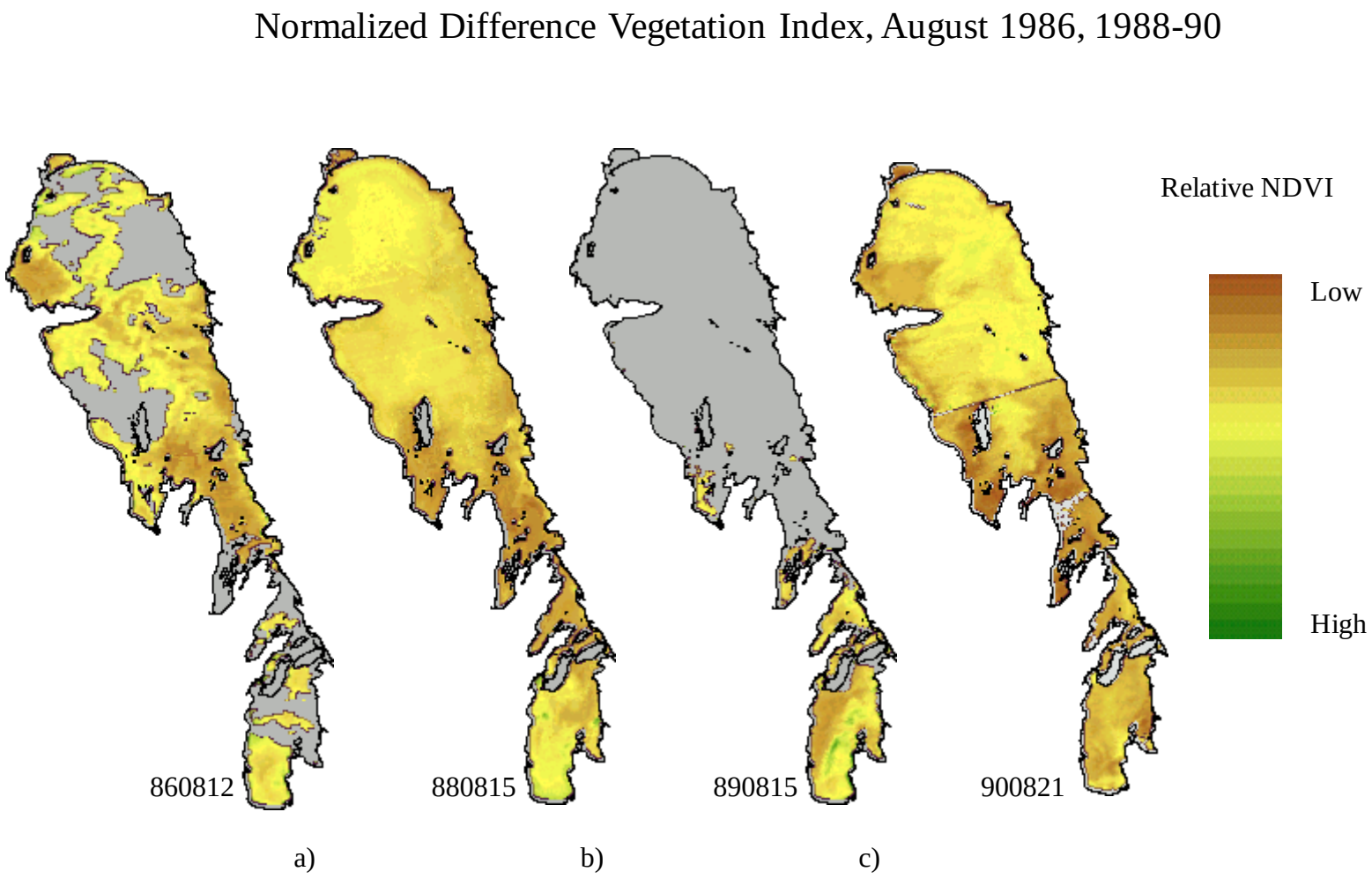

Figure 3.2. NDVI calculated from NOAA AVHRR data. Dates are in YYMMDD format.

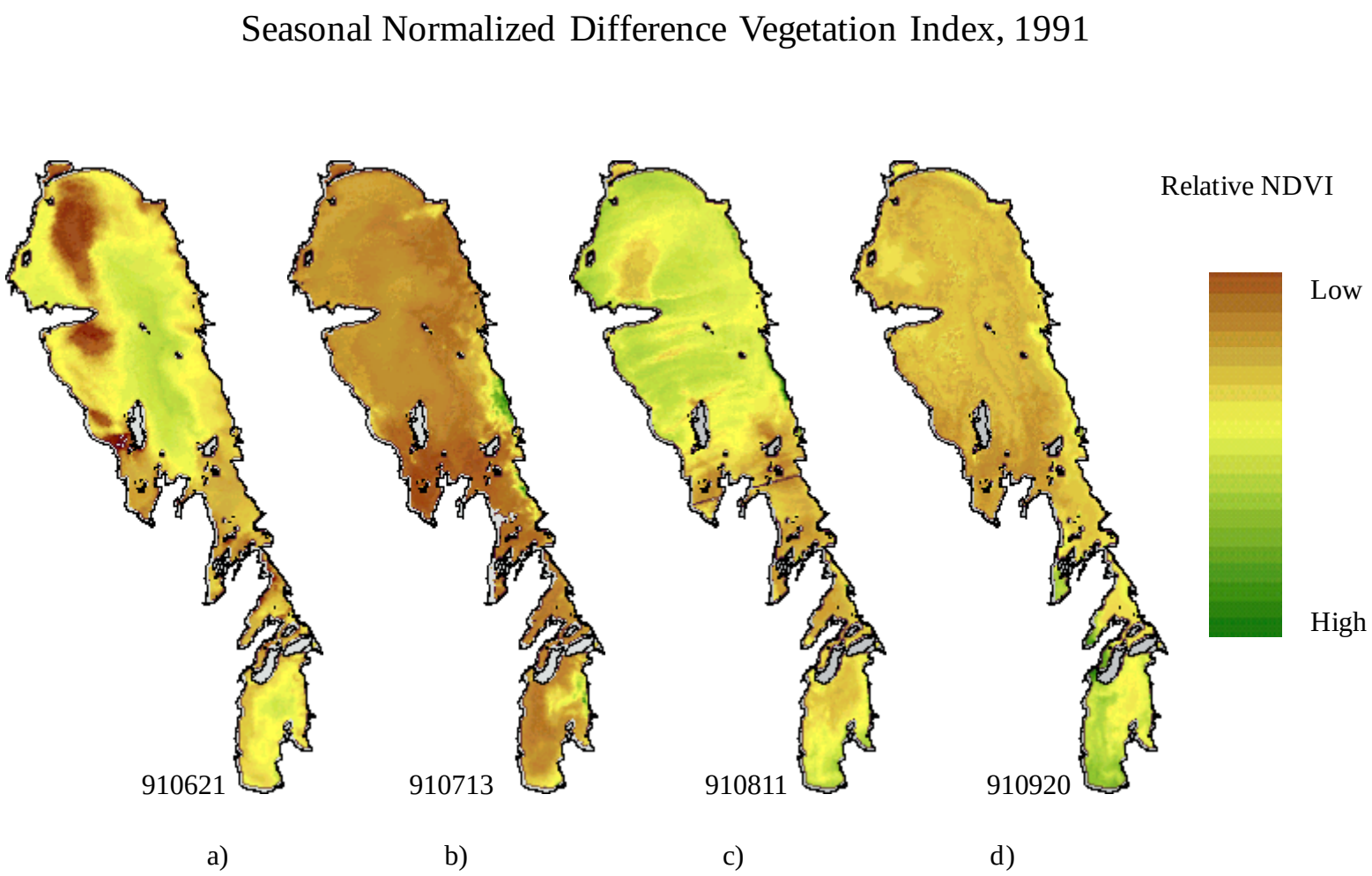

Figure 3.3. NDVI calculated from NOAA AVHRR data. Dates are in YYMMDD format.

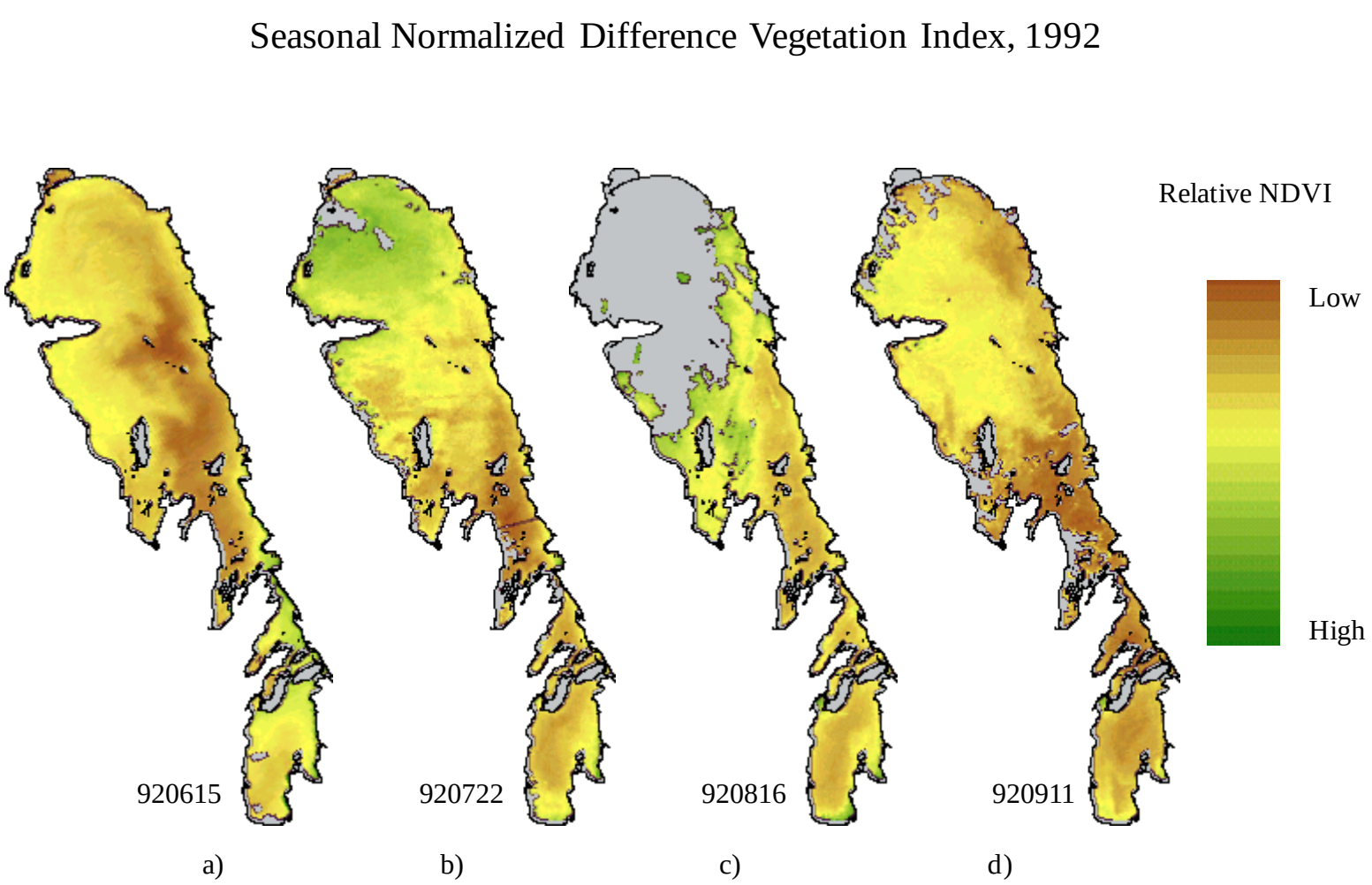

Figure 3.4. NDVI calculated from NOAA AVHRR data. Dates are in YYMMDD format.

Normalized Difference Vegetation Index, August 1993-96.

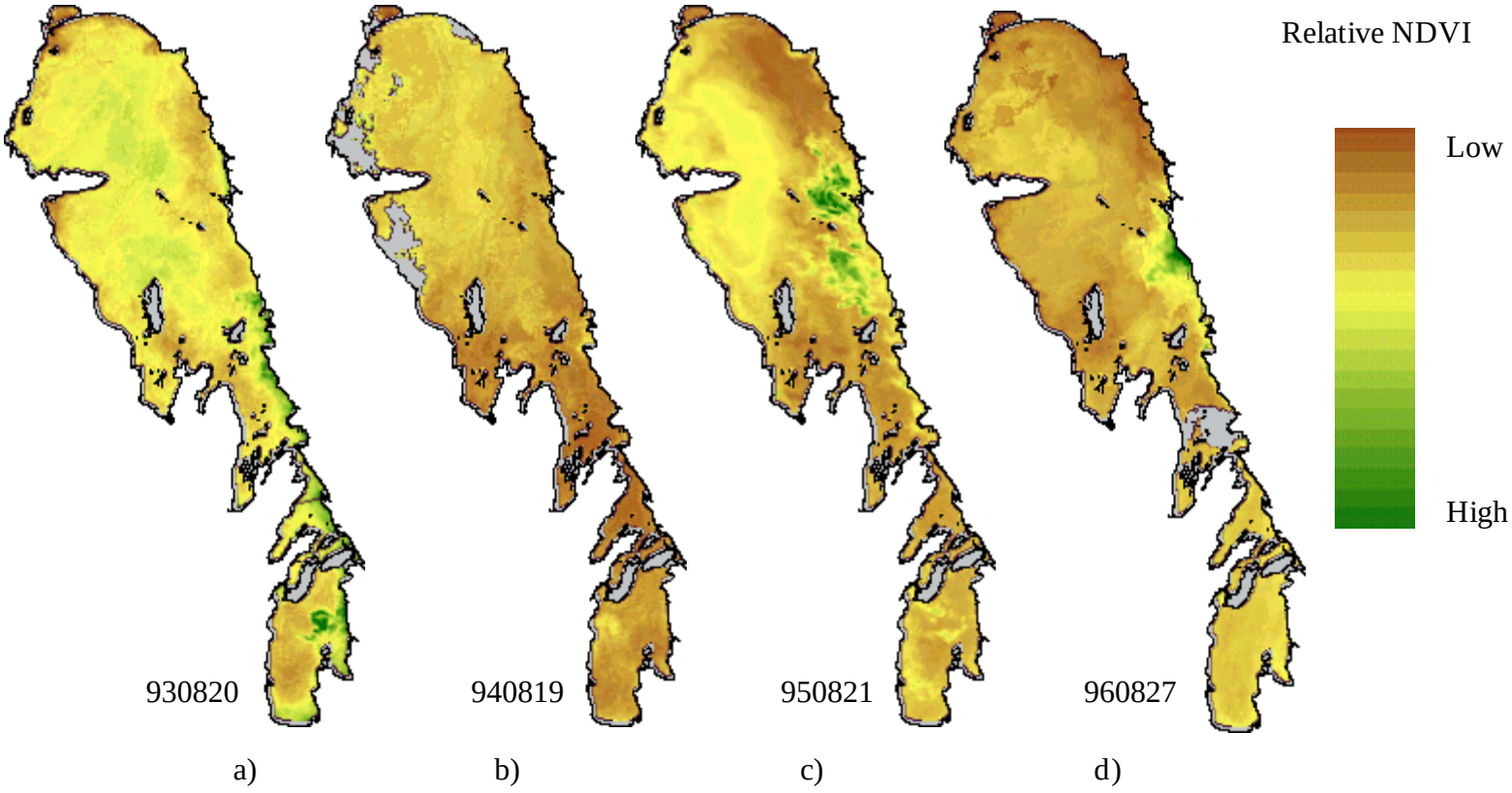

Figure 3.5. NDVI calculated from NOAA AVHRR data. Dates are in YYMMDD format.

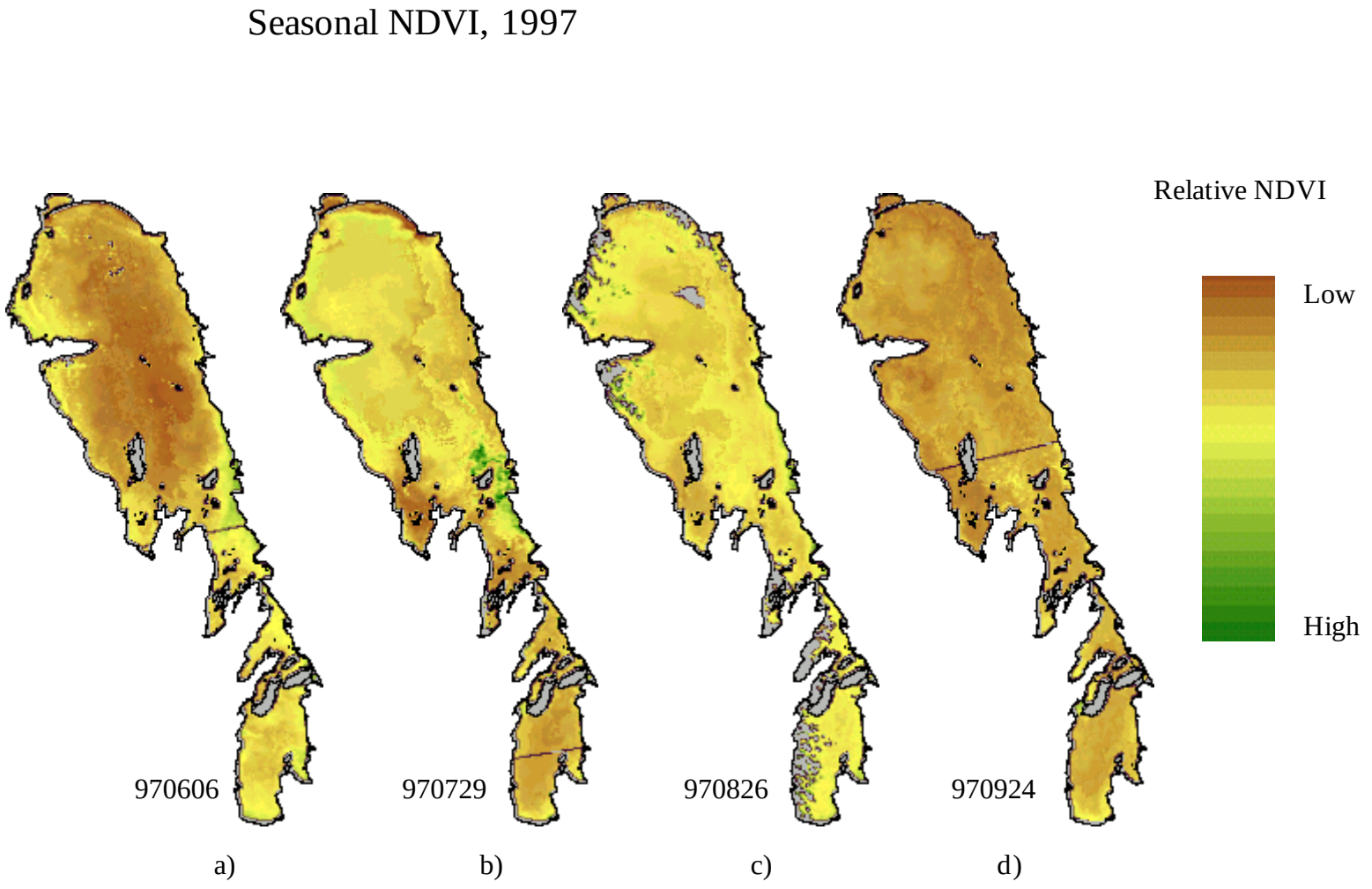

Figure 3.6. NDVI calculated from NOAA AVHRR data. Dates are in YYMMDD format.

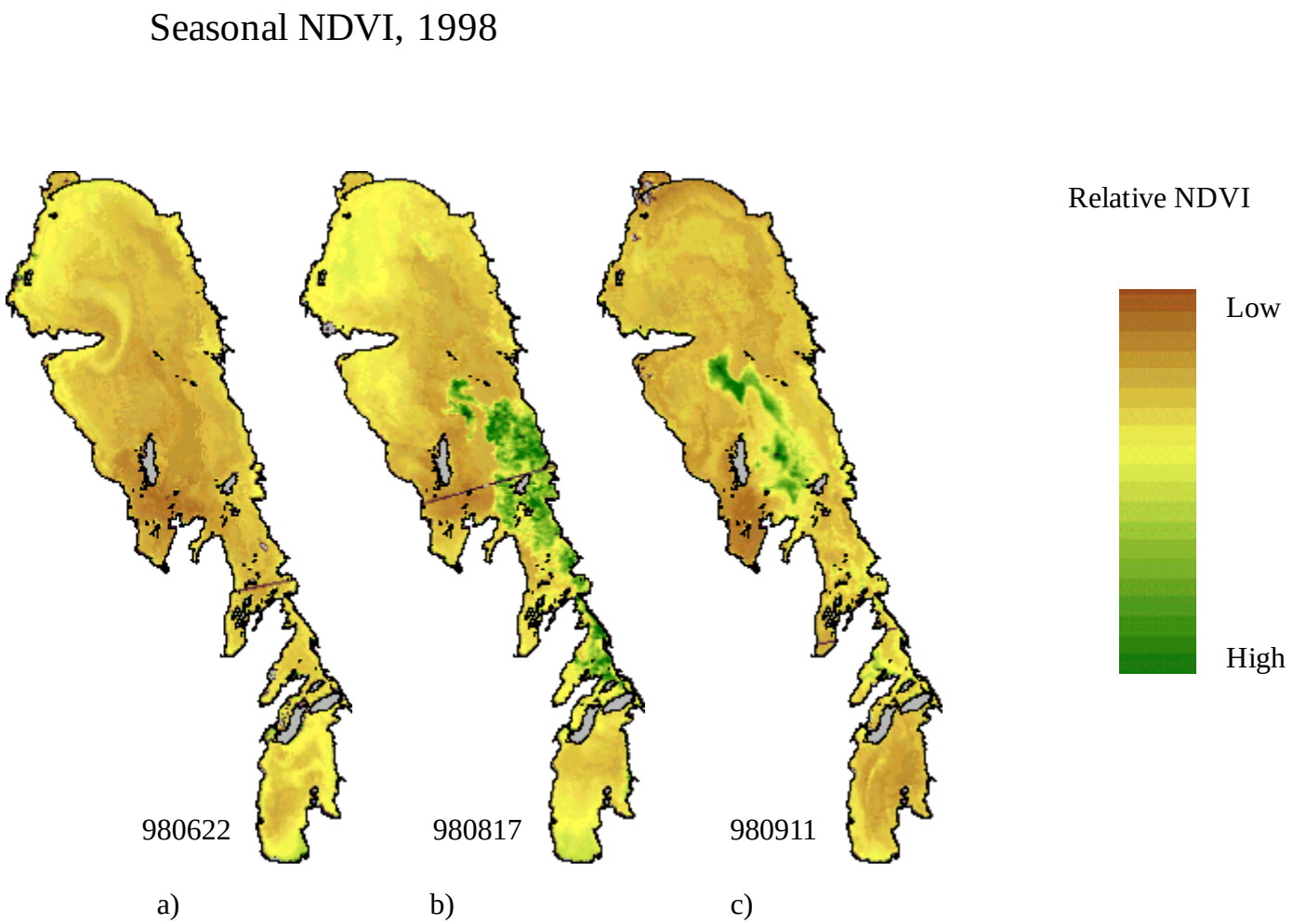

Figure 3.7. NDVI calculated from NOAA AVHRR data. Dates are in YYMMDD format.

Normalized Difference Vegetation Index, August 1999

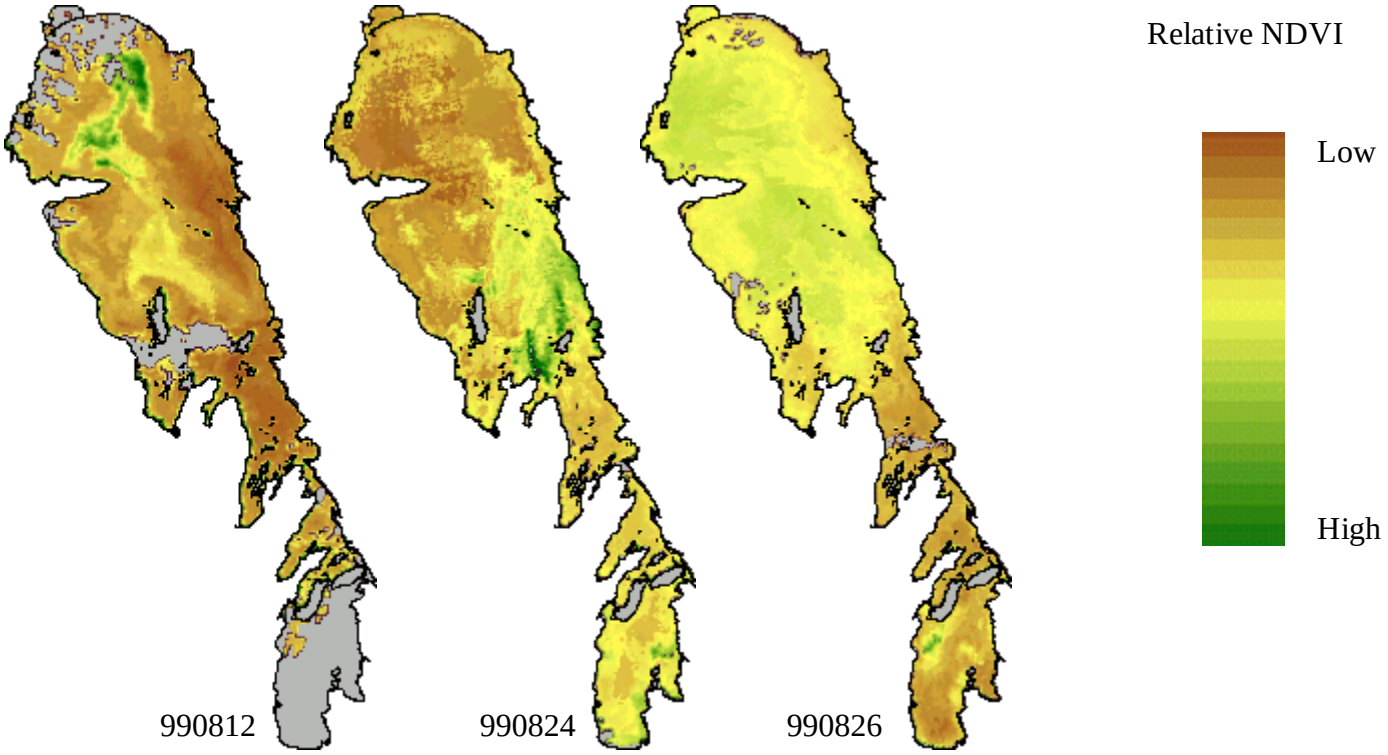

Figure 3.8. NDVI calculated from NOAA AVHRR data. Dates are in YYMMDD format.

Normalized Difference Vegetation Index, August and September 2000

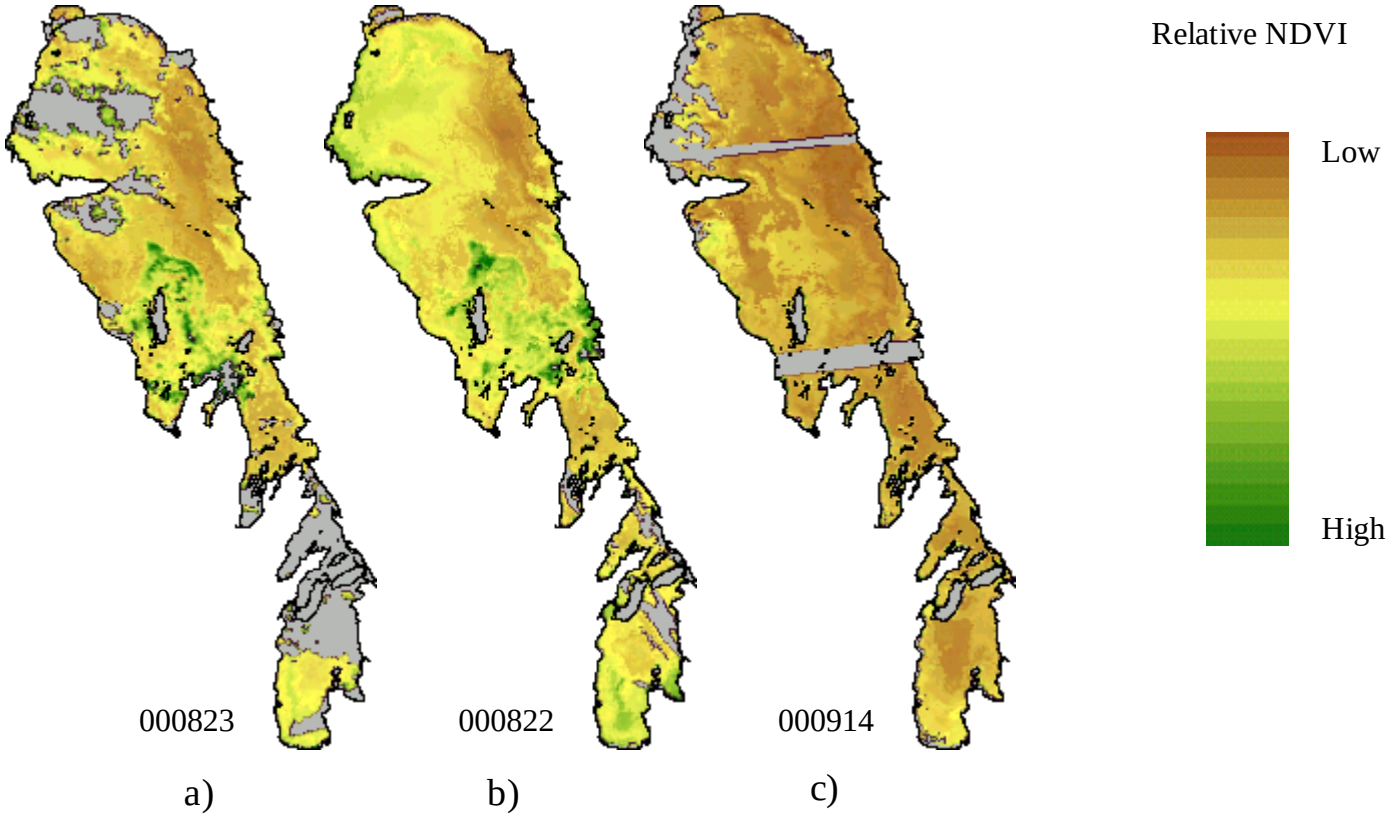

Figure 3.9. NDVI calculated from NOAA AVHRR data. Dates are in YYMMDD format.

11 APPENDIX 4. SPECTRAL ALBEDO SAMPLES FROM THE 23-25 AUGUST CRUISE

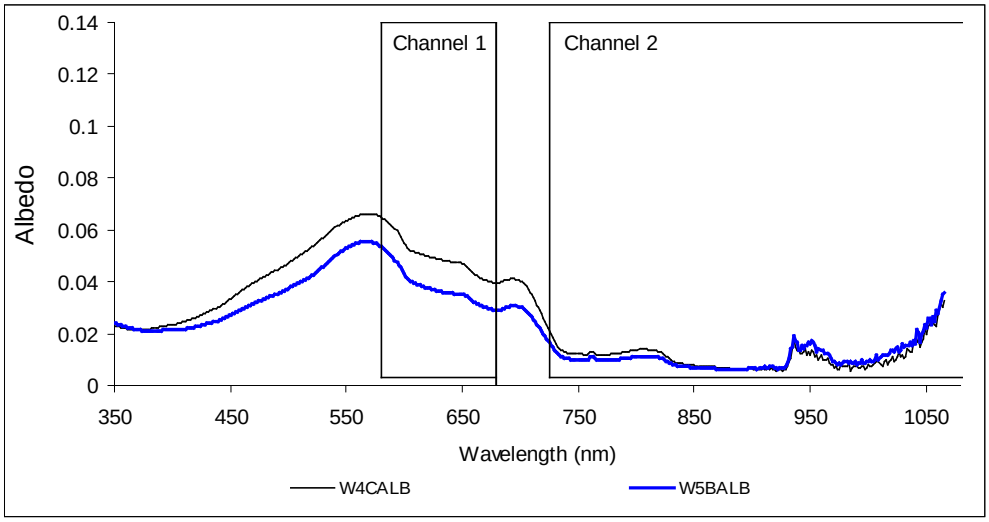

Figure 4.1. Spectral distribution of albedo for ASD samples 4 and 5 (corresponding to DFO stations 3 and 4). For ASD4, chl=26 ug·L^{-1}, TSS=15 mg·L^{-1}; for ASD5, chl=9.9 ug·L^{-1}, TSS=7 mg·L^{-1}. Albedo expressed as a decimal fraction. Boxes indicate spectral range of AVHRR Channel 1 (580-680 nm) and part of Channel 2 (725-1100 nm).

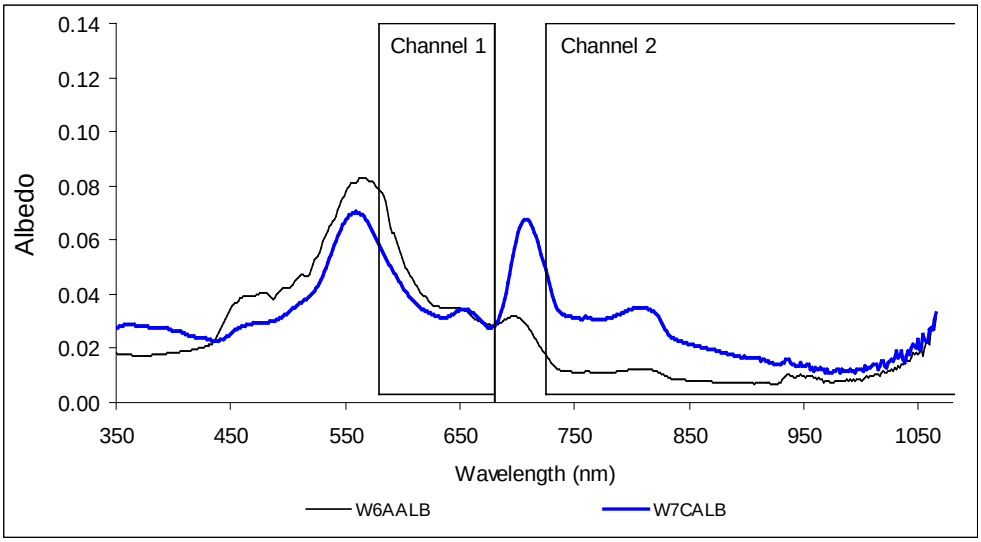

Figure 4.2. Spectral distribution of albedo for ASD samples 6 and 7 (corresponding to DFO stations 5 and 6). For ASD6, chl=12 ug·L^{-1}, TSS=6 mg·L^{-1}; for ASD7, chl=68 ug·L^{-1}, TSS=12 mg·L^{-1}. Albedo expressed as a decimal fraction. Boxes indicate spectral range of AVHRR Channel 1 (580-680 nm) and part of Channel 2 (725-1100 nm).

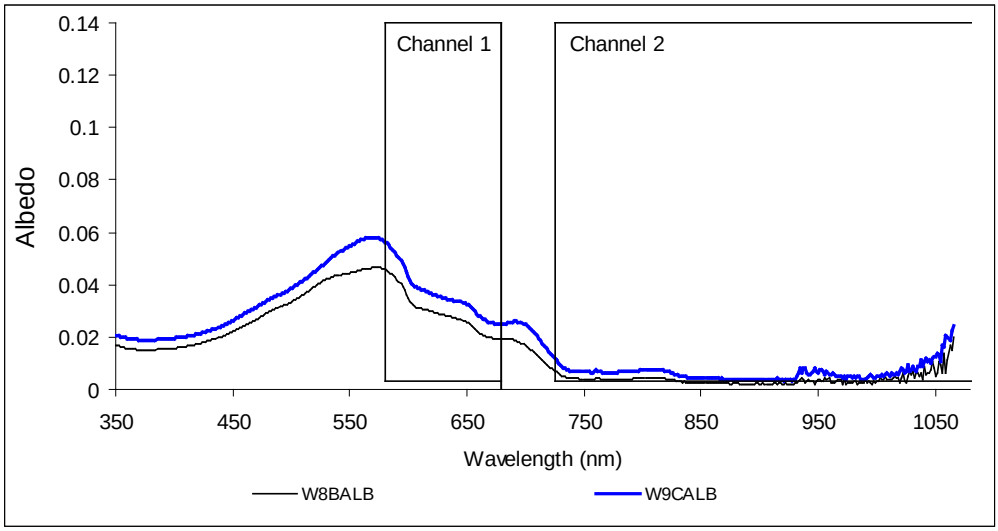

Figure 4.3. Spectral distribution of albedo for ASD samples 8 and 9 (corresponding to DFO stations 7 and 8). For ASD8, chl=6.6 ug·L^{-1}, TSS=5 mg·L^{-1}; for ASD9, chl=10 ug·L^{-1}, TSS=6 mg·L^{-1}. Albedo expressed as a decimal fraction. Boxes indicate spectral range of AVHRR Channel 1 (580-680 nm) and part of Channel 2 (725-1100 nm).

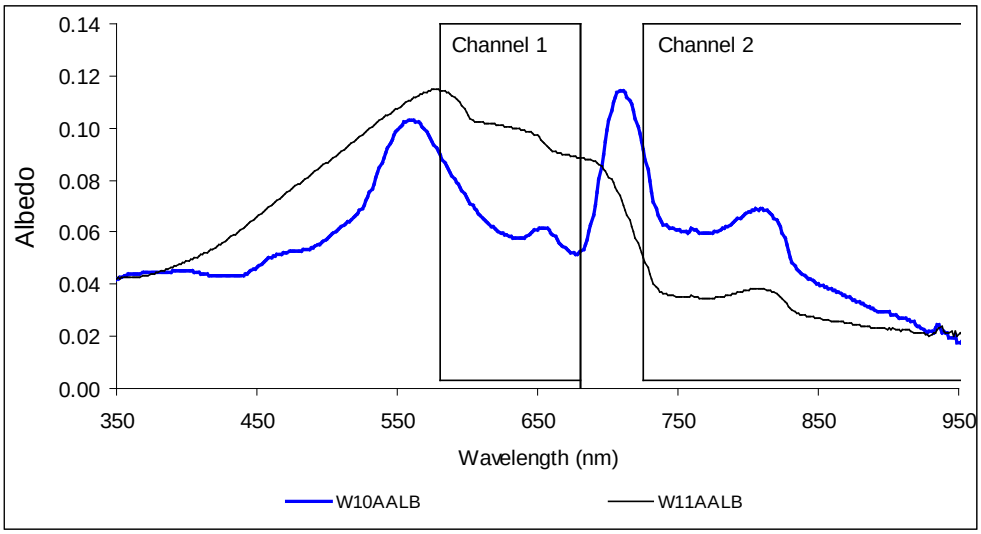

Figure 4.4. Spectral distribution of albedo for ASD samples 10 and 11 (corresponding to DFO stations 9 and "CLEAR"). For ASD10, chl=94 ug·L^{-1}, TSS=34 mg·L^{-1}; for ASD11, chl=4.1 ug·L^{-1}, TSS=18 mg·L^{-1}. Albedo expressed as a decimal fraction. Boxes indicate spectral range of AVHRR Channel 1 (580-680 nm) and part of Channel 2 (725-1100 nm).

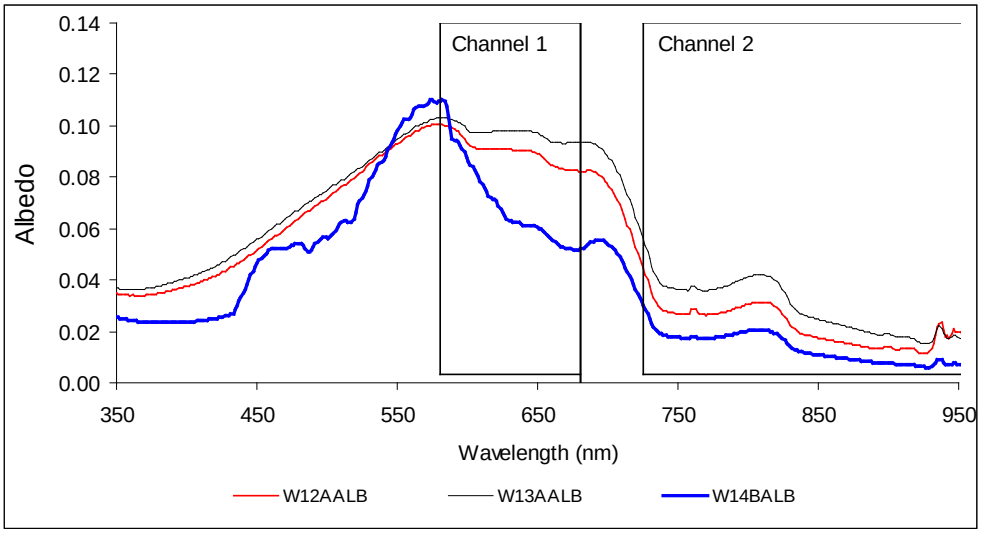

Figure 4.5. Spectral distribution of albedo for ASD samples 12, 13, and 14 (corresponding to DFO stations 10, 11 and Gimli). For ASD12, chl=5.2 ug·L^{-1}, TSS=24 mg·L^{-1}; for ASD13, chl=2.8 ug·L^{-1}, TSS=34 mg·L^{-1}; for ASD14, chl=17 ug·L^{-1}, TSS=21 mg·L^{-1}. Albedo expressed as a decimal fraction. Boxes indicate spectral range of AVHRR Channel 1 (580-680 nm) and part of Channel 2 (725-1100 nm).